In collaboration with:

Supported by:

15th PORSEC

PAN OCEAN REMOTE SENSING CONFERENCE

PRE-CONFERENCE PROCEEDINGS

(VOLUME I)

UNIVERSITI TEKNOLOGI MALAYSIA AND PORSEC ASSOCIATION

Organisers:

PRE-CONFERENCE PROCEEDINGS

VOLUME I

Universiti Teknologi Malaysia

15TH Pan Ocean Remote Sensing Conference (PORSEC)

Johor Bahru, Malaysia

e ISBN 978-967-19916-0-2

9 7 8 9 6 7 1 9 9 1 6 0 2

15th Pan Ocean Remote Sensing Conference (PORSEC)

Universiti Teknologi Malaysia, Johor Bahru, Malaysia

Editorial Team (UTM):

Assoc Prof. Sr Dr. Nurul Hazrina Idris
Dr. Wan Anom Wan Aris
Prof. Dr. Kasturi Devi Kanniah
Dr. Norhakim Yusof
Dr. Ami Hassan Md Din
Dr. Norhadija Darwin

Technical Team (UTM):

Muhammad Haikal Fayyadh Munadi
Nurul Liyana Ibrahim

Local Organising Committee:

Assoc Prof. Sr Dr. Nurul Hazrina Idris (Chairman 15th PORSEC LOC, Head of Tropical Mapping Resource Research Group, UTM)
Dr. Mohd Nadzri Md Reba (Co-Chairman 15th PORSEC LOC, Director INSTEG UTM)
Sr Dr. Nurul Hawani Idris (Secretary 15th PORSEC LOC, UTM)
Dr. Norhadija Darwin (UTM) (Co-Secretary 15th PORSEC LOC, UTM)
Dr. Noordyana Hassan (Treasury 15th PORSEC LOC, UTM)
Mr. Muhammad Hafizuddin Ripin (Co-Treasury 15th PORSEC LOC, UTM)
Prof. Dr. Kasturi Devi Kanniah (Assistant Dean – Quality and Strategy)
Assoc. Prof. Dr. Zulkepli Majid (Deputy Dean – Research and Innovation, FABU UTM)
Prof. Dr. Razali Mahmud (UTM)
Dr. Jaw Siow Wei (UTM)
Dr. Muhammad Rizal Mahmud (UTM)
Dr. Norhakim Yusof (UTM)
Dr. Abdul Wahid Rasib (UTM)
Dr. Muhammad Zulkarnain Abdul Rahman (UTM)
Dr. Muhammad Imzan Hasan (UTM)
Dr. Mohd Rozaimi Che Hasan (UTM)
Dr. Ivin Amri Musliman (UTM)
Dr. Alvin Lau Meng Shin (UTM)
Dr. Ami Hassan Md Din (UTM)
Dr. Wan Anom Wan Aris (UTM)
Dr. Othman Zainon (UTM)
Mdm. Yasni Nurul Huda Mohd Yassin (UTM)
Mr. Md Yani Kasiren (UTM)
Dr. Shaparas Daliman (UMK)
Assoc. Prof. Dr. Aidy@Mohamed Shawal bin M.Muslim (Director INOS, UMT)
Dr. Mohammad Shawkat Hossain (UMT)
Mr. Mohd Izuan Mohd Nadzri (UMT)
Dr. Norzailawati Hj Mohd Nor (IIUM)
Wan Shafrina Wan Mohd Jaafar (UKM)
Dr. Azzuliani Supangat (UM)
Assoc. Prof. Dr. Farrah Melissa Muharam (UPM)
Khairiyah Binti Ismail (Geospatial Executive, Spatial Synergy Consultant Sdn Bhd)

Scientific Organising Committee:

Dr. Gad Levy (PORSEC President; Senior Scientist at NorthWest Research Associates Seattle, Washington USA Division)
Dr. Abderrahim Bentamy (PORSEC Elected President; Senior Scientist at French Oceanographic Institute IFREMER)
Prof. Dr. Ming-An Lee (PORSEC Vice President)
Stefano Vignudelli (PORSEC Vice President; Senior Scientist at Consiglio Nazionale delle Ricerche at Pisa, Italy)
Nimit Kumar (PORSEC Executive Secretary, Outreach Chair)
Cara Wilson (Treasury; NOAA's Southwest Fisheries Science Center in Monterey CA, USA)

15th Pan Ocean Remote Sensing Conference (PORSEC)

Universiti Teknologi Malaysia, Johor Bahru, Malaysia

All papers in this book have been selected by the scientific committee.

The publisher makes no representation, express or implied, with regard to the accuracy of the information contained in this book and cannot any legal responsibility for any errors that may be made.

e ISBN 978-967-19916-0-2

9 7 8 9 6 7 1 9 9 1 6 0 2

MALAYSIA, 5 July 2021

Preface

Kumar Nimit[a], Gad Levy[b], Nurul Hazrina Idris[c]

[a]Indian National Centre for Ocean Information Services (INCOIS), Ministry of Earth Sciences (MOES), Hyderabad, India; [b]NorthWest Research Associates, Seattle, WA, USA; [b]Associate Faculty, University of Phoenix USA; [c]Geoscience and Digital Earth Centre, Research Institute of Sustainable Environment, Universiti Teknologi Malaysia, Johor Darul Takzim, Malaysia

This conference proceedings feature a selection of research papers (extended abstracts) and a full paper submitted for the 15th Biennial Pan Ocean Remote Sensing Conference (PORSEC). This is the first time we are publishing pre-conference proceedings due to restrictions in organizing conferences since the global pandemic of COVID-19 outbreak. It continues the legacy of seven previous special IJRS issues of PORSEC conferences, held in Busan, Korea; Guangzhou, China; Keelung, Taiwan; Kochi, India; Bali, Indonesia; Fortaleza, Brazil and Jeju Island, the Republic of Korea, respectively (Levy and Gower 2008, 2010, 2012; Gower and Levy 2014; Levy, Vigundelli, Gower 2016, 2018; and Levy, Nimit, Vigundelli, Gower, 2020). Established in 1990 (the International Space Year), with the name of "Pacific Ocean Remote Sensing Conference", PORSEC has gained equal popularity among leading and aspirant countries in this field as a platform for sharing ocean remote sensing research and applications. The now common component of capacity building in the form of a pre-conference tutorial is one of the most acclaimed aspects of PORSEC and has cultivated young brains to pursue works for the benefit of mankind.

A total of 14 full papers planned to be presented at PORSEC2020 (now postponed till further update) have been accepted for publication by the scientific committee after reviewing and necessary revisions. Ten of the papers address regional science problems, while two others address tropical seas (Arabian Sea, Persian Gulf), one addresses the science of sub-tropical sea (Sea of Azov), and one addresses polar (Arctic) regions. Half of these papers make use of altimeter data, underlining the importance of the sensor and making a strong case for a constellation with altimeter sensors to be maintained. Among the other papers, two each make use of wind or ocean colour data. Most of the papers from the Indo-Pacific region address topics of coastal zone management and spatial planning in one way or the other. Further, a significant number of papers make use of the Artificial Intelligence (AI) to process the datasets or derive conclusions, which is a welcome approach considering 'massive data' necessities being applied to the satellite remote sensing in terms of day-by-day and ever growing (spatial, temporal, spectral) resolutions and longer time-series. This highlights the need for robust mapping with the help of geospatial and machine learning tools, for achieving the goals of the UN Decade of Ocean Science for Sustainable Development (2021-2030).

Herewith, we would like to express gratitude to the Asia Pacific Network (APN) for Global Change Research, Committee on Space Research (COSPAR), Scientific Committee on Oceanic Research (SCOR), Institution of Geospatial and Remote Sensing Malaysia (IGRSM), and Malaysia Convention & Exhibition Bureau (MyCEB) for the financial supports. A sincere "thank you" to our collaborators from the Malaysia Space Agency and local universities including the Universiti of Kebangsaan Malaysia (UKM), Universiti Putra Malaysia (UPM), Universiti Malaysia Kelantan (UKM), International

Islamic University Malaysia (IIUM), Universiti Sains Malaysia (USM) and University of Malaya (UM).

References

Gower, J., and G. Levy. 2014. “Ocean Remote Sensing for Well-being of All.” International Journal of Remote Sensing 35 (14): 5311–5314. doi:10.1080/01431161.2014.941242.

Levy, G., and J. Gower. 2008. “Preface Satellite Observations of the Atmosphere, the Ocean and Their Interface: Climate, Natural Hazards and Management of the Coastal Zone.” International Journal of Remote Sensing 29 (21): 6085–6090. ISSN 0143-1161. doi:10.1080/01431160802302116.

Levy, G., and J. Gower. 2010. “Preface - Oceanic Manifestation of Global Changes: Satellite Observations of the Atmosphere, Ocean and Their Interface.” International Journal of Remote Sensing 31 (17–18): 4509–4514. doi:10.1080/01431161.2010.485225.

Levy, G., and J. Gower. 2012. “Connecting Regional Impacts to Global Environmental Change.” International Journal of Remote Sensing 33 (23): 7305–7309. doi:10.1080/01431161.2012.685990.

Levy, G., Nimit K., Vignudelli, and J. Gower. 2020. Preface: Interdisciplinary multi-sensor studies of the Pacific and Indian Oceans, International Journal of Remote Sensing, 41:15, 5645-5652, DOI: 10.1080/01431161.2020.1766293.

Levy, G., S. Vignudelli, and J. Gower. 2016. “Ocean Remote Sensing for Sustainable Resources.” International Journal of Remote Sensing 37 (9): 1977–1980. doi:10.1080/01431161.2016.1175804.

Levy, G., S. Vignudelli, and J. Gower. 2018. “Editors - Enabling Earth Observations in Support of Global, Coastal, Ocean, and Climate Change Research and Monitoring.” International Journal of Remote Sensing 39 (13): 4287–4292. doi:10.1080/01431161.2018.1464101.

TABLE OF CONTENTS

MULTI-MISSION SATELLITE ALTIMETER FOR PROJECTING RISING SEA LEVEL ACROSS MALAYSIAN SEAS

Amalina Izzati binti Abdul Hamid[1*], Ami Hassan Md Din[1,2*], Norhakim Yusof[3], Nazirah Mohamad Abdullah[4]

[1] Geomatics Innovation Research Group (GnG), [2] Geoscience and Digital Earth Centre (INSTEG), Faculty of Built Environment and Surveying, Universiti Teknologi Malasia, 81310 Johor Bahru, Johor, Malaysia
*amalinaabdhamid55@gmail.com; *amihassan@utm.my
[3] Department of Geoinformation, Faculty of Built Environment and Surveying, Universiti Teknologi Malaysia, 81310 Johor Bahru, Johor, Malaysia
[4] Faculty of Civil and Environmental Engineering, Universiti Tun Hussein Onn Malaysia, 86400 Parit Raja, Johor, Malaysia

KEYWORDS: Malaysian Seas; Multi-Mission Satellite Altimeters; Rising Sea Level; Sea Level Projection

ABSTRACT:

Across Malaysian seas, the sea level is undeniably rising, and it can be justified from an accelerating value from satellite altimeter measurement. Grounded by the accessible in-situ and space-based data sets, quantifying contemporary sea-level change and understanding its causes have improved remarkably in recent years. By presenting a robust f itting linear trend to express rising Malaysian sea-level projections, this paper highlights the analysis and interpretation of predicated 21st-century rising sea levels over Malaysian seas from a multi-mission satellite altimeter. Sea level anomalies (SLAs) are determined using data from the Radar Altimeter Database System (RADS), covering eight altimeter missions from enhanced processing strategy to optimize sea surface heights (SSHs). Projections then are calculated every 20 years, over Malaysian seas grid lin es retrieved from robust fit regression simulations. Our result demonstrates that during the 21st century, Malaysian seas will encounter a rise of 13.15 cm by 2040, 20.23 cm by 2060, 27.31 cm by 2080, and 34.39 cm by 2100. Information on projected sea leve l in this region is valuable for a wide variety of climate applications and for studying environmental issues while also important for its relevance to predict future regional climates for disaster adaptation measures.

I. INTRODUCTION

Our major preoccupation, all over the globe, has always been trying to predict, or rather speculate, what the weather has in store for us. The most widespread indication that the Earth is steadily changing has been perpetual warming from greenhouse gases due to anthropogenic effects (NASA, 2020). From this effect, oceans have warming, which accounts for 90% of the increase in energy stored within the climate system between the years 1971 and 2010 (IPCC, 2014). As a result, the oceans are rising attributable to the thermal expansion of global warming. Figure 1 displays the estimated attributes responsible for 21st-century rising sea levels (Church et al., 2001). The estimated sea level rate from thermal expansion ranges from 0.3 mm/yr to 0.7 mm/yr, higher than any other contribution.

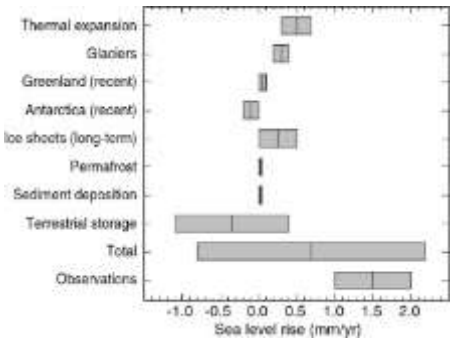

Figure 1. Mean acceleration of sea level its estimated contributions (Church et al., 2001)

As modern technology advances, the acquisition of sea level data has been enhanced. According to Hamid et al. (2018), Malaysian seas have been rising at a rate of 4.22 ±0.12 mm/yr, with a magnitude of around 5 cm from a series of satellite altimeters. Thereby, This paper is emphasized on projecting the Malaysian sea level from multi-mission of satellite altimeters. Implications of such sea level trends will be presented as well.

II. DATA AND METHODS

A. RADS for Multi-mission Satellite Altimeter Processing

Sea level anomalies (SLAs) are extracted from the Radar Altimeter Database System or RADS over Malaysian Seas; more than ten satellite altimeters have been employed which spanning from January 1993 to December 2015. Details regarding the altimetry used are described in Table 1:

Table 1. Selected altimetry mission for this study

Satellite	Phase	Sponsor	Period	Cycle
TOPEX	A, B, N	NASA/Cnes	Jan 93 - Jul02	11 - 363
Jason-1	A, B, C	NASA/Cnes	Jan 02 - Jun 13	1 - 425
Jason-2	A	NASA/Cnes	Jul 08 - Mac 16	0 - 282
ERS-1	C, D, E, F, G	ESA	Jan 93 - Jun 96	91 - 156
ERS-2	A	ESA	Apr 95 - Jul 11	0 - 169
Envisat	B, C	ESA	May 02 -Apr12	6 - 113
Cryosat	A	ESA	Jul 10 - Dec 15	4 - 77
Saral	A	ESA	Mac 13 - Dec15	1 - 31

RADS offers an altimetry data processing that executes a standard coordinated analysis, data collection, software distribution, and recommendations. (Hamid et al., 2018). The sea level data are adjusted for orbital altitude and altimeter range to which the specific bias is reduced in RADS; hence, the sampling characteristics of the altimetry data are improved. The altimeter corrections and bias removal are then performed by applying specific models on each satellite altimeter mission in RADS. Distance-weighted gridding and filtering are implemented in order to lose as little information as possible while still obtaining meaningful grid values. The daily solutions of SLAs are then combined into monthly average solutions, which are carried out to standardize the final monthly altimeter solution with the monthly tide gauge solution. Figure 2 outlines the RADS altimetry data processing employed in this study.

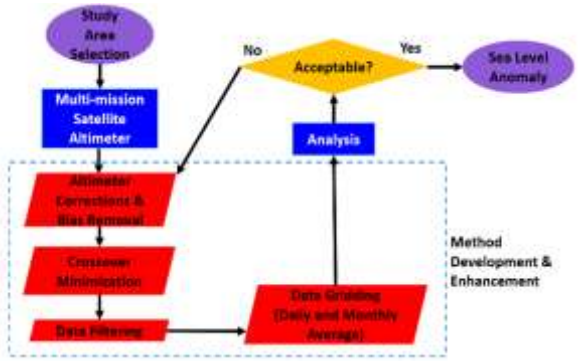

Figure 2. Altimetry data processing overview in RADS (Din et al., 2015; Hamid et al., 2018)

B. Tidal Data for Altimetry Data Validation

The monthly tidal data is the domain of interest of this study for the verification of RADS altimetry data. The verification is carried out by extracting the monthly SLA average at tide gauge locations and the altimeter track that are nearby the tide gauge stations. The pattern and correlation of SLAs from both measurements are then evaluated over the same period in each area. Figure 3 illustrates the allocation of the tide gauge stations used in the validation between altimetry and tidal data. The chosen tide gauges are stationed in the front of the South China Seas as more satellite tracks can be accessed, which encompass Geting, Cendering, T g. Gelang, P. Tioman and Tg. Sedili, Bintulu, Labuan and K. Kinabalu.

Figure 3. Tide gauge stations allocation that has been used in data verification.

C. Robust Fitting for Projecting Rising Sea Level

Trends are calculated by a robust fitting method. The approach, which is called Iteratively Re-weighted Least Squares (IRLS) (Holland and Welsch, 1977), fits the SLA time series by a linear function and then solves for the trend in the function while removing SLA outliers by iterations. The weight of measurements is adjusted according to the deviation from the trend line, which is re-fitted, and repeated until the solution converges. The relationship of robust fitting can be expressed as (Holland and Welsch, 1977; Hamid et al., 2018; Din et al., 2019):

$$wi = \begin{cases} (1-(u_i)^2)^2 & |u_i| < 1 \\ 0 & |u_i| \geq 1 \end{cases} \quad (1)$$

Where,

$$ui = \frac{r_i}{K.S.\sqrt{1-h_i}}$$

r_i : Residuals,

h_i : Leverage,

S : Mean absolute deviation divided by a factor 0.6745 to make it an unbiased estimator of standard deviation

K : A tuning constant whose default value of 4.685 provides for 95% asymptotic efficiency as the ordinary least squares assuming a Gaussian distribution

Observations attributed to zero weight in any iteration are declared outliers and have been eliminated from the further computation.

III. RESULTS AND ANALYSIS

A. Validating Altimetry Data with Tidal Data

As mentioned in Section II (A), daily altimetry solutions are averaged into monthly solutions. This manifests to the monthly tidal solutions for the validation. Tide gauge solutions are grounded on continuous measurements at one location, whereas the altimeter, in the best scenario, only revisits a similar site three times in a month, and in the worse-case, only once ((Trisirisatayawong et al., 2011). The validation analysis is focused on the pattern and correlation aspects of SLA, and the Root Mean Square Error (RMSE) is subsequently computed. Both measurements are evaluated over the same period for the purpose of producing comparable results. The SLA time series from altimetry data and tidal records at selected tide gauge stations show similar patterns, indicating good agreement for all stations. Meanwhile, correlation analysis for all locations exhibits a confidence result with a correlation (R^2) value that ranges from 0.8215 to 0.9413, and is statistically significant. All altimetry data achieved RMS differences between 2.60 cm to 4.75 cm when compared to tidal data. Table 2 summarise the R^2 and RMSE values for the validation, while Figure 4 shows the evaluation plots of the outcome from both measurements.

Table 2. Validation values between altimetry and tidal SLA

Stations	R^2	RMS difference (cm)
Geting	0.9413	4.75
Cendering	0.9243	4.59
Tg. Gelang	0.9380	3.79
P. Tioman	0.9404	3.21
Tg. Sedili	0.9270	3.79
Bintulu	0.8215	3.36
Labuan	0.9071	2.60
K. Kinabalu	0.9069	2.99

a)

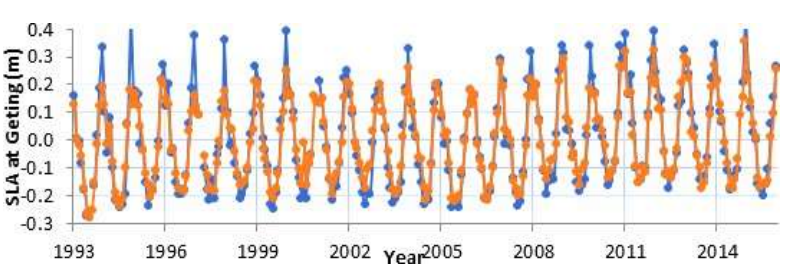
SLA at Geting (m)
Year

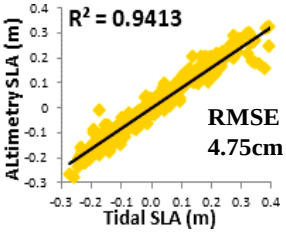
R² = 0.9413
RMSE
4.75cm
Altimetry SLA (m)
Tidal SLA (m)

b)

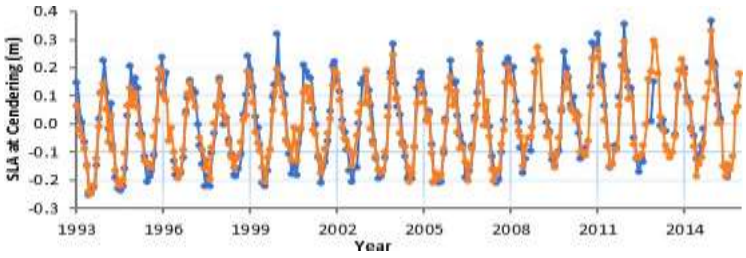
SLA at Cendering (m)
Year

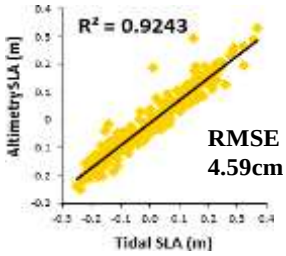
R² = 0.9243
RMSE
4.59cm
Altimetry SLA (m)
Tidal SLA (m)

c)

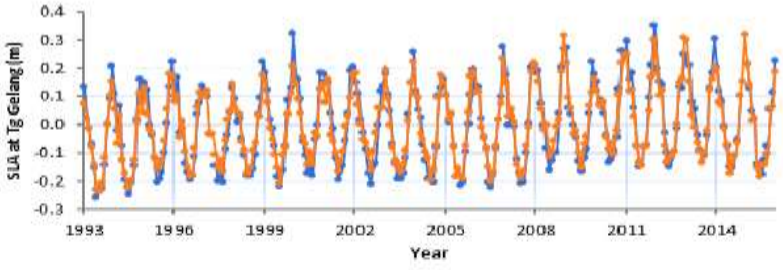
SLA at Tg Gelang (m)
Year

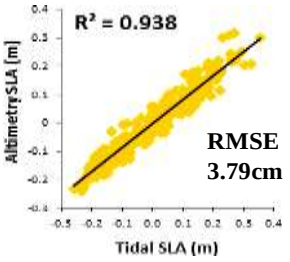
R² = 0.938
RMSE
3.79cm
Altimetry SLA (m)
Tidal SLA (m)

d)

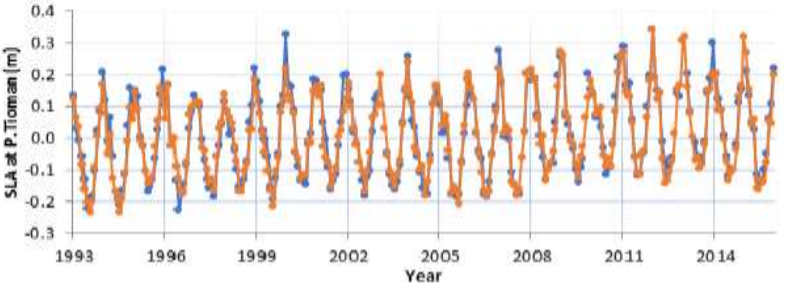
SLA at P. Tioman (m)
Year

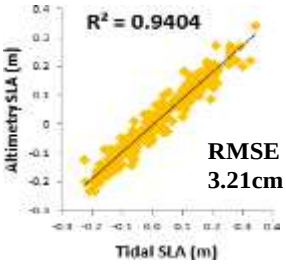
R² = 0.9404
RMSE
3.21cm
Altimetry SLA (m)
Tidal SLA (m)

e)

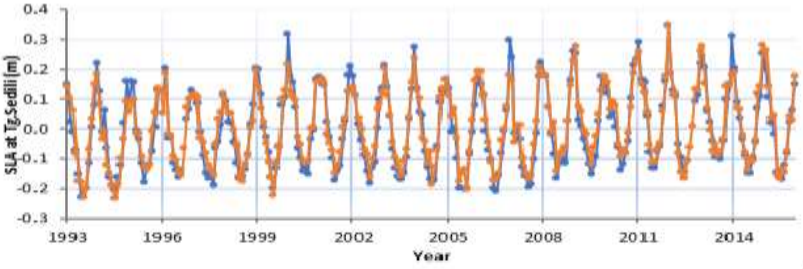
SLA at Tg Sedili (m)
Year

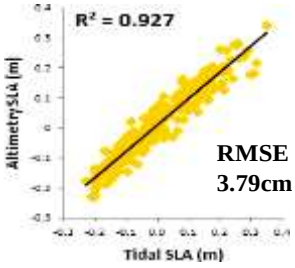
R² = 0.927
RMSE
3.79cm
Altimetry SLA (m)
Tidal SLA (m)

f)

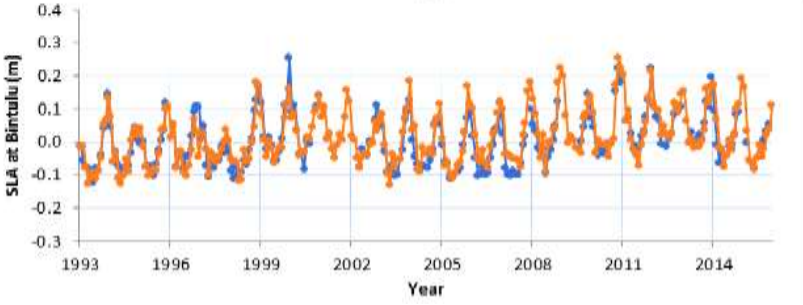
SLA at Bintulu (m)
Year

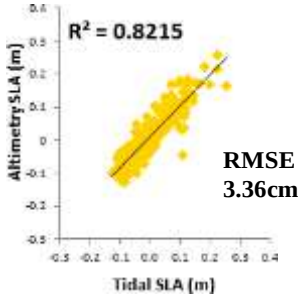
R² = 0.8215
RMSE
3.36cm
Altimetry SLA (m)
Tidal SLA (m)

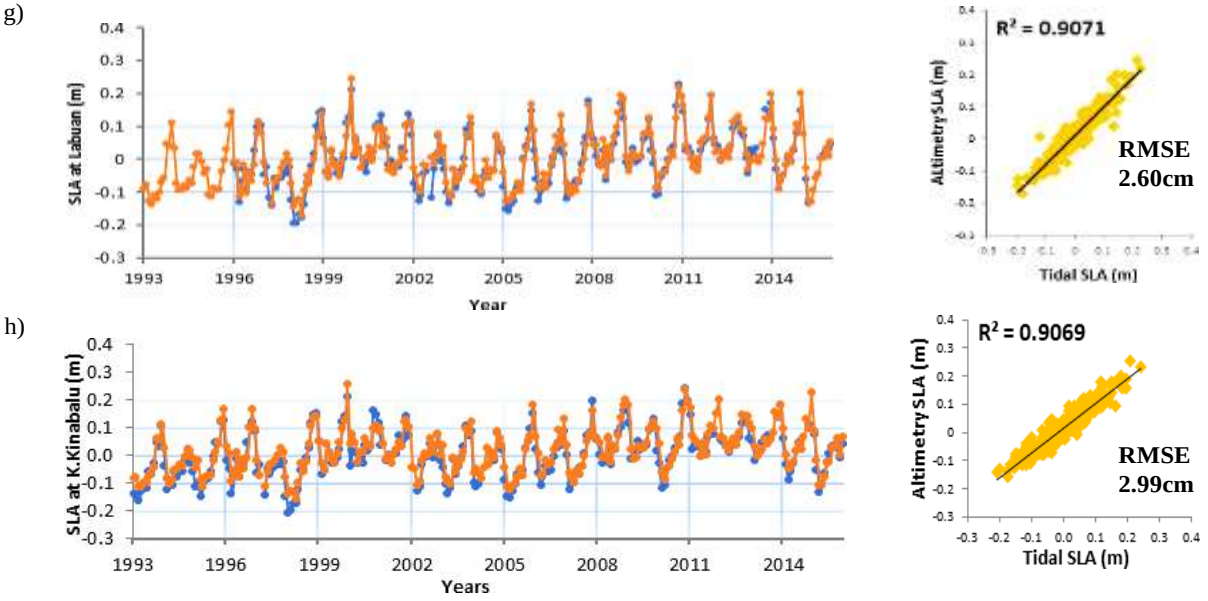

Figure 4. Evaluation plots between SLA time series from tide records (blue) and altimetry (orange) with their correlation

These results prove that the altimeter processing in RADS is well executed for this study; therefore, the altimetry data has shown a good probability in determining the sea level of this region.

B. Projecting Rising Sea Level from Satellite Altimeter

By presenting a robust fitting linear trend to express rising Malaysian sea level projections, the analysis and interpretation of predicted 21st century rising sea levels over Malaysian seas from multi-mission satellite altimeter data are presented. Projections are calculated every 20 years from the year 2020 until 2100 over Malaysian seas grid lines retrieved from altimeter missions. From the computed rates of Malaysian sea levels, a linear projection from robust fit regression simulations is continuously carried on until the year 2100. Figure 5 demonstrates robust fitting linear trends until the year 2100 at Malacca Straits.

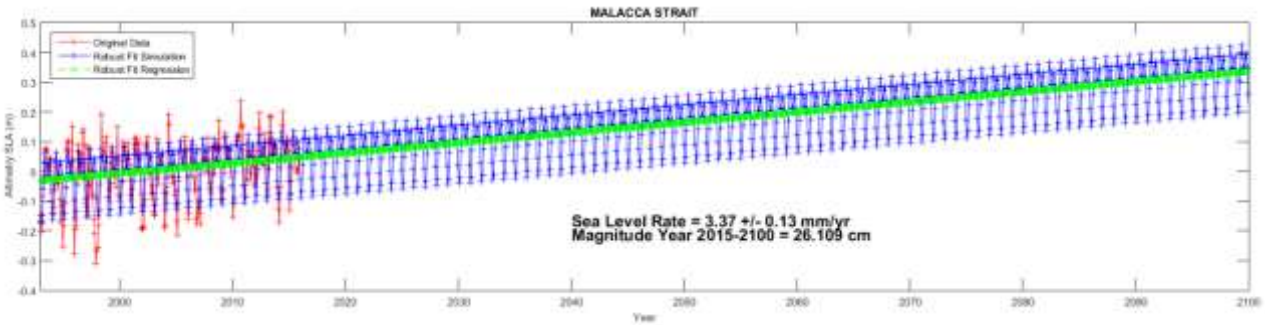

Figure 5. Time series of robust fitting linear trend projection of rising sea levels at Malacca Straits

The Malaysian coastal zone will experience coastal erosion by 2100. As reported by Leatherman et al. (2000), a sustained increase of 10 cm in sea level results in 15 m of coastal erosion. The average magnitude from 2015 to 2100 is 34 cm above the seas of Malaysia. Figure 7 illustrates the projection of rising sea levels over Malaysian seas every 20 years. The Malacca Strait will face a rise of 26 cm, and the South China Sea will face 39 cm. The Sulu Sea would experience a rising sea level of 45 cm, close to that of the Celebes Sea during this period. It should be remarked that the projection of rising sea levels from this study does not take into account external effects such as temperature, vertical land motion, and so on.

Table 3 summarises the median (minimum to maximum) of Malaysian rising sea level projections for every 20 years.

Table 3. Average magnitude of sea level projection over Malaysian seas

Year	Average rising sea levels projection from 2015 (cm)
2020	6.073 (0.014 to15.885)
2040	13.153 (2.413 to 28.160)
2060	20.232 (2.982 to 44.644)
2080	27.312 (3.551 to 61.127)
2100	34.392 (4.120 to 77.611)

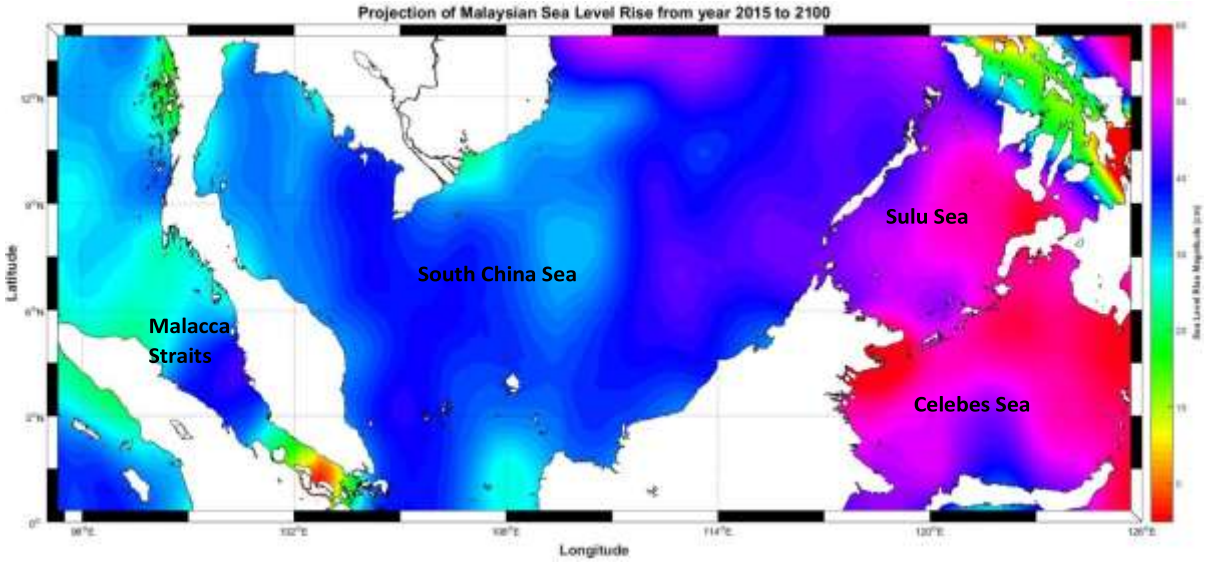

Figure 7. Map of the projection of rising sea levels over Malaysian seas from the year 2015 to 2100

IV. CONCLUSION

By having enough confidence in the data and selecting the best methods for processing all the data together from the year 1993 until 2015, projecting Malaysian rising sea level rise is carried out for every 20 years from 2020 to 2100. Malaysian sea levels are projected to rise by 34 cm by 2100, and the highest projected rise than previous years i.e. a rise of 6.07 cm by 2020, 13.15 cm by 2040, 20.23 cm by 2060 and 27.31 cm by 2080 with the Celebes Sea is the most effected with a projected rise of 45.1 cm, higher than other Malaysian seas.

Information on trends in the sea level in this region is valuable for coastal management, urban development and flood mitigation. It is also important to be used in projecting the rising sea levels for their relevance to future regional climates. Adaptation measures are needed to reduce the potential impact of rising sea levels, particularly in coastal areas. In order to reduce the negative impact of rising sea levels in Malaysia, adaptation measures such as coastal defenses, beach nourishment, offshore barriers, flood gates, mangroves, etc. should be implemented progressively.

ACKNOWLEDGEMENS

The authors would like to express gratitude towards TU Delft, Permanent Service for Mean Sea Level (PSMSL) and Department of Survey and Mapping Malaysia (DSMM) for providing altimetry and tidal data respectively. This research is funded by the Ministry of Higher Education (MOHE) under the Fundamental Research Grant Scheme (FRGS) Fund, Reference Code: FRGS/1/2020/WAB05/UTM/02/1 (UTM Vote Number: R.J130000.7852.5F374).

REFERENCES

Church, J. A., Gregory, J. M., Huybrechts, P.,Kuhn, M., Lambeck, K., Nhuan, M. T., Qin, D., Woodworth, P. L., 2001. Changes in Sea Level, in: J.T Hought on, Y. Ding, D.J. Griggs, M. Noguer, P.J. Van der Linden, X. Dai, K. Maskell, and C.A. Johnson (eds.): Climate Change 2001: The Scientific Basis: Contribution of Working Group I to the Third Assessment Report of the Intergovernmental Panel.

Din, A.H. M, Reba, M.N. M, Omar, K.M., Pa'suya, M.F., Ses, S., 2015. Sea Level Rise Quantification using Multi-mission Satellite Altimeter over Malaysian Seas. Proceedings - The 36th Asian Conference on Remote Sensing.

Din, A. H. M., Zulkifli, N. A., Hamden, M. H., & Aris, W. A. W., 2019. Sea level trend over Malaysian seas from multi-mission satellite altimetry and vertical land motion corrected tidal data. Advances in Space Research, 63(11), 3452 –3472.

Hamid, A. I. A., Din, A. H. M., Hwang, C., Khalid, N. F., Tugi, A., Mohd, K., 2018. Journal of Asian Earth Sciences Contemporary sea level rise rates around Malaysia: Altimeter data optimization for assessing coastal impact. Journal of Asian Earth Sciences, 166 (October 2017), 247–259. http://doi.org/10.1016/j.jseaes.2018.07.034

Holland, P. W. and Welsch, R. E., 1977. Robust Regression using Iteratively Reweighted Least-squares. Communications in Statistics—Theory and Methods 6 (9), 813–827.

IPCC, 2014. Synthesis Report. Contribution of Working Groups I, II and III to the Fifth Assessment Report of the Intergovernmental Panel on Climate Change. IPCC, Geneva, Switzerland.

Leatherman, S. P.; Zhang, K.; Douglas, B.C., 2000. Sea level rise shown to drive coastal erosion. Eos, Transactions American Geophysical Union, Volume 81, Issue 6, p. 55 -57.

NASA, 2020. National Aeronautics and Space Administration, https://sealevel.nasa.gov/understanding-sea-level/key-indicators/global-mean-sea-level.

Trisirisatayawong, I., Naeije, M., Simons, W. and Fenoglio-Marc, L., 2011. Sea Level Change in the Gulf of Thailand from GPS Corrected Tide Gauge Data and Multi-Satellite Altimetry. Global Planetary Change, 76: 137 -151.

MARINE GEOID MODELING FROM MULTI-MISSION SATELLITE ALTIMETRY DATA USING LEAST SQUARES MODIFICATION OF STOKES' WITH ADDITIVE CORRECTIONS APPROACH

Nornajihah Mohammad Yazid [1], Ami Hassan Md Din [1,2], Abdullah Hisam Omar[1], Cheinway Hwang[3], Muhammad Faiz Pa'suya[4], Nazirah Mohamad Abdullah[5], Zainal Abidin Md Som[1]

[1] Geomatic Innovation Research Group (GNG), [2]Geoscience and Digital Earth Centre (INSTEG), Faculty of Built Environment and Surveying, Universiti Teknologi Malaysia, 81310, Johor Bharu, Johor, Malaysia- nornajihah1510@gmail.com, amihassan@utm.my, abdullahhisham@utm.my, zams.geo@gmail.com

[3]Department of Civil Engineering, National Chiao Tung University, 1001 Ta Hsueh Road, Hsinchu 300, Taiwan - cheinway@nctu.edu.tw

[4]Environment and Climate Change Reseach Group (ECCG) Faculty of Architecture, Planning & Surveying, Universiti Teknologi MARA, Perlis, Arau Campus, 02600 Arau, Perlis, Malaysia- faiz524@uitm.edu.my

[5]Fakulti Kejuruteraan Awam dan Alam Sekitar, Universiti Tun Hussein Onn Malaysia, 86400, Parit Raja, Johor. - nazirah@uthm.edu.my

KEY WORDS: Airborne Gravity; Gravity Data; Marine Geoid; Shipborne Gravity; Satellite Altimeter

ABSTRACT:

Recently, satellite altimeter enables coverage of nearly 60% of the ocean surface height. Satellite altimetry has allowed the replacement of conventional marine geoid models with an advanced technique that can survey a wider coverage area and low cost. This study presents an attempt to model marine geoid from multi-mission satellite altimetry data using Least Squares Stokes' Modification Approach with Additive Corrections. Six altimetry data were used to derive the mean sea surface. The gravity anomaly was computed using planar Fast Fourier Transformation method. The optimal condition modification parameters of 4° spherical cap, 0.4 mGal terrestrial gravity data error and 0.1° correlation length were applied. Then, the additive corrections were combined with the estimated geoid to provide a precise marine geoid over Malaysian seas. Three selected levelling observations at Geting, Cendering and Pelabuhan Klang tide gauge stations were used to verify the accuracy of the computed marine geoid model. The accuracy of marine geoid model corresponds to the standard deviation, 0.098m and the root mean square error value, 0.177m. The findings suggest that the marine geoid model can be utilised for orthometric height determination in marine area. This study is significant in providing a reference frame for coastal marine observations.

I. INTRODUCTION

A. General Instructions

Marine geodesy ascertains a geodetic control network on Earth's surface that is bordered by oceans. Geodesy plays an essential role to accurately measure the position of sea surface, marine gravity field, dynamic topography and marine geoid. Geoid determination is one of the main functions of geodesy. After ellipsoid, geoid is the subsequent paramount estimation of the figure of Earth.

Recent publications have defined geoid in multiple ways. Benerjee, P. (2011) illustrates geoid as the level surface that corresponds with mean sea level (MSL) over the oceans and continents. In contrast, Jekeli, C. (2016) interprets geoid as an equipotential surface of the Earth's gravity field closely approximates with mean sea level.

The equipotential surface is described as a constant value of the gravity potential on the surface. Besides, the geoid is a level surface, which is illustrated as a closed equigeopotential surface of the gravity of the Earth closest to the Mean Sea Level (MSL) (Jalal et al., 2019). However, in MSL can be interpreted as the mean sea surface (MSS) heights.

Dynamic topography is computed based on the summation of sea level anomalies (SLA), which correspond to the deviations from sea surface height (SSH) added with mean dynamic topography, which is a part of MSS heights due to permanent currents (that is, the MSS height minus a reference geoid) (Pardo et al., 2015). SLA is estimated as SSH anomalies with respect at a temporal mean (Falcini et al., 2012).

Airborne and shipborne surveys have been conventionally used for measuring and acquiring gravity data in oceanography. Nevertheless, these gravity measurements in determining gravity field information are limited only to specific study areas due to time constraints and high cost incurred in handling the surveys. Therefore, the employment of multi-mission satellite altimeter is a better alternative that can provide comprehensive data, especially for marine geoid determination.

Satellite altimetry data can be applied to compute gravity anomalies in the marine area (Pa'suya et al., 2019a). Hence, it plays a crucial role in offering an abundance of geodetic data for marine geodesy applications. Furthermore, the quantity of data provided by satellite altimeter is also homogeneous and economical in nature. The recent launch of satellite altimeters (i.e., Jason-3 and Sentinel-3a) has presented a highly accurate measurement of sea level, which includes a wide coverage of ocean monitoring.

There are two approach methods from Remove-Compute-Restore (RCR) and Least Square Modifications with Additives Corrections (LSMSA) enable for geoid computations. Thus, in this study LSMSA approach or known as KTH method is selected as the best method used in geoid computations. One of the advantages of LSMSA method is the

applied additives corrections; downward continuation correction, atmospheric correction and ellipsoidal correction in estimating geoid that enhanced the accuracy of the regional computed geoid. Another study by Pa'suya et al. (2018) implemented the LSMSA method to estimate the gravimetric geoid although the Northern parts (Kedah and Perlis) of Peninsular Malaysia.

This study, therefore, presents an effort in determining and modelling marine geoid over Malaysian seas based on multi-mission satellite altimetry data employing LSMSA method. Therefore, the application of marine geoid is significant as a reference frame for coastal marine observations. Taking the definition of marine geoid as the surface to which tidal variations refer, geoid can therefore serve as the mean sea surface in order to define ocean depths in the immediate coastal vicinity of Malaysia.

II. MARINE GEOID DETERMINATION

A. Marine Geoid Determination Using KTH Method

This research is intended to determine the local marine geoid using multi-mission satellite altimeter and a global gravity field model over Malaysian seas covering South China Sea, Sulu Sea, Celebes Sea and Malacca Straits. The altimetry data is processed for 11-year period starting 2005 to 2015. The area under study is bounded between latitude from 0˚ up to 14˚ and longitude from 95˚ to 126˚. This study area is focused on the whole Malaysians sea covering Malacca strait, South China Sea, Celebes Sea and Sulu Sea.

The Least Squares Modification of Stokes' Formula with Additive Corrections (LSMSA) is a geoid determination approach developed by Royal Institute of Technology (KTH), Division of Geodesy & Satellite Positioning in Sweden. The additive corrections are applied to the estimated geoid that consists of the downward continuation effect, the total atmospheric correction and ellipsoidal correction.

There are two main components involved in the estimation of geoid heights which are the GGM-derived gravity anomaly from the GO_CONS_GCF_2_TIMR4 model and altimetry-derived gravity anomaly. For countries that lack their local geoid, the GGM such as GO_CONS_GCF_2_TIMR4 can be implemented as a source to provide the global geoid model for estimating the geoid heights (N) according to the WGS84 reference ellipsoid (Jalal et al., 2020). Global Geopotential Model (GGM) can be described as the mathematical model that clarifies gravitational potential in a spectral domain by using spherical harmonic expansions. Besides, the data derived from GGM provides a better medium and long wavelength part of the gravimetric geoid in terms of the quality of data; accuracy and resolution (Tugi et al., 2016 and Yazid et al., 2016).

B. Modifications Parameters

The main purpose of the modified Stokes' formula being applied is to reduce truncation errors due to the integration cap around the estimated point. It also delimited to hundred kilometres resulted from the inadequacy of land gravity data coverage (Sulaiman, 2016).

In this study, there are a few sets of initial conditions (spherical cap, terrestrial gravity data errors and correlation length) used, as represented in Table 1. This verification plays an important role in determining the modification coefficient parameters ($s_n$and b_n). Based on Table 1, one of the initial input condition parameters is changed while the remaining condition parameters are fixed.

The verification of the satisfied modification coefficient parameters is determined by validating the GPS levelling observations of tide gauge data. The satisfactory and accurate information with respect to the initial condition parameter verification is used for marine geoid estimation in the Malaysian region.

Table 1. The initial set of conditions for the determination of modification parameters.

Spherical Cap (ψ_0) (Unit: °)	**Terrestrial Gravity Data ($\sigma_{\Delta g}$) (Unit:mGal)**	**Correlation Length (ψ) (Unit:°)**
2.0	0.4	0.05
3.0	1.0	0.1
4.0	5.0	0.2
5.0	10.0	0.4

C. Estimated Marine Geoid

The Least Squares Estimator of KTH approach is employed in geoid height estimation and is composed of two main components: the selected GGM (GO_CONS_GCF_2_TIMR4) gravity anomaly and the altimetry-derived gravity anomaly. The determination of estimated geoid heights N_0^{LM} applying the modified Stokes' formula by integrating the surface gravity anomalies and the GGM gravity data is as follows:

$$N_0^{LM} = \frac{R}{4\pi\gamma}\iint_{\sigma 0} S^L(\psi)\triangle g d\sigma + c\sum_{n=0}^{M}(Q_n^L + S_n)\Delta g_n^{GGM} \quad (1)$$

Consequent to the determination of the estimated geoid heights (N_0^{LM}), the additive corrections were applied in order to obtain precise geoid heights for Malaysian seas and the determination of additive corrections such as downward continuation correction (δN_{dwc}), total atmospheric correction (δN_{tot}^a) and ellipsoidal correction (δN_{tot}^e).

.

III. VALIDATION OF MARINE GEOID MODEL

A. Data Verification with GPS Levelling at Tide Gauge Stations

The local geoid model is used for orthometric height determination using GPS levelling at tide gauge stations. Hence, orthometric height is determined by combining the ellipsoidal height (GPS height) and geoid heights. The geodetic heights provided by GPS measurements are adopted from WGS84 coordinate system. The GPS data is provided from (Nielsen et al., 2014).

In this study, the orthometric height and the geometrical geoid heights at tide gauge stations were verified to ensure the marine geoid is computed in high accuracy). Figure 1 exemplifies the numerous surfaces at a typical tide gauge station and the association is summarised as:

$$h_{MSL} = h_{GPS} - \Delta H_{Lev} + \Delta H_{MSL} \quad (2)$$

Where h_{GPS} is the GPS-derived ellipsoidal height for the tide gauge benchmark, ΔH_{Lev} is the tide gauge bench mark height above the zero-tide gauge provided by DSMM. In contrast, ΔH_{MSL} is the MSL height observed above the zero-tide gauge relying on the mean yearly MSL. In this study, ΔH_{MSL} is obtained from the mean of yearly MSL from PSMSL data starting from the year 2005 until 2015.

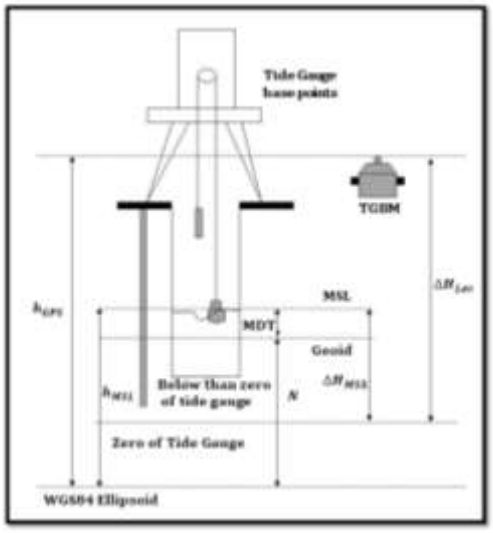

Figure 1. The relationship between various levels of the sea for geometrical geoid determination (modified from Mohamed, 2003).

The h_{GPS} and ΔH_{Lev} data are obtained from Mohamed (2003). The h_{GPS} data information referring to ellipsoidal heights are provided by TG2000 GPS campaign. Geting is a continuous permanent operating GPS station that is collocated with a tide gauge station and is a part of the MASS network. The details about h_{GPS} and ΔH_{Lev} are discussed in Mohamed (2003). Figure 2 illustrates the distribution of GPS levelling observations data at tide gauge stations adopted in this study.

Figure 2. The distributions of tide gauge stations over Peninsular Malaysia.

IV. RESULTS AND DISCUSSION

This section presents the results of this study related to marine geoid determination using multi-mission satellite altimeter. Hence, 0.1m correlation length represents the minimum RMSE value, similar to the previous spherical cap and terrestrial gravity data error evaluation. Hence, it can be concluded that 4° spherical cap, 0.4mGal terrestrial gravity error and 0.1m correlation length represent the most accurate value for geoid determination using KTH approach.

Thus, this evaluation clearly specifies that the spherical cap, terrestrial gravity data errors and correlation length evaluation are particularly significant in providing a highly accurate marine geoid model in Malaysian region using the Least Square Modification of Stokes' Formula based on the stated condition parameters. Hence, the suitable modification parameters for marine geoid computation are summarised in Table 2.

Table 2. Estimated geoid heights over Malaysian Seas.

Condition Parameters	**Value**
Spherical Cap	4°
Terrestrial Error	0.4 mGal
Correlation Length	0.1°

The final marine geoid computation involves the combination of the estimated geoid height and additive correction results using Equation (2). In geoid height determination, errors come from numerous sources and they can be expressed in terms of RMSE value. Hence, the internal errors are examined based on the mean of global mean square errors as demonstrated by Sj ö berg (1991).

The external measurements based on geometrical geoid from GPS levelling observations at tide gauge stations are utilised to provide a realistic verification of the marine geoid model accuracy. Hence, marine geoid model with the applied additive corrections (downward continuation corrections, atmospheric corrections and ellipsoidal corrections) were verified with the GPS levelling observation at Geting, Cendering and Pelabuhan Klang tide gauge stations. The elevation from GPS observation is a highly accurate (millimetre to centimetre) set of ground control points (GCPs) (Pa'suya et al., 2019b). Hence, Geting, Chendering and Pelabuhan Klang are set as GCPs in this study. The verification results are represented in Table 3.

Table 3. Verification results of the final marine geoid model with GPS levelling observations.

Marine Geoid						
Unit:m	h_{timr4}			$h_{hawtimr4}$		
TWW	Mean Error	Std Dev	RMSE	Mean Error	Std Dev	RMSE
10	0.249	0.148	0.289	0.186	0.119	0.220
40	0.121	0.129	0.177	0.207	0.125	0.241
50	**0.148**	**0.098**	**0.177**	0.154	0.102	0.185
100	0.118	0.135	0.179	0.121	0.128	0.177
110	0.127	0.144	0.192	0.132	0.139	0.192

Referring to Table 10, the verified marine geoid based on the computed h_{timr4} from tapering window width with block 50 represents the minimum standard deviation, 9.8 cm and fits

RMSE value, 17.7 cm. The map of marine geoid model over Malaysian seas is illustrated in Figure 3.

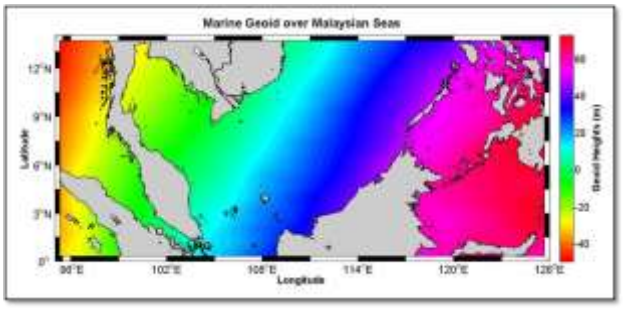

Figure 3. Marine Geoid Map over Malaysian seas.

The geoid heights slightly increase with the increasing distance on South China Sea, Sulu Sea and Celebes Sea. The geoid heights covering Peninsular Malaysia are smaller compared to Sabah and Sarawak areas. Consequently, it can be concluded that geoid heights in Malaysian seas correspond to the sea surface heights information data. The geoid heights information data increase rapidly with increasing sea surface heights data towards the South-East region.

V. CONCLUSION

Marine geoid determination plays a crucial role in many professional and scientific research. Thus, marine geoid determination from multi-mission satellite altimetry data has been generated using Least Squares of Stokes' Formula with Additive Corrections (LSMSA). Hence, three tide gauge stations from Geting, Cendering and Pelabuhan Klang were selected for the estimated geoid height evaluation.

Based on the statistical analysis, the tapering window width (TWW) with block 50 from h_{timr4} computation represents the best accuracy for marine geoid determination over Malaysian seas that fits standard deviation, 0.098 m and RMSE value, 0.177m. In conclusion, the marine geoid over Malaysian seas can be utilised to address the orthometric heights for surveying and mapping purposes as well as engineering applications in marine area. The applications of geoid model highly demanding as well as it is a vertical reference datum measurement for engineering works (Ming et al., 2021).

ACKNOWLEDGEMENTS

The authors would like to acknowledge the Ministry of Higher Education (MOHE) under the Fundamental Research Grant Scheme (FRGS) Fund, Reference Code: FRGS/1/2020/WAB07/UTM/02/3 (UTM Vote Number: R.J130000.7852.5F304) for funding this study.

REFERENCES

Dubayah, R.O., Swatantran, A., Huang, W., Duncanson, L., Tang, H.,Johnson, K.,Dunne, J.O., and Hurtt, G.C., 2017. CMS: LiDAR-derived Biomass, Canopy Height and Cover, Sonoma County, California, 2013. ORNL DAAC, Oak Ridge, Tennessee, USA https://doi.org/10.3334/ORNLDAAC/1523.

Banerjee P., (2011). Geoid, In Gupta H.K., (Ed.), Encyclopedia of Solid Earth Geophysics, Encyclopedia of Earth Sciences Series, Springer Science & Business Media B.V. 2011, p. 353.

Falcini, F., Jerolmack, D. J., & Nardelli, B. B. (2012). Mississippi River and Sea Surface Height Effects on Oil Slick Migration, 7(4) 2-8, http://doi.org/10.1371/journal.pone.0036037.

Jalal, S.J., Musa, T.A., Ameen, T.H., Din, A.H.M., Aris, W.A.W. & Ebrahim, J.M. (2020). Optimizing the Global Digital Elevation Models (GDEMs) and accuracy of derived DEMs from GPS points for Iraq's mountainous areas. Geodesy and Geodynamics, 2020, 11(5), pp. 338–349.

Jalal, S.J., Musa, T.A., Md Din, A.H., Aris W.A.W., Shen, W. & Pa'suya, M.F. (2019). Influencing factors on the accuracy of local geoid model. Geodesy and Geodynamics, 2019, 10(6), pp. 439–445.

Ming, T.K., Amin, Z.M., & Din, A.H.M. (2021). Least square modification of stokes formulae with additive corrections estimator for klang valley geoid modelling. IOP Conference Series: Earth and Environmental Science, 2021, 620(1), 012016.

Nielsen, J. E., Forsberg, R. Olesen, A. V, Jensen, Tim, Becker, D (2014). Sabah offshore airborne geophysics campaign 2014 (MAGIC/ Marine Cadastre Phase 1, Final Contact report (ver 2) (Unpublished).

Pardo, M. A., Gerrodette, T., Beier, E., Gendron, D., Forney, K. A., Chivers, S. J., Federal, D. (2015). Inferring Cetacean Population Densities from the Absolute Dynamic Topography of the Ocean in a Hierarchical Bayesian Framework, 1–23. http://doi.org/10.1371/journal.pone.0120727.

Pa'suya, M. F., Din, A. H. M., Amin, Z. M., Rusli, N., Othman, A. H., Aziz, M. A. C., & Samad, M. A. A. (2018). Accuracy Assessment of TanDEM-X DEM and Global Geopotential Models for Geoid Modeling in the Southern Region of Peninsular Malaysia. In Proceedings of the Second International Conference on the Future of ASEAN (ICoFA) 2017 – Volume 2 (pp. 91–100). Springer Singapore. https://doi.org/10.1007/978-981-10-8471-3_9.

Pa'suya, M. F., Din, A. H. M., McCubbine, J. C., Omar, A. H., Amin, Z. M., & Yahaya, N. A. Z. (2019a). Gravimetric Geoid Modelling Over Peninsular Malaysia Using Two Different Gridding Approaches For Combining Free Air Anomaly. International Archives of the Photogrammetry, Remote Sensing and Spatial Information Sciences - ISPRS Archives (Vol. 42, pp. 515–522). International Society for Photogrammetry and Remote Sensing https://doi.org/10.5194/isprs-archives-XLII-4-W16-515-2019

Pa'suya, M. F., Bakar, A. F. A., Din, A. H. M., Aziz, M. A. C., Samad, M. A. A., & Mohamad, M. I. (2019b). Accuracy assessment of the tandem-X DEM in the Northwestern Region of Peninsular Malaysia using GPS-levelling. ASM Science Journal, 12(Special Issue 2), 100–106.

Sjöberg, L. E. (1991). Refined least squares modification of Stokes' formula. *Manuscripta Geodaetica*, 16, 367-375.

Sulaiman, S.A. (2016). *Gravimetric Geoid Model Determination for Peninsular Malaysia Using Least Squares*

Modification of Stokes, Doctor Philosophy, Universiti Teknologi Mara, Shah Alam.

Tugi, A, Din, A. H. M., Omar, K. M., Mardi, A. S., Som, Z. A. M., Omar, A. H., Yahaya, N. A. Z., & Yazid, N. M. (2016). Gravity Anomaly Assessment Using GGMs and Airborne Gravity Data towards Bathymetry Estimation. International Archives of the Photogrammetry, Remote Sensing and Spatial Information Sciences. XLII-4(W1): 287-297.

Yazid, N. M., Din, A. H. M., Omar, K. M., Som, Z. A. M., Omar, A. H., Yahaya, N. A. Z., & Tugi, A. (2016) Marine Geoid Undulation Assessment Over South China Sea Using Global Geopotential Models and Airborne Gravity Data. International Archives of the Photogrammetry, Remote Sensing and Spatial Information Sciences. XLII-4(W1): 253-263.

SPATIO-TEMPORAL VARIATION OF OCEAN TIDE LOADING OVER MALAYSIAN REGION

Nur Surayatul Atikah Alihan[1*], Dudy Darmawan Wijaya[3] and Ami Hassan Md Din[1,2*]

[1] Geomatics Innovation Research Group (GnG), [2] Geoscience and Digital Earth Centre (INSTEG), Faculty of Built Environment and Surveying, Universiti Teknologi Malaysia, 81310 Johor Bahru, Johor, Malaysia.
*nsatikah99@gmail.com; *amihassan@utm.my
[3] Geodesy Research Group, Faculty of Earth Sciences and Technology, Institute of Technology Bandung, Bandung, Indonesia.

KEY WORDS: KPPP GPS; Malaysian Region; Ocean Tide Loading; Spatio-temporal Variation

ABSTRACT:

Ocean tide loading is one of the factors that were contributing to the deformation of solid earth. The tidal ground displacement due to the variability of the ocean is the secondary tidal effect after the earth body tide as the magnitude of the ocean tide loading can be larger upon the station is near the coastal area. Conventionally, various instruments are used to estimate the tidal ground deformation accurately such as gravimeter, tiltmeter and strainmeter. Nevertheless, the use of these instruments leads to the high-cost operation and sparse distribution of stations. This study is conducted to estimate the spatio-temporal variation of the ocean tide loading over the Malaysian region, using a Kinematic Precise Point Positioning (KPPP) GPS approach. Continuous GPS observations along the year 2013 have been utilized to observe diurnal, semi-diurnal and long-term periods of the tidal constituents by employing the harmonic analysis. The ocean tide loading derived from the KPPP GPS correlates well with the predictions of the theoretical model; NAO.99b with the average correlation coefficient above 0.90 and root mean square error is less than ± 1 cm at horizontal and vertical components. This study is beneficial in providing tidal information to improve the geodetic measurements as well as it can be used to study the impact of the tidal variations towards the geophysical phenomenon such as earthquakes, tsunami and volcanic activity.

I. INTRODUCTION

The earth's crust undergoes periodic displacements due to the gravitational attraction between the moon and the sun, temporally varying atmospheric, surface loads, oceanic and continental water mass. The deformation of solid earth due to the variability of ocean tide is known as ocean tide loading, which arising from the gravitational attractions between the moon and sun acting upon the rotation of the earth. These tidal ground displacements are the secondary tidal effect after the earth body tide as the magnitude of the ocean tide loading is smaller than the magnitude of the earth body tide. The magnitude of ocean tide loading is usually around the millimetre (mm) level of displacement and more than 1 cm can be achieved when the geodetic stations are located very close to the shore (Pagiatakis, 1988; Héroux and Kouba, 2001; Zheng, 2007; Subirana et al., 2013).

The gravitational force and ocean tide water movement periodically load and unload the earth causing changes in displacement, tilt, and gravity. The displacement due to the ocean tide loading affects the coordinate system and has gained importance in geodesy as the high precision of space geodetic measurements (e.g. GPS, VLBI, Doppler Orbitography and Radiopositioning Integrated by Satellite (DORIS) and Altimeter) required the correction from the tidal effects to maximize their extensive use in geodesy and geophysical studies such as monitoring the variations of mean sea level and quantifying the vertical land motion. Thus, to increase the accuracy of satellite positioning and geodetic measurement techniques to sub-millimeter level, a good knowledge of tidal deformation is imperative.

The tidal response is usually measured by several types of instruments such as super-conducting gravimeters, strainmeter and tilt observations. The rising operational cost, the scarce distribution of station as well as the complexity of accessing the best location for low-noise site, however, cause contradictory observations to disclose the spatial heterogeneity of the solid earth tidal field (Ito et al., 2009). Therefore, the utilising of the precise space geodetic approaches such as GPS will provide the continuity of observations in the study of the interior of the earth from the surface observations of the loading effects (Penna et al., 2015; Alihan et al., 2019a; Matviichuk et al., 2020).

II. DATA AND METHODOLOGY

A. GPS Data Observations

In this study, a GPS Continuously Operating Reference Station (CORS) from MyRTKnet operated by Department of Survey and Mapping Malaysia (DSMM) as shown in Figure 1 is utilised. As many as 70 stations are used from 1st January to 31st December 2013 over Malaysian region.

Figure 1. The distribution of MyRTKnet stations.

B. GPS Data Processing

An open-source software RTKLIB with Comment User Interface (CUI) is used for GPS data processing. This software is compatible with scientific studies in surveying fields that require standard and precise positioning. The Kinematic Precise Point Positioning (KPPP) method is used in this study in order to estimate the ocean tide loading signal in GPS observations. Otherwise, the signal would be omitted or reduced if the approach used is differential GPS positioning since the relative positioning technique can frequently minimize or eradicate the effects of ocean tide loading if the stations are relatively close to each other (Milbert, 2017; Alihan et al., 2019b).

In order to construct daily solution data, the GPS data processing strategies involve the data preparation of the 30 second data sampling with the 10-degree elevation of mask angle to increase the number of observations. Furthermore, the parameter of the precise ephemeris (.SP3), IGS Earth Rotation Parameter (.ERP), IGS final clock with sampling rate 30s (.CLK) and Differential Code Bias (.DCB) is applied into the processing strategies of the zero-difference measurements to reduce the noise that affects the appropriate signal in the GPS observations. The measurement models such as the satellite and receiver antenna phase variation center (.ATX), phase windup correction, Ionosphere-free linear combination with dual frequency and approximate total zenith delays and horizontal gradient parameters for troposphere correction was subsequently used in the KPPP GPS processing. Then, the static integer ambiguities are continuously estimated and resolved using the fix and hold strategy. Table 1 summarizes the processing strategies used in this study.

Table 1. The KPPP GPS processing strategies.

Processing Parameters	Processing Strategy
Availability Data	1st January 2013 – 31st December 2013
Input data	Daily
Elevation cut-off angle	10°
Sampling rate	30 second
Ionosphere correction	Ionosphere-Free (IF) linear combination
Troposphere correction	Estimated ZTD + Grad
Satellite Ephemeris/Clock	Precise
Integer Ambiguity Resolution	Fix and Hold

C. Estimation of Ocean Tide Loading based on KPPP GPS Solutions

There are two (2) configurations in the processing strategy to determine the signal of ocean tide loading. The first configuration includes the processing strategy applying earth body tide correction using IERS2003 model, while the second configuration comprises the processing strategy that applying both earth body tide and ocean tide loading corrections using IERS2003 and FES2012 model. The ocean tide loading derived from the KPPP GPS is determined by the difference of KPPP GPS solutions between these configurations where these observations are acquired from the output of the ocean tide loading model and model error as presented in equation (1):

$$\widehat{OTL} = \overline{OTL} + \varepsilon_{\overline{OTL}} \quad (1)$$

where $\widehat{OTL}$ = ocean tide loading derived from KPPP GPS
$\overline{OTL}$ = ocean tide loading model, FES2012
$\varepsilon_{\overline{OTL}}$ = ocean tide loading model error

D. Tidal Analysis

The periodic measurement data from the periodic phenomena contain the composition of the periodic signals. In this study, the assessment of the tidal analysis is divided into two parts, (1) tidal harmonic analysis and (2) tidal spectral analysis.

The tidal harmonic analysis is conducted to estimate the amplitude and phase of the tidal constituents from ocean tide loading at 70 MyRTKnet stations. The harmonic analysis decomposes the periodic function or periodic signals into the sum of a set of simple oscillating functions known as sine and cosine functions. The basic equation of this method is as follows (Katznelson, 2004; Guo et al., 2018):

$$f(t) = A_o + \sum_{n=1}^{\infty} A_n \cos(\omega_n t - \theta_n) \quad (2)$$

where A_o = the coefficient
n = the tidal constituents
A_n = the amplitude of the tidal constituent n
ω_n = the angular frequency of the tidal constituent n
t = time epoch
θ_n = the phase of the tidal constituent n

Further, the tidal spectral analysis is conducted using Fast Fourier Transform (FFT) method to examine the characteristics of the ocean tide loading over the Malaysian region.

III. RESULTS AND DISCUSSION

A The Correlation of Ocean Tide Loading based on KPPP GPS and NAO.99b Model

The validation of ocean tide loading is computed based on the ocean tide loading observation from the KPPP GPS solutions and the prediction from the ocean tide model, NAO.99b. Based on the findings, the validation of ocean tide loading depicts a similar trend and possess the strong data argument between the ocean tide loading derived from KPPP GPS solution and NAO.99b model. Figure 2 shows the trend of ocean tide loading at CAME station where the magnitude of north and east component is around 0.5 cm while the magnitude of ocean tide loading at up component is approximately 2 cm.

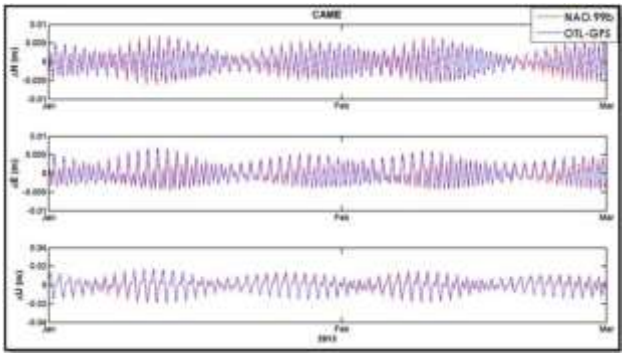

Figure 2. The trend of ocean tide loading at CAME station.

The linear regression by least square approach is used in quantifying the strength and the direction of the linear relationship between the ocean tide loading observed by KPPP GPS and the predictions of the theoretical model, NAO.99b. The average correlation of coefficient for 70 stations over the Malaysian region is approximately 0.9493, 0.9379 and 0.9455 at north, east and up component, respectively, with the average mean bias equivalent to 4.55 x 10^{-5} cm at north component, 2.95 x 10^{-5} cm at east component and 5.33 x 10^{-4} cm at up component. The average RMSE of ocean tide loading validation is around ± 0.0938 cm at north component, ± 0.1208 cm at east component and ± 0.4138 cm at up component.

B. The Amplitude and Phase of Tidal Constituents

Since ocean tide loading is periodic phenomena that contain the composition of the periodic signals, harmonic analysis is used as the mathematical approach to determine the amplitude and phase of the tidal constituents. The coefficient parameters of the harmonic analysis are applied to estimate the amplitude and phase of primary tidal constituents that consist of semi-diurnal tide, diurnal tide and long-term period tide. In this study, a total of 11 tidal constituents Ssa, Mm, Mf, Q1, O1, P1, K1, N2, M2, S2 and K2 are well produced by the ocean tide loading observations. Table 2 tabulated the average amplitude and phase of tidal constituents for 70 stations of MyRTKnet stations.

Table 2. The average amplitude and phase of tidal constituents for 70 stations of MyRTKnet.

		Ocean Tide Loading		
		N-S	**E-W**	**Up**
Ssa	**Amplitude (cm)**	0.0036	0.0051	0.0389
	Phase (º)	72.2596	202.9022	330.7818
Mm	**Amplitude (cm)**	0.0022	0.0033	0.0621
	Phase (º)	145.8898	186.1991	270.2432
Mf	**Amplitude (cm)**	0.0032	0.0091	0.0876
	Phase (º)	136.7093	187.6409	216.5143
Q1	**Amplitude (cm)**	0.0138	0.0253	0.1389
	Phase (º)	267.2249	199.9567	34.5596
O1	**Amplitude (cm)**	0.0741	0.1158	0.6411
	Phase (º)	171.8383	282.6485	135.6797
P1	**Amplitude (cm)**	0.0451	0.0521	0.2567
	Phase (º)	248.5332	157.1912	95.2436
K1	**Amplitude (cm)**	0.1315	0.1549	0.8031
	Phase (º)	254.6556	159.7530	95.4763
N2	**Amplitude (cm)**	0.0419	0.0482	0.1270
	Phase (º)	174.3589	69.9807	196.4585
M2	**Amplitude (cm)**	0.1776	0.2291	0.5801
	Phase (º)	248.9265	140.1210	265.5468
S2	**Amplitude (cm)**	0.0693	0.0863	0.1880
	Phase (º)	144.7760	132.1995	169.2080
K2	**Amplitude (cm)**	0.0256	0.0283	0.0630
	Phase (º)	255.9629	196.9787	292.2332

Referring the Table 2, the ocean tide loading is dominated by M2 constituent, followed by K1, O1 and S2 constituents at both northing and easting components. Meanwhile, the tidal constituents of K1 are most significant at up component, followed by M2, O1 and S2 constituents.

C. The Spatio-temporal Variation of Ocean Tide Loading Over Malaysian Region

The variability of ocean tide is generated from the gravitational attraction of the moon and sun towards the earth's rotation. Rather than the sun, it is the moon that has a greater influence on the tidal displacements on the earth as the distance between

the moon and the earth are relatively small. Therefore, the spatio-temporal of ocean tide loading is computed during the perigee phenomena, where the lunar orbit is the closest distance to the earth. Figure 3 indicated the propagation of the ocean tide loading for every six hours at up component. The findings show that the MyRTKnet stations are displaced due to the ocean tide loading within -3.2 cm subsidence and 2.4 cm uplift.

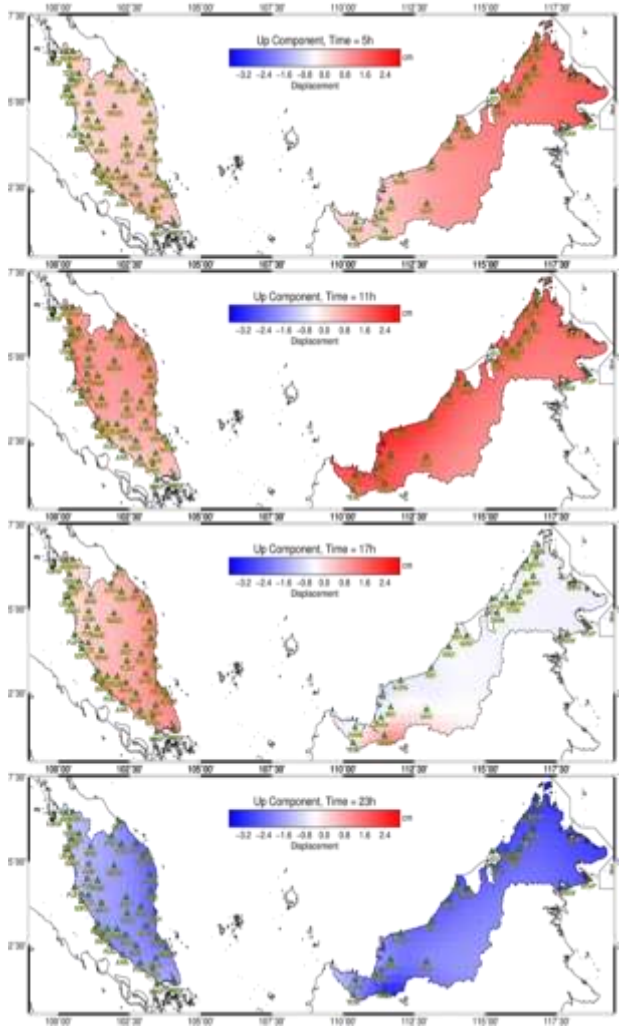

Figure 3. The propagation of the ocean tide loading displacement for every six hours at up component from time 05:00:00 hour to 23:00:00 hours during perigee phenomenon. X-axis is longitude and the Y-axis is latitude. Red and blue colours indicate uplift and subsidence of MyRTKnet stations, respectively.

IV. CONCLUSION

Ocean tide loading plays a role in geodetic measurements that required the accurate removal of the tidal signal. In this study, the behaviour of the ocean tide loading is presented in the spatio-temporal of climatology maps over Malaysian region, which generated based on the estimation of the tidal parameters from the tidal harmonic analysis at 70 MyRTKnet stations. Based on the harmonic analysis, a total of 11 primary tidal constituents are well produced by the ocean tide loading observations.

ACKNOWLEDGEMENT

The authors would like to express their gratitude to the Department of Surveying and Mapping Malaysia (DSMM) for providing valuable MyRTKnet data for the usage of this study. This research project is funded by the Ministry of Higher Education (MOHE) under the Fundamental Research Grant Scheme (FRGS) Fund, Reference Code: FRGS/1/2020/WAB05/UTM/02/1 (UTM Vote Number: R.J130000.7852.5F374).

REFERENCES

Alihan, N.S.A., Wijaya, D.D., Din, A.H.M., Bramanto, B., Omar, A.H. (2019a). Spatiotemporal variations of earth tidal displacement over Peninsular Malaysia based on GPS observations. Lecture Notes in Civil Engineering, 2019, 9, pp. 809–823.

Alihan, N.S.A., Wijaya, D.D., Din, A.H.M., Omar, A.H. (2019b). The presence of geophysical loadings in GPS observations using general least squares approaches. International Archives of the Photogrammetry, Remote Sensing and Spatial Information Sciences - ISPRS Archives, 2019, 42(4/W16), pp. 101–107.

Guo, Z., Pan, H., Cao, A., and Lv, X. (2018). A harmonic analysis method adapted to capturing slow variations of tidal amplitudes and phases. Continental Shelf Research. 164 37-44.

Héroux, P., and Kouba, J. (2001). GPS precise point positioning using IGS orbit products. Physics and Chemistry of the Earth, Part A: Solid Earth and Geodesy. 26 (6), 573-578.

Ito, T., Okubo, M., and Sagiya, T. (2009). High resolution mapping of Earth tide response based on GPS data in Japan. Journal of geodynamics. 48 (3-5), 253-259.

Katznelson, Y. (2004). An introduction to harmonic analysis. 3rd Edition. United Kingdom: Cambridge University Press.

Matviichuk, B., King, M., and Watson, C. (2020). Estimating ocean tide loading displacements with GPS and GLONASS. Solid Earth. 11 (5), 1849-1863.

Milbert, D. (2017). Solid Earth Tide. Retrieved from http://geodesyworld.github.io/SOFTS/solid.htm

Pagiatakis, S. D. (1988). Ocean tide loading on a self-gravitating, compressible, layered, anistropic, viscoelastic and rotating earth with solid inner core and fluid outer core. Degree of Doctor of Philosophy. Department of Surveying Engineering, University of New Brunswick, Fredericton, N. B. Canada.

Penna, N. T., Clarke, P. J., Bos, M. S., and Baker, T. F. (2015). Ocean tide loading displacements in western Europe: 1. Validation of kinematic GPS estimates. Journal of Geophysical Research: Solid Earth. 120 (9), 6523-6539.

Subirana, J. S., Zornoza, J. M. J., and Hernández-Pajares, M. (2013). GNSS data processing, Vol. I: Fundamentals and algorithms. Netherlands: ESA Communications.

Zheng, Y. (2007). Generation of network-based differential corrections for regional GNSS services. Degree of Doctor of Philosophy. Faculty of the Built Environment and Engineering, Queensland University of Technology, Australia.

LONG-TERM DATASETS OF WIND ROSE DIAGRAM AND WAVE SCATTER TABLE TO SUPPORT OCEAN RENEWABLE ENERGY IN THE SOUTHERN REGION OF SOUTH CHINA SEA

Uti, M. N. [1*], Din, A. H. M. [1,2*], Hashim, F. E.[3], Yaakob, O. [3], Idris, N. H. [4], Yusof, N. [4], Idris, N. H. [4], Razak, N. A. [1],Dzulkarnain, S. [1], Hamid, A. I. A. [1], Siang, K. H.[3]

[1] Geomatics Innovation Research Group (GnG), [2]Geosciences and Digital Earth Centre (INSTEG), Department of Geoinformation, Faculty of Built Environment and Surveying, Universiti Teknologi Malaysia, 81310 Skudai Johor, Malaysia – (amihassan@utm.my, mnizam65@graduate.utm.my)

[3] School of Mechanical Engineering, Faculty of Engineering, Universiti Teknologi Malaysia, 81310 Johor Bahru, Johor, Malaysia[4] Tropical Map Research Group, Faculty of Built Environment and Surveying, Universiti Teknologi Malaysia, 81310 Johor Bahru, Johor, Malaysia.

KEY WORDS: Ocean Renewable Energy; Satellite Altimeter; Wave Period; Wind Rose Diagram; Wave Scatter Diagram

ABSTRACT:

Satellite altimeter has shown its capability in providing reliable information for ocean energy studies. But, existing techniques suchas Volunteer Observing Ships, buoy and numerical models contain limitations in the spatial and temporal domain in providing reliable long-term datasets. The aim of this study is to produce a wind rose diagram and wave scatter table in the Southern Region of South China Sea using long-term datasets from multi-mission of satellite altimeter. Radar Altimeter Database System (RADS) is used to extract the wind speed and significant wave height for 25-year (1993 to 2017) with the additional derivation of wind direction wave period. A wind speed validation with buoy presents a good correlation and RMSE of 0.66 and 0.95 m/s, respectively. In contrast, altimeter significant wave height shows a good value correlation of 0.72 and 0.88 m for RMSE. The wind rose diagram showing during the Northeast monsoon recorded the highest value of wind speed up to 8 m/s. Using the Fara-U method, the wave scatter table presents a low significant wave height between 0.1 m to 1.5 m while the peak wave period is ranging between 2 s to 6 s. In conclusion, both winds rose diagram and wave scatter table can provide a reliable value that suitable for energy derivation to support ocean renewable energy in Malaysia.

I. INTRODUCTION

The implementation of five-fuel diversification strategy energy mix in Malaysia in 1999 has been the starting point for the study of renewable resources in Malaysia (Hashim, 2016 and Shamsuddin, 2012). Renewable energy in Malaysia is divided into three, namely solar energy, wind energy and ocean energy. In two decades, satellite altimeter has proven to be one of the important tools in providing good quality of data in the oceanographic study in terms of spatial and temporal resolution. By using multi-mission long-term data, satellite altimeter has proven capable of extracting different types of information such as sea level, wave height, wind speed above the sea surface etc. (Wan et al 2014).

A. Research Background

Numerous studies have been done to assess Malaysia's capability in harvesting ocean energy. Various methods were used from conventional to advanced technologies, and some even combine these methods. For example, a study by Nasir et al. (2017) has proved the ability of Terengganu and Sarawak waters as hot-spot areas to produce an average of 2.8 kW/m to 8.6 kW/m of wave energy density. A study conducted by Zaman et al. (2019) proved that the altimetry technique is able to provide reliable and large coverage of wind data. This study also identified Terengganu coastlines, Labuan and Sabah were the potential to generate up to 5kWh/m^2/year. A study by Hashim etal. (2020) using the satellite altimeter data concludes theoretically that Malaysia is capable of offshore wind energy, especially in Borneo water with an annual wind energy density above 500 kWh/m^2.

B. Satellite Altimeter Principle

Generally, a satellite altimeter transmits signals to the Earth surfaces (ocean, land, ice, river, etc.) and receives back the echoes. The basic principle of satellite altimeter is based on the simplest understanding that time is a distance (Din et al. 2014). A precise measurement of the time taken to make the round trip are derived between the satellite and the surface.

II. DATA AND METHODS

A. Data source and Data Analysis

This study area broadens from 0˚N to 14˚N and 95˚E to 125˚E that includes Malacca Straits, South China Sea, Celebes Sea and Sulu Sea as shown in Figure 1. Commonly, Malaysia experienced two major monsoons known as Northeast monsoon (Nov-Feb) and Southwest monsoon (May-Aug). A seasonal assessment is carried out. So, a 25-year (1993-2017) of wind speeds and significant wave height data were extracted from series of satellite altimeter using Radar Altimeter Database System (RADS) with a posting of 1Hz resolution and 0.25˚ x 0.25˚ spatial resolution as shown in Figure 1.

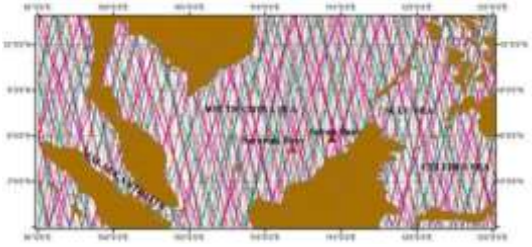

Figure 1. Study area and altimetry mission track

For validation parts, correlation coefficient (*r*) and trend graph were generated as well as the calculation of root mean square error through the comparison of the altimeter and buoy measurement. The buoy stations are located at Sabah sea (5.83 N, 114.39 E) and Sarawak sea (5.15 N, 111.82 E). The RMSE will indicate the accuracy of the altimetry measurements. This calculation is performed by measure the differences between measured (*a*) and observed (*b*) values as shown in equation (1).

$$\text{RMSE}=\sqrt{\frac{\sum_{i=1}^{n}((a)-(b))^2}{n}} \qquad (1)$$

Where n = Total number of observation
a = Altimeter
b = Buoy significant wave height

In-situ measurements act as a benchmark for the assurance of the altimeter measurements (Kumar et al, 2015). The abundance of studies has proved the reliability of altimeter derived wind speed and significant wave height parameters with buoy data (Shanas et al., 2014; Zaman et al. 2019; Yang and Zhang, 2019).

B. Wind Rose Diagram and Wave Scatter Table

The main part of this study is the construction of the wind rose diagram and wave scatter diagram. The wind rose diagram can be described as a graphic tool that contains information on wind speeds and directions at a particular location. While wave scatter table provides tabulated information of significant wave height and wave zero crossing period. To produce wave scatter table, estimation of wave period, *T* is needs to be done. Numerous algorithms were produced. However, due to the variety of ocean environments, there are pros and cons in choosing a suitable approach. Most of the algorithms were not suitable to use in the Malaysia sea due to weather conditions and water properties (Hashim, 2016). To encounter this effect, Fara-U algorithm (equation 2 and 3) developed by Hashim (2016) is used to estimate the wave period, T_z at Malaysian seas.

$$T_z = 1.299_a - 1.127 \qquad (2)$$

$$a = 2.247 + [(4.947+25.399\ H_s)/\ (7.562 + H_s + U)] \qquad (3)$$

Where T_z = Wave period (s)
H_s = Significant wave height (m)
U = Wind speed (m/s)

The wind rose and wave scatter table is normally used in forecasting. However, through time this method has also been applied in renewable energy assessment such as (Nasab et al. 2020; Salam et al. 2018; Yong et al. 2014). In this part, 16 zones (60nm x 60nm) were selected to produce wind and wave diagrams, as shown in Figure 2.

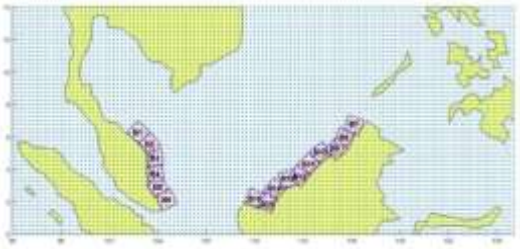

Figure 2. 16-bin selection of desired areas

III. RESULTS AND DISCUSSION

A. Validation

Observed data from the satellite altimeter is compared with the buoy measurements in the Sabah and Sarawak sea based on the buoy time frame. (Sabah buoy- December 2004 to December 2007; Sarawak buoy- January 2009 to January 2012). Kumar et al. (2015) explained that comparison of altimeter and buoy requires good consideration in terms of spatial and temporal aspects. Both of the buoy stations coincided within the altimeter tracks with not more than 50km radius as implementedin a previous study (Uti et al. 2018). By far, no altimeter mission has been designed to monitor the inland or ground areas. Thus, the surrounding topography like the presence of land or shallow water always corrupts the returned radar signal (Uti et al. 2017). Table 1 presents the results of the correlation coefficient, *r* and RMSE.

Table 1. Summary of RMSE and correlation results for wind speed and significant wave height.

Buoy	Parameter	RMSE	*r*
Sabah	Wind speed	0.66 m/s	0.89
	Significant wave height	0.19 m	0.72
Sarawak	Wind speed	0.95 m/s	0.82
	Significant wave height	0.2 m	0.88

B. Seasonal Assessment

There are two major seasonal effects which are northeast monsoon (Nov-Feb) and southwest monsoon (May-Aug). Monsoon occurs due to the difference in temperature caused by the sun's radiation and movement of heat between the land and ocean across the continents.

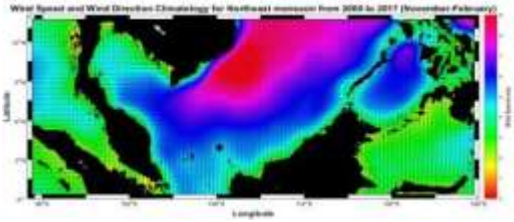

Figure 3. Wind speed and wind direction during northeast monsoon

Northeast monsoon happened due to the movement of wind from the northeast direction, as shown in Figure 3. It happened from Nov-Feb. Strong wind speeds up to 9 m/s occurred at the center of South China Sea and north of Sulu Sea. As the wind-blown towards the northeast, east-coast of Peninsular; north-coast of Sabah and Sarawak received strong wind up to 6 m/s. While the west-coast of Peninsular (Malacca Straits) and Celebes sea possessed low movement of wind (less than 4 m/s) because the winds are blocked by the Sumatra Islands near the Malacca

Straits and the Sulu islands in Celebes Sea. During the southwest monsoon (Figure 4), the movement of wind from the southwest region has deflected the wind strength in Malacca Straits, Sulu Sea and Celebes Sea (below 4 m/s). A sudden change of wind also happened at the center of South China Sea,which most of the area experienced 5-8 m/s of wind.

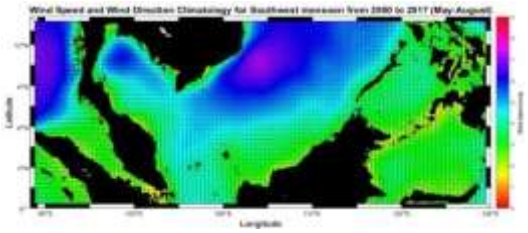

Figure 4. Wind speed and wind direction during southwest monsoon

Figure 5 and 6 show the condition of significant wave height during the northeast monsoon and southwest monsoon.

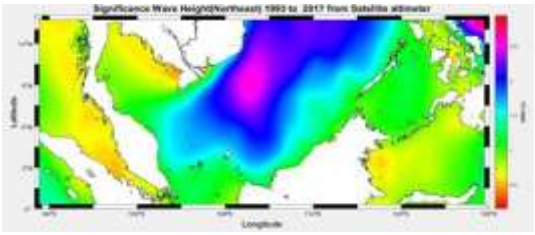

Figure 5. Significant wave height during northeast monsoon

Figure 5 illustrated the distribution of significant wave height during Northeast monsoon. Southern South China Sea experienced up to 2.5m compared to Celebes Sea and Sulu Sea with 0.4m and 1.4m, respectively. Among all the Malaysian Malacca straits experienced low significant wave height, which is 0.6 m. As the wave moves downward from South China Sea in northeast direction, east-coast of Peninsular Malaysia, north-coast of Sabah and Sarawak experienced up to 1.5m of waves. While, during the southwest monsoon (Figure 6), the condition of the wave is much lower, even the center of South China Sea can reach a maximum of 1m. Most of the coastal regions at Malaysian sea experienced up to 0.6m of waves. But as the waves hit the coast (20km from the shore), the water becomes shallower, but the waves were gradually increased (up to 1m) due to the dynamic of the nearshore and the presence of long wave groups (Ardhuin and Orfila, 2018).

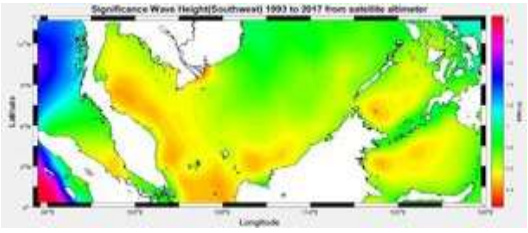

Figure 6. Significant wave height during southwest monsoon

C. Wind Rose Diagram

Based on Figure 2, 16-bin were selected to be assessed. Table 2 presents the summary of long-term wind speed analysis throughout 18-year altimeter observation. Therefore, three locations possessed great average wind speeds and potential for offshore wind energy; B3 (4.07 m/s), B4 (3.9 m/s) and B7 (3.92 m/s).

Bin	Wind speed (m/s)			Bin	Wind speed (m/s)		
	min	max	average		min	max	average
B1	0.99	7.80	3.35	B7	1.23	7.47	3.92
B2	1.09	8.38	3.73	B8	1.14	7.50	3.47
B3	1.41	8.14	4.07	B9	1.01	7.51	3.33
B4	1.36	8.29	3.94	B10	1.00	7.74	3.65
B5	1.11	8.19	3.55	B11	1.01	7.38	3.31
B6	1.06	8.74	3.67	B12	0.94	7.31	3.17
Bin	Wind speed (m/s)			Bin	Wind speed (m/s)		
	min	max	average		min	max	average
B13	0.99	7.46	3.04	B15	1.01	9.89	2.66
B14	0.94	8.24	2.69	B16	1.22	8.07	3.16

Table 2. Summary of wind speed long-term analysis for 16-bin

This analysis also explained that east-coast of Peninsular Malaysia (B2-B6) experienced maximum wind speed up to 9 m/s, which is stronger than Sabah and Sarawak coasts.

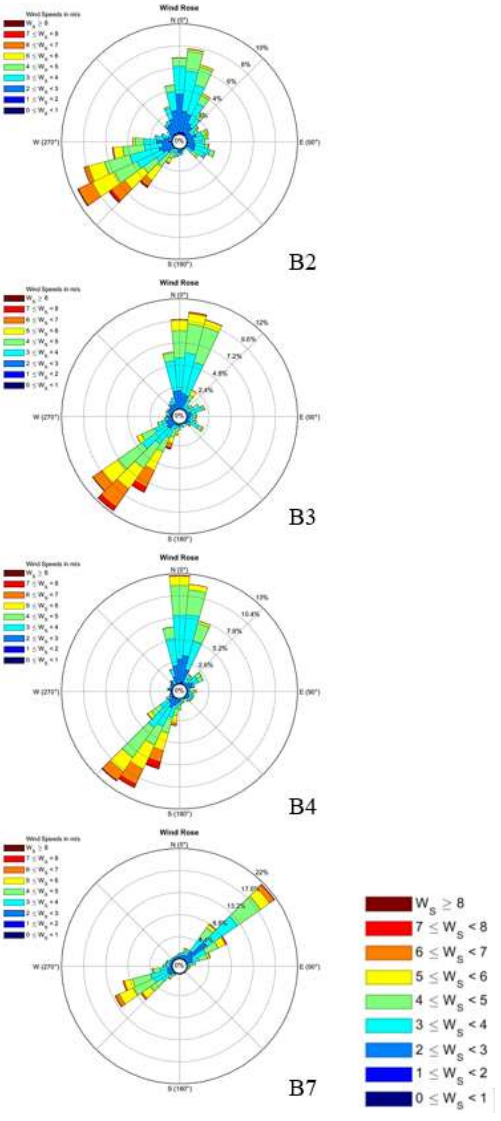

Figure 7. The wind rose diagram of 16-bin for 18-year data

Based on Figure 7, present the wind rose diagram for each bin. Constantly, B1-B7 and B10-B11 experienced more than 5m/s of wind speed compared to other bins. Even though B1- B7 have experienced greater wind, only B7 shows the highest frequency of wind with 22%, but most of the time B7 region received wind speeds within the range of 3-4m/s, while B1-B6 the frequency of wind is below 15% but experienced more than 5m/s of wind speed. When the wind moves in northeast direction (southwest monsoon), each bin received low windspeed, which is below 7m/s as shown in B14, B15 and B16. Therefore, three potential locations have been identified for offshore wind energy, which is B3-B4 (Terengganu) and B7 (north-coast of Sabah).

D. Wave Scatter Table

Scatter diagrams or contingency tables are built upon the accumulated data of significant wave height and average zero-up-crossing period that have been collected regularly over a period of time, often at 3- or 6-hour intervals. According to Jadidoleslam et al. (2016), for any practical application of wave energy extraction, it is necessary to know the contribution of each sea state for wave energy. This scatter table is necessarily used for wave energy converter (WEC) production (Pastor et al. 2015). Table 3 summarises the dominant and average sea state for all zones.

Table 3. Summary of significant wave height and wave period long-term analysis for 16-bin

Bin	Dominant sea state		Average	
	H_s (m)	Wave period, T_p (s)	H_s (m)	Wave period, T_p (s)
1	0-1.5	3-6	0.80	4.58
2	0-1.5	3-6	0.91	4.75
3	0-1.5	3-6	0.91	4.70
4	0-1.5	3-6	0.83	4.51
5	0-1.5	3-6	0.81	4.56
6	0-1.5	3-6	0.82	4.60
7	0-1.5	3-5	0.87	4.63
8	0-1.5	3-6	0.82	4.63
9	0.5-1.5	3-6	0.86	4.74
10	0-1.5	3-6	0.88	4.72
11	0.5-1.5	3-6	0.84	4.70
12	0-1.5	3-6	0.81	4.66
13	0-1.5	3-6	0.81	4.67
14	0-1.5	3-6	0.78	4.70
15	0-1.5	2-6	0.88	5.0
16	0-1.5	3-6	0.85	4.74

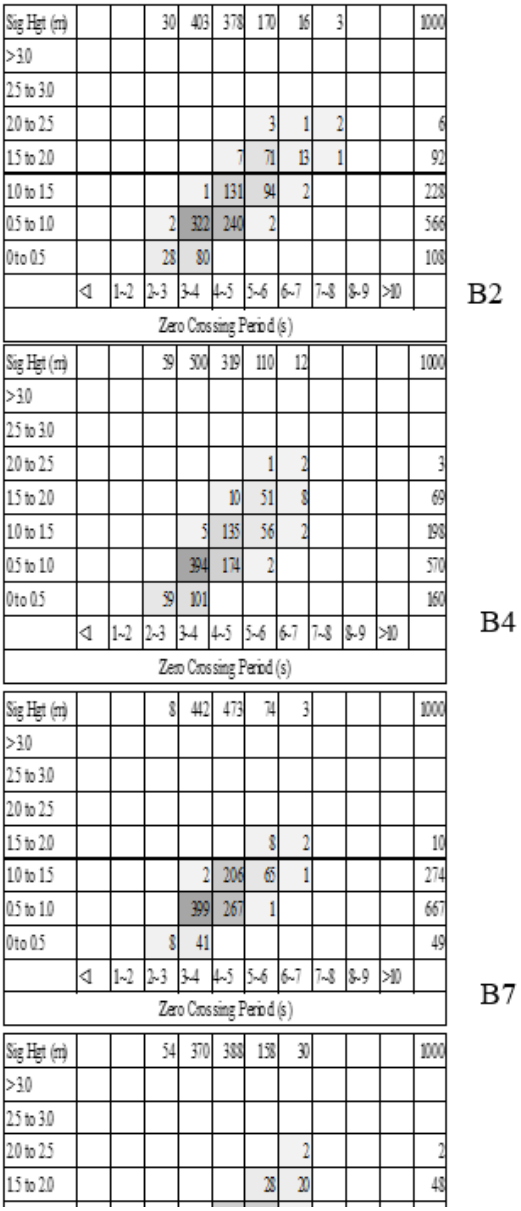

Figure 8. The wave scatter table of 16-bin for 18-year data

Based on Figure 8, zone B1 to B6 show the sea state is dominated by a significant wave height of 0.1 m to 0.5 m with

the peak period of 3s to 6s. As for B15 experienced a more dominant significant wave height range from 1.5-2.0m with 6s to 8s of wave period. In contrast, B7 has the highest occurrence of significant wave height between 0.5-1.0m. These results areclosely similar to the study by Yaakob et al. (2016). Sabah and Sarawak coastal area are dominated by significant wave height of 0.1 m to 0.5 m and peak period 3 s to 6 s. As mentioned before, scatter table is important to give information on the wavecondition.

IV. CONCLUSION

In conclusion, this study has proved the reliability of satellite altimeter data in providing accurate marine information for ocean renewable energy assessment in Malaysia. The validation result shows altimeter derived wind speed and significant wave height were well-correlated with the buoy measurement. However, this study suggests utilizing more in-situ measurements in order to improve the accuracy. During the northeast monsoon, Malaysia coastal region experienced strong wind and waves, especially areas that were facing towards the South China Sea. With the help of wind rose and wave scatter diagram, the study of wind and wave become much deeper. Based on this theoretical analysis, three locations were considered as potential areas for offshore wind energy, which are Terengganu coast, Pahang coast and north-coast of Sabah. For ocean wave energy, Terengganu coast and Sarawak coast possessed great potential.

ACKNOWLEDGEMENTS

The authors would like to thank to TU Delft Altimetrics LLC for providing altimetry data through Radar Altimeter Database System (RADS) and the oil and gas company for providing the buoy data. This project is funded by the Ministry of Science, Technology and Innovation (MOSTI) under the International Collaboration Fund, Project Number IF1117N0008 (UTM Vot Number: R.J130000.7901.4S142) and the Ministry of Higher Education (MOHE) under the Fundamental Research Grant Scheme (FRGS) Fund, Reference Code: FRGS/1/2020/WAB05/UTM/02/1 (UTM Vot Number: R.J130000.7852.5F374).

REFERENCES

Ardhuin, F. and Orfila, A., 2018. Wind waves. *New frontiers in Operational Oceanography*, pp. 393-422.

Hashim, F. E., Peyre, O., Lapok, S. R., Yakob, O., Din, A. H. M., 2020. Offshore Wind Energy Resource Assessment in Malaysia with Satellite Altimetry. *Journal of Sustainability Science and Management*, 15(6), pp. 111-124.

Hashim, F. E., 2016. Assessment of wave energy resources in Malaysia using satellite altimetry. Universiti Teknologi Malaysia.

Jadidoleslam, N., & Ozger, M., 2016. Wave power potential assessment of Aegean Sea with an integrated 15-year data. *Renewable Energy*, 86, pp. 1045–1059, doi: 10.1016/j.renene.2015.09.022.

Kumar, U. M., Swain D., Sasamal S.K., Reddy N. N., Ramanjappa, T., 2015. Validation of SARAL/Altika significant wave height and wind speed observations over North Indian Ocean. *Journal of Atmospheric and Solar-Terrestrial Physics*,135, pp. 174-180.

Nasab, N. M., Kilby, J. and Bakhtiaryfard, L., 2020. The potential for Intergration of wind and tidal power in New Zealand. *Sustainability*, 12 (1807), doi:10.3390/su12051807.

Nasir, N. A. M. and Maulud, K. N. A., 2018. Wave potential in Malaysia territorial waters. In: *IOP Conf. Series: Earth and Environmental Science*, Vol. 37.

Pastor, J., & Liu, Y., 2015. Wave energy resource analysis for use in wave energy conversion. *Journal of Offshore Mechanics and Arctic Engineering*, 137(1), 011903 (1–9), doi:10.1115/1.4028880.

Salam, M. A., Yazdani, M. G., Rahman, Q. M., Nurul, Dk., Mei, S. F. and Hassan, S., 2018. Investigation of wind energy potential in Brunei Darusssalam. *Frontiers in Energy*, doi: 10.1007/s11708-018-0528-4.

Shanas, P. R., Kumar, V. S., Hithin, N. K., 2014. Comparison of gridded multi-mission and along-track mono-mission satellite altimetry wave height with in situ near-shore buoy data. *Ocean Engineering*, 83, pp. 24-35.

Shamsuddin, A. H., 2012. Development of Renewable Energy in Malaysia-Strategic Initiatives for Carbon Reduction in the Power Generation Sector. *Procedia Engineering*, 49, pp.384-391.

Uti, M N, Din A H M, Omar A. H., 2017. Reliability of wind speed data from satellite altimeter to support wind turbine energy. In*: International Archives of the Photogram, Rem Sens & Spatial Sci*, 42(4W/5), pp. 215-224.

Uti, M. N., Din, A. H. M., & Yaakob, O., 2018. Significant wave height assessment using multi mission satellite altimeter over Malaysian seas. In: *IOP Conference Series: Earth and Environmental Science*, Vol. 169 (2018) 012025, doi :10.1088/1755-1315/169/1/012025.

Wan, W. A., Omar, K. M., & Din, A. H, 2014. Ocean Wind Speed Characteristic Over Malaysian Seas from Multi-Mission Satellite Altimeter during Monsoon Periods. *Jurnal Teknologi (Sciences & Engineering)*, 71(4), pp. 79-82.

Yaakob, O., Hashim, F. E., Omar, K. M., Din, A. H. M., & Koh, K. K., 2016. Satellite-based wave data and wave energy resource assessment for South China Sea. **Renewable Energy**, 88, pp. 359-371.

Yang, J. and Zhang, J., 2019. Validation of Sentinel-3A/3B satellite altimetry wave heights with buoy and Jason-3. *Sensors*, 19, 2914, doi:10.3390/s19132914.

Zaman, A. A. A., Hashim, F. E. and Yaakob, O., 2019. Satellite-based offshore wind energy resource mapping in Malaysia. *Journal of Marine Science and Application*, 18, pp. 114-121, https://link.springer.com/article/10.1007/s11804-019-00066-w.

REMOTE SENSING INTEGRATED WITH AIRBORNE MAGNETIC DATA TO MAP SUBSURFACE STRUCTURES USING IMAGE CLASSIFICATIONS

[1]Kayode, J.S. [1]Nawawi, M.N.M., [1,2]Khalil A. E., and [3]Arifin, M.H.

[1]Geophysics Unit, School of Physics, Universiti Sains Malaysia, 11800 USM, Penang. Malaysia.

[2]Geology Department, Faculty of Science, Helwan University, Cairo, Egypt.

[3]Program Geologi, Jabatan Sains Bumi dan Alam Sekitar, Fakulti Sains dan Teknologi, Universiti Kebangsaan Malaysia. 43600 UKM, Bangi, Selangor, Malaysia.

*Corresponding Author: jskayode@gmail.com

KEY WORDS: Remote sensing, Image classifications, Aeromagnetic data, Subsurface minerals occurrences.

ABSTRACT:

Application of the remote sensing technique (RST) offers synoptic scrutiny of the subsurface geological structures (SGS), along with its use for detailed monitoring and transformations of the exposure analysis of natural and environmental resources. Prior to the data analysis, initial processing of the raw data was carried out to correct for any misrepresentation of images due to the characteristics of the imaging system and the environments. A geometric correction pre-processing technique was applied to the digital images due to the enclosure of geometric distortions that prevent the use of the geology map directly. The georeferenced projection was accomplished using the Universal Transverse Mercator, (UTM), Zone 32^{a} N E012, Datum World Geodetic System, 1984, (WGS 1984). The output pixel spacing was correctly set as it determined the size of the corrected image on the geology map. Ground Control Points (GCP) were manually selected on the geology map, with the image from Google Earth as the reference image for the selecting points. Pixels were assigned to the various classes of the geologic features of their spectral properties. A supervised classification method (SCM) was applied to classify the rock bodies. At the training stage, all classes were assigned based on the rock types in the study area. The principal objective is to define geological boundaries, rock contacts, lineaments, faults, fractures and other features that support the occurrence of subsurface minerals in the study area through the integration of aeromagnetic data and remote sensing datasets.

I.INTRODUCTION

The search for natural subsurface resources to enhanced sustainable economic development has been made possible by the integration of remote sensing technique (RST) with the airborne magnetic datasets to map underlain subsurface structures by means of image classifications. Correct subsurface characterization is essential for mineral resources mapping and development. The research aimed at accurate processing of the images, the georeferenced raw datasets, using the coordinates of the topographic sheets of the study area, by integration of the remote sensing technique (RST), the geology map and the aeromagnetic data using the PCI Geomatica© software (Kayode, 2017; Kayode et al., 2017; Fahil, et al., 2020, Jackisch, et al., 2020). The main objective of the study is to develop a non-complicated approach to evaluating subsurface structural futures for the occurrences of both magnetic (i.e. areas with high magnetic intensity values) and non-magnetic (i.e. places with low magnetic intensity values) in a complex geological basement environment.

To derive this precious information from the study incorporated remote sensing by means of the output pixel spacing that was accurately located to determine the size of the spot on the image from the geology map. The aeromagnetic data was applied to delineate and classify the extension of subsurface lithological geological features through closed observations. The different datasets are integrated by the supervised image classifications to be able to separate spectrally and non-distinct rock types underlain the study area. As a consequence, the technique makes it possible to connect surface geological information that serves as indicators for the subsurface mineral occurrences in relation to surface pixel classifications and magnetic minerals within the subsurface geological structural features (SGSFs) (Fahil, et al., 2020; Jackisch, et al., 2020; Kayode et al., 2020, Kayode and Yusup, 2020). Using the trends and spatial distribution of the high-resolution airborne magnetic datasets intended for solid mineral exploration, the valuable information derived is tailored towards the planning and development of the mineral resources in the study area.

II.METHODOLOGY

A. The Data

The study used the high-resolution airborne magnetic datasets intended for solid mineral exploration obtained across the Nigerian Basement Terrain by Canadian firms (namely Fugro Airborne Survey Services, and Patterson Grant and Watson), through the Nigerian Geological Survey Agency (NGSA). These firms had obtained the airborne data between the years 2003 and 2009, along the NW–SE flight lines that were positioned at right angles to the most significant narrow geological strike. To record this data, an airplane was flown at typically spaced 0.5 km intervals, with a ~2000 m tie-line spacing along the northeast-southwest (NE-SW), directions at ~80 m nominal flight elevation; the data was recorded at 0.1 s intervals for the magnetometer settings (Kayode, 2017).

Combining the nominal flight height—that was set exceptionally close to the ground surface using narrow line spacing—and the extremely small recording time gaps, this study achieved a higher resolution of the magnetic anomalies than the general high-altitude airborne magnetic surveys. Prior to the data distribution by the NGSA to the interested users, the Fugro Airborne Surveys Company processed the essential magnetic data corrections: the geomagnetic gradient was alienated from the data using the existing model with the International Geomagnetic Reference Field (IGRF), January 2005 version, as specified in the World Geodetic System 1984 ellipsoid (Kayode, et al., 2017; Kayode, 2017; Kayode and Yusup, 2018). Besides, the Universal Transverse Mercator (UTM) coordinate system was used to project the airborne magnetic data. The airborne magnetic survey data presented in this study covered the Omu-Aran area in parts of the Nigerian south-western Precambrian basement complex (NSPBC), with moderately shallow overburden lithologies (Kayode, 2017). The geology map was obtained from the Nigerian Geological Survey Agency (NGSA). The Landsat^{TM} 8 and the digital elevation model (DEM) data were freely downloaded from the United States Geological Survey (USGS) website.

B. Ground Control Points, (GCP)

To ensure the accuracy of maps coordinates that could be read as maps in the PCI Geomatica© software in addition to overlay with each other whilst processing the images, the raw data were georeferenced using the coordinates of the topographic sheets of the study area. The georeferenced projection was accomplished using the Universal Transverse Mercator, (UTM), Zone 32$^{\alpha}$ N E012, Datum World Geodetic System 1984, (WGS 1984), (Kayode, 2017, Kayode et al., 2017).

The output pixel spacing was correctly set as it determined the size of the corrected image on the geology map. Ground Control Points, (GCP) were manually selected on the geology map with the image from Google Earth as the reference image for the selecting points. After selection of all the GCP, the geometric correction was carried out to ensure all the maps produced were in the same projection (i.e., UTM, Zone 32$^{\alpha}$ N E012, WGS 1984) before it could be used for the study (Kayode 2017, Kayode et al., 2017).

The projection of the output and GCP images was fixed to UTM 32$^{\alpha}$ N E012, WGS 1984 with a pixel size of 100 m before the GCPs are collected. The GCPs were manually selected by picking a point in the image and inserting the latitude and longitude coordinates values with respect to the geological map (Figure 1). The quality of the geometrically corrected image produced is a function of the root mean square errors (RMS), values obtained which are directly related to the quality and the number of the GCPs and the chosen math model. If a wrong math model is selected, or too few GCPs are collected, and inaccuracy in the process of collecting the GCPs, all these may lead to a geometrically incorrect image produced that may perhaps not suit the need and purpose of the research work. The RMS values obtained are; (i) 6.79 residual, (ii) 6.04 along the X - direction, and (iii) 3.12 along Y-direction suitable and acceptable enough for the accuracy of the processes (Kayode et al., 2017).

C. Auto selection of pixels in PCI Geomatica© software.

Sampling interval control how the computations were performed when an image is geometrically corrected. OrthoEngine in the PCI Geomatica© software automatically selects a pixel from the output file, computes the elevation from the digital elevation model (DEM) data, and applies the math model to determine which pixel corresponds to a pixel in the raw image, and then transfers the data to the pixel that matches in the output file. The sampling interval determines how many output pixels are to be computed during the process. For this research work, a sampling interval of one was adopted to ensure that every output pixel was processed. However, processing of every output pixel can take lots of time in remote sensing technique (RST).

D. Colour Composite Enhancement Technique Using the Maximum Likelihood.

Colour composite enhancement technique (CCET), was performed on the Landsat^{TM} 8 images generated from the remote sensing data, as shown in Figure 2. Although the data available for this area was cloudy at the time the data was acquired by the USGS, it was still possible to assigned pixels to the various classes of the geologic features and their spectral properties. A supervised classification method (SCM) was applied to classify the rock bodies. At the training stage, all classes are assigned based on the rock types in the study area. Different colours for each class were selected to distinguished, without difficulties, the types of each rock unit.

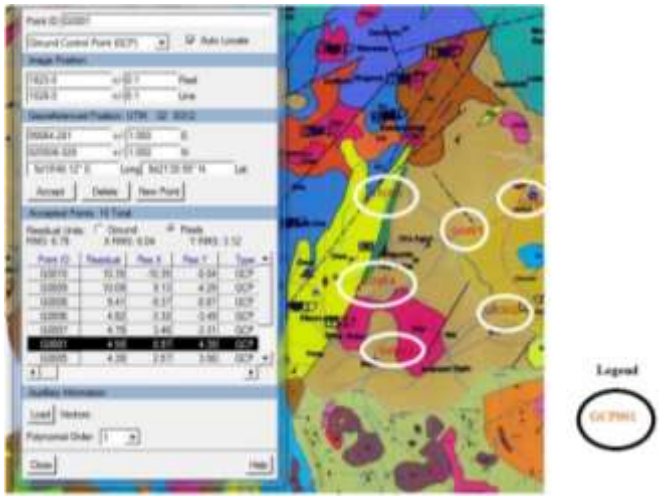

Figure 1. Landsat^{TM} 8 and geological map Ground Control Point image processing, adapted from Kayode (2017).

The classifier generated a new image according to its spectral properties at the end of the training stage. Naturally, there are three types of classifiers to generate image classifications, that is; (a) the maximum likelihood, (b) the minimum distance, and (c) the parallelepiped. The maximum likelihood classifier is most frequently applied in image classifications (Huguenin et al., 1997, Westbrook et al., 2012). The best classification is the image that correlates with another image in the geology map and gives the highest value in the accuracy assessment report. Land cover classification at the sub-pixel size provides further bias than the usual per-pixel multispectral classifiers for pixels, where the features of interest varied with other structures. The process permits the un-mixing of pixels to show the fraction of each feature of interest (Westbrook et al., 2012). Our interest in this study area is to delineate geological boundaries, rock contacts, linear features, faults, fractures, and other SGFs that support solid minerals occurrences, (Kayode, 2017).

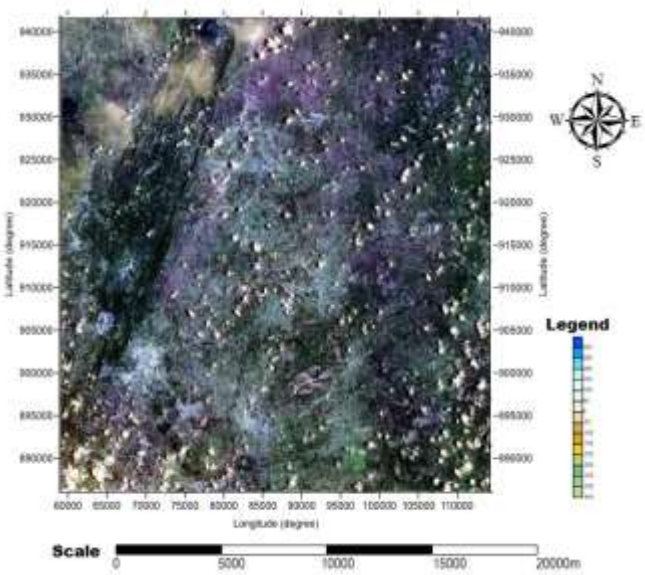

Figure 2. Landsat^{TM} 8 image of the study area, adapted from Kayode, (2017).

III.RESULTS AND DISCUSSION

A. Integration of Total Magnetic Intensity data and Landsat^{TM} 8.

The Landsat^{TM} 8 map produced through integration of the Total Magnetic Intensity, (TMI), data of the study area together, using PCI Geomatica© software as shown in Figure 3. The map clearly defined the principal structural features (PSF), trending, in the NNE-SSW followed by the NE-SW trends as the dominant subsurface geologic structural features emplace in the study area (i.e., the redline arrows). Other trends are in the NE, SE, NW, and SW respectively. These SGFs are the most important features controlling and also responsible for the solid mineral's occurrences in the study area (Kayode 2017, Kayode et al., 2017, Kayode and Yusup, 2018).

B. Nearest Neighbours (NN) Process using the Digital Elevation Model (DEM), image.

The DEM image (i.e., Figure 4) was used to estimates the SGFs of interest that were mapped, based on the declining path of each cell, using the nearest neighbours, (NN) processes. The changes in the topography connected with the subsurface and the surface structural linear features, geological features and those of man-made features were as highlighted in Figure 4, the same as the new map generated by the classifier in line with their spectral properties when the training stage finished.

The most excellent classification (MEC) is the image that showed the most affiliation with the corresponding image on the geology map and offered the highest value in the accuracy assessment details. In situations where the concerned SGFs of interest mixed up with other features present, land-cover classification at the sub-pixel size affords auxiliary bias than the usual per-pixel multispectral classifiers for the pixels, which makes their separation effortlessly achievable. The maximum likelihood classifier most commonly used in image classifications was adopted and applied in this work to generate Figure 4.

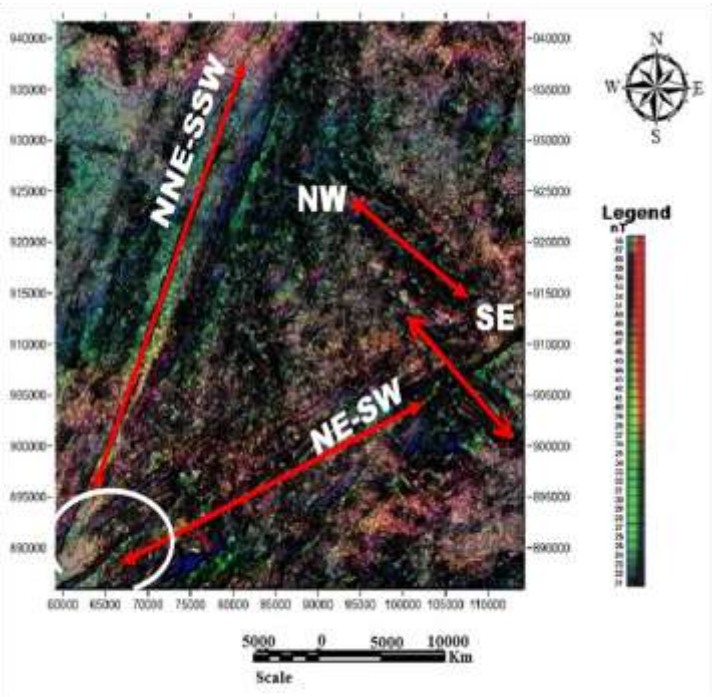

Figure 3. Landsat ^{TM} 8 map integrated into the Total Magnetic Intensity data of the study area from the PCI Geomatica software. Modified after Kayode, (2017).

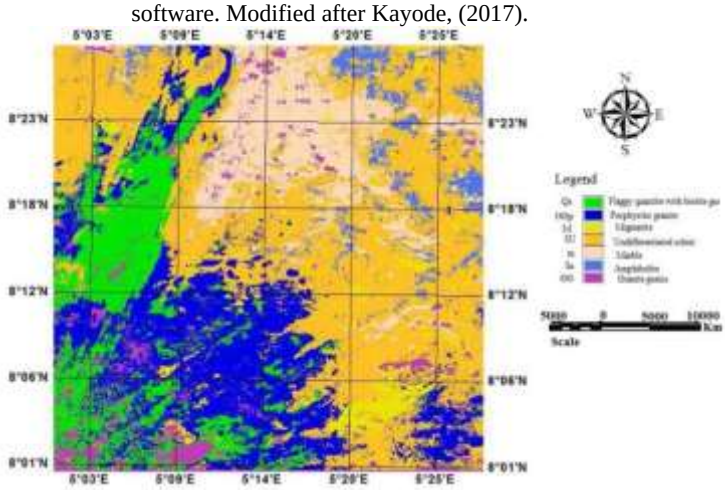

Figure 4. Maximum Likelihood geological structures and rocks classification map of the Total Magnetic Intensity integrated into the DEM data of the study area.

IV.CONCLUSION

The integration of aeromagnetic and remote sensing data implemented in this research work assisted in the determination of the subsurface linear features, (SLF), in the study area as shown in all the maps generated. The subsurface structural patterns, (SSP) obtained from the maps provide an excellent correlation with the techniques adopted. These SGFs are responsible for the control of the mineralized features in the study area as clearly defined by the geologic structural features in the study area. An offset observed by the white circular ring at the lower end of the map shown in Figure 3 may perhaps be a geological event due to tectonic activities. Closed observation

of these SGFs showed some major partitioning and diverse orientations of each block delineated.

The Applied RST proffered a synoptic analysis of the subsurface geological structures along with its use for detailed monitoring and transformations of the exposure mineral resources of the study area. The technique makes understanding of the terrains subsurface signatures underlain the area possible when data are integrated together. The study was able to expose the mechanisms that contributed and controlled the minerals productiveness of the schist belt zone. On a final note, the SGFs as shown, are the most significant features responsible for the minerals occurrences in the area.

ACKNOWLEDGMENTS

We thank Universiti Sains Malaysia, Pulau Pinang, Malaysia, for supporting our research through the Institute of Postgraduate Studies (IPS), Postgraduate Fellowship Awards. We appreciate the United States Geological Survey, (USGS) for the free access to Landsat™ 8 and DEM datasets. We also wish to acknowledge the efforts of our reviewers, who have helped to improve the standard of this paper.

COMPETING INTERESTS

The authors declare that they have no known competing financial interests or personal relationships which have, or could be perceived to have, influenced the work reported in this article.

REFERENCES

Fahil, A.S., Ghoneim, E., Noweir, M.A. and Masoud, A., 2020. Integration of Well Logging and Remote Sensing Data for Detecting Potential Geothermal Sites along the Gulf of Suez, Egypt. *Resources*, *9*(9), p.109. https://doi.org/10.3390/resources9090109

Jackisch, R., Lorenz, S., Kirsch, M., Zimmermann, R., Tusa, L., Pirttijärvi, M., Saartenoja, A., Ugalde, H., Madriz, Y., Savolainen, M. and Gloaguen, R., 2020. Integrated Geological and Geophysical Mapping of a Carbonatite-Hosting Outcrop in Siilinjärvi, Finland, Using Unmanned Aerial Systems. *Remote Sensing*, *12*(18), p.2998. https://doi.org/10.3390/rs12182998

John Stephen Kayode and Yusri Yusup. 2020. A novel fusion Python application of data mining techniques to evaluate airborne magnetic datasets. Computer and Geosciences, CAGEO-D-20-00064-R1 Revision submitted back to the journal.

Kayode, J. S., Nawawi, M. N. M., Yusup Y., Khalil A. E., Arifin, M. H., Aduloju, M. O., and Mohamad Shafiq Suhaimi. 2020. GIS-based geospatial tools for estimating the magnetic anomaly depth of hydrothermal mineral deposits using inverse distance weights method. Journal of African Earth Sciences. Manuscript Number. AES-9209. Under Review.

Kayode, J.S., 2017. Integration of Qualitative and Quantitative Analysis for Mineral Resources Mapping in Omu-Aran Schist Belt Zone, Nigeria. Unpublished PhD Thesis, Universiti Sains Malaysia Institute of Postgraduate Studies, 230p

Kayode, J.S., Nawawi, M., Abdullah, K.B., Khalil, A.E., 2017. Integrating aeromagnetic and Landsat™ 8 data into the subsurface structural mapping of Precambrian basement complex, *Journal of Afican. Earth Sciences* vol. 125, pp. 202–213. http://dx.doi.org/10.1016/j.jafrearsci.2016.11.010.

Kayode, J.S., Yusup, Y., 2018. Data on the evaluation of structural index from aeromagnetic enhanced datasets with the application of Euldphλ semi-automatic algorithm *Data in Brief* vol. 19, pp. 798–803. https://doi.org/10.1016/j.dib.2018.05.090.

Huguenin, R. L., Karaska, M. A., Van Blaricom, D. & Jensen, J. R., 1997. Subpixel classification of bald cypress and tupelo gum trees in Thematic Mapper imagery. Photogrammetric *Engineering and Remote Sensing*, vol. 63, pp. 717-724.

Westbrook, J., Hung, I., Unger, D., Zhang, Y., 2012. Sub-Pixel Classification of Forest Cover Types in East Texas.

SATELLITE REMOTE SENSING OF PHYTOPLANKTON COMMUNITY STRUCTURE AND ITS PHENOLOGY IN THE ARABIAN SEA

Rebekah Shunmugapandi[1], Shirish kumar Gedam[1], Arun B. Inamdar[1]

[1]Center of Studies in Resources Engineering, Indian Institute of Technology Bombay
India – (rebekah.s,shirish,abi)@iitb.ac.in

KEY WORDS: Ecological indicator; Interannual variability; Indian monsoon; Phytoplankton phenology; and Remote sensing

ABSTRACT:

Phytoplankton is a sensitive indicator to monitor the state of the marine ecosystem efficiently and detect changes stimulated by environmental conditions. Earlier studies on phytoplankton phenology over the Arabian Sea remain unclear, often due to data usage with missing values due to overcast and sensor errors. Here we investigated the phenology of phytoplankton over the Arabian Sea using reconstructed chlorophyll-*a* data (chl-*a*). The missing data values were reconstructed using the DINEOF approach for 2003 and 2018 through threshold criterion phenological indices. The long-term phytoplankton study allows a unique understanding of the patterns of phytoplankton dynamics. From the results, it is found that the Indian monsoon dynamics is the main influencing factor that could both hinder and facilitate the distribution of phytoplankton over the Arabian Sea. The present work revealed the efficiency of the DINEOF method in reconstructing the missing chl-*a* data. Further, this study highlighted the unique adaptations of phytoplankton and their sensitiveness towards the monsoonal pattern.

I. INTRODUCTION

Phytoplankton, the microscopic cells living in the ocean's euphotic layer, plays a predominant role in the marine food web and biogeochemical cycle (Andreo, Dogliotti, and Tauro 2016; Falkowski 2012). The existence of phytoplankton is not uniform as they are sensitive to environmental factors (Ardyna et al., 2017). The distribution of phytoplankton is under the control of physical forcing subjected to regional and seasonal changes (Barlow, Mantoura, and Cummings 1999). Being in a tropical region, the Arabian Sea experiences a unique reversal monsoonal wind pattern that facilitates bloom in the summer (June to August) and winter monsoon (December-March) (Kumar et al. 2004; Prasanna Kumar et al. 2010). Episodic occurrence of seasonal changes triggers phytoplankton production, especially in the upwelling region due to the enrichment of deep-seated nutrients (Koné et al. 2009). The distribution of phytoplankton can be obtained mainly through field-based observation, remote sensing and model simulation. Field-based observation is carried out traditionally by ship-board survey and recently by Argo floats. Due to cost and unstable weather conditions, phytoplankton's continuous monitoring is always sparse in the Arabian Sea. Even though climate reanalysis datasets provide constant observation, still the resolution is very coarse and not suitable for regional based study. From remote sensing-based observation, high spatial and long-time-scale continuous datasets can be obtained (IOCCG 2014).

The seasonality of phytoplankton bloom using satellite-based observation though a well-researched topic and understood phenomena (Kumar et al. 2004; Narvekar and Prasanna Kumar 2006; Prasanna Kumar et al. 2010). However, the satellite-based datasets used for such analysis were uncertain due to missing data issues due to cloud conditions and sensor errors. Investigation of phytoplankton phenology using such datasets will not provide clear information (Jayaram, Kochuparambil, and Balchand 2013; Rebekah, Inamdar, and Gedam 2019). Since the Arabian Sea are prone to heavy data loss during the extreme condition (Hilborn and Costa 2018). Therefore, the rectification of satellite observation is mandatory for better understanding.

Missed values in the geophysical datasets can be rectified using Data INterpolation Empirical Orthogonal Function (DINEOF). The DINEOF method is an empirical orthogonal function developed by Beckers et al. (2003) to fill the gaps in geophysical datasets. Compared to other geophysical data reconstruction methods, the DINEOF method is computationally efficient and requires significantly fewer input requirements.

In the present work, we reconstructed the sixteen years of MODIS-Aqua chlorophyll-*a* (chl-*a*) datasets (2003-2018) using the DINEOF method. With the reconstructed chl-*a* datasets, the phenological phytoplankton patterns have been assessed using a statistical approach.

II. DATA AND METHODS

A. Study site and satellite Data

We conduct our study of phytoplankton patterns in the Arabian Sea extended within 6^0N-31^{o}N and 43^{o}E – 79^{o}E located in the Northern part of the Indian Ocean. To investigate the distribution structure of chl-*a* in the Arabian Sea, we used sixteen-year daily MODIS-Aqua Level 3 chl-a data (2003-2018) to be downloaded from the NASA ocean color website. We chose MODIS-Aqua chl-*a* of 4 x 4 km spatial resolution as appropriate for long-timescale chl-*a* assessment.

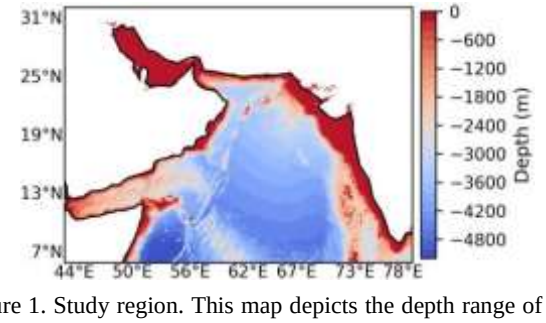

Figure 1. Study region. This map depicts the depth range of the Arabian Sea.

B. Data Reconstruction

DINEOF approach is a self-consistent method for reconstructing missing data values in the geophysical datasets (Alvera-Azcárate et al., 2016; Beckers and Rixen, 2003). The singular vector decomposition process is carried out on iteration basics with repetitive EOF modes until RMS's optimal convergence (Alvera-Azcárate et al., 2016; Hilborn and Costa 2018). After that, the second EOF mode runs under the same process; this procedure continues with the maximum number of EOF until the optimal RMS convergences occur (Beckers and Rixen 2003; Taylor et al. 2013; Zhou, Peng, and Shi 2017). The resultant reconstructed data will be with no gaps, thus ready for further analysis.

C. Statistical analysis

Using the gap-filled chl-*a* time series data, we calculated the chl-*a* anomalies and phenological indexes. The chl-*a* anomalies were estimated with positive and negative anomalies over the Arabian Sea. Further, the phenological indexes: month of maximum and minimum chl-*a* were obtained pixelwise for the whole time series over the Arabian Sea.

III. RESULTS

A. Chl-*a* anomalies

Both the annual anomalies and monthly climatology showed distinctive variation in the chl-*a* distribution of the Arabian Sea. Figure 2 shows the yearly anomalies of chl-*a*. The chl-*a* annual anomalies did not show any clear pattern in the distribution. For instance, in the years 2006,2008 and 2009, the positive anomalies are found in the northern part of the Arabian Sea, while in 2007, 2011,2012,2018, the chl-*a* distribution is lower (i.e. negative anomaly). Significantly, the year 2008 showed a higher distribution compared to other years. On the other hand, from 2010 to 2011, chl-*a* showed lower values in the north part of the Arabian Sea. The southern part of the Arabian Sea is found to be consistent in nature.

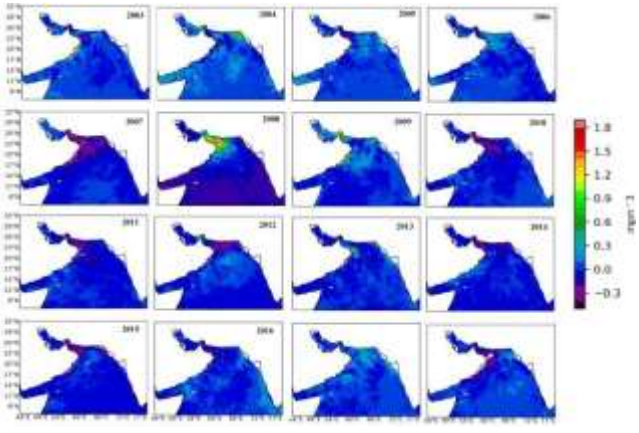

Figure 2. Annual Anomalies of time-series chl-*a* in mg/m^3 calculated from the reconstructed data.

B. Statistical Indexes

The estimation of the distribution of chl-*a* time series maximum and minimum is shown in Figure 3 and 4. The maximum rate of chl-*a* distribution was from December to March in the northern part of the Arabian Sea. Most of the region began to bloom between early December to March and June to August, which positively correlates with the winter monsoon and summer monsoon. During the inter-monsoon period (April-May), the chl-*a* distribution is found to be significantly less.

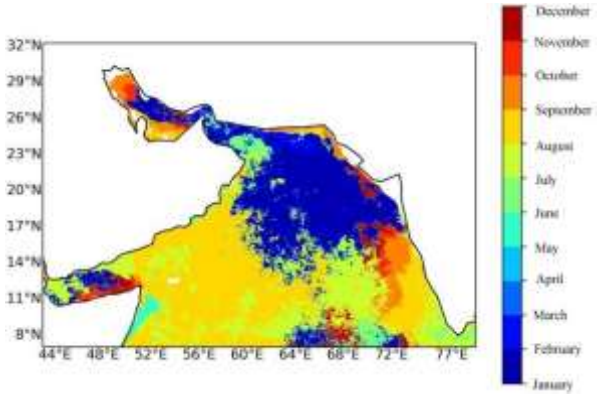

Figure 3. The month of maximum chl-*a* (mg/m^3) from the reconstructed data over the period 2003-2018.

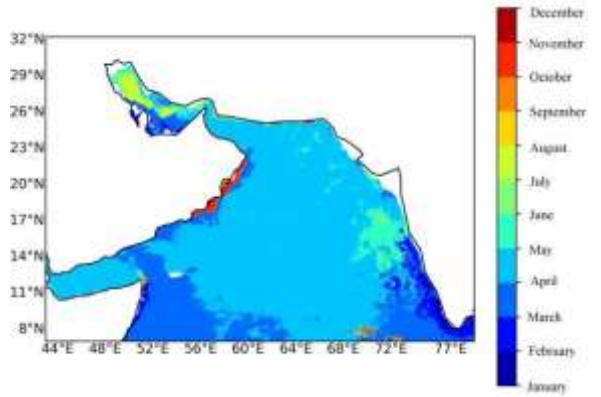

Figure 4. The month of minimum chl-*a* (mg/m^3) from the reconstructed data over the period 2003-2018.

IV. CONCLUSION

We obtained an overview of chl-a distribution pattern in the Arabian Sea using reconstructed satellite data from this study. Further, the present work demonstrated the effectiveness of chl-a data reconstruction with no missing data. The results show the Indian Monsoonal pattern influence on the phytoplankton distribution in the Arabian Sea. This study complements the gap-filling techniques to understand better the distributional pattern of chl-a in the Arabian Sea.

Overall, this study has an essential contribution to marine ecosystem monitoring and conservation. Further research in this area has a scope for harmful algal bloom prediction, marine ecosystem observation and the impact of climatic changes.

ACKNOWLEDGEMENTS

The authors would like to thank NASA for the open-source chlorophyll-*a* concentration and GHER for the DINEOF platform. The authors would also like to thank the Department of Science and Technology for supporting this research through the DST-INSPIRE programme.

REFERENCES

IOICCG. 2014. "Phytoplankton Functional Types from Space." *Reports and Monographs of the International OceanColour Coordinating Group* (15):156.

Falkowski, Paul. 2012. "Ocean Science: The Power of Plankton." *Nature* 483(7387):S17–20. doi: 10.1038/483S17a.

Alvera-Azcárate, Aida, Alexander Barth, Gaëlle Parard, and Jean Marie Beckers. 2016. "Analysis of SMOS Sea Surface Salinity Data Using DINEOF." *Remote Sensing of Environment* 180:137–45. doi: 10.1016/j.rse.2016.02.044.

Andreo, Verónica Carolina, Ana I. Dogliotti, and Carolina Beatriz Tauro. 2016. "Remote Sensing of Phytoplankton Blooms in the Continental Shelf and Shelf-Break of Argentina: Spatio-Temporal Changes and Phenology." *IEEE Journal of Selected Topics in Applied Earth Observations and Remote Sensing* 9(12):5315–24. doi: 10.1109/JSTARS.2016.2585142.

Beckers, J. M., and M. Rixen. 2003. "EOF Calculations and Data Filling from Incomplete Oceanographic Datasets." *Journal of Atmospheric and Oceanic Technology* 20(12):1839–56. doi: 10.1175/1520-0426(2003)020<1839:ECADFF>2.0.CO;2.

Barlow, R. G., R. F. C. Mantoura, and D. G. Cummings. 1999. "Monsoonal Influence on the Distribution of Phytoplankton Pigments in the Arabian Sea." *Deep-Sea Research Part II: Topical Studies in Oceanography* 46(3–4):677–99. doi: 10.1016/S0967-0645(98)00123-4.

Jayaram, Chiranjivi, Ajith Joseph Kochuparambil, and Alungal N. Balchand. 2013. "Interannual Variability of Chlorophyll-a Concentration along the Southwest Coast of India." *International Journal of Remote Sensing* 34(11):3820–31. doi: 10.1080/01431161.2012.762482.

Koné, Vamara, Olivier Aumont, Marina Lévy, and L. Resplandy. 2009. "Physical and Biogeochemical Controls of the Phytoplankton Seasonal Cycle in the Indian Ocean: A Modeling Study." *Ocean Biogeochemical* 147– 66. doi: 10.1029/2008GM000700.

Prasanna Kumar, S., Raj P. Roshin, Jayu Narvekar, P. K. Dinesh Kumar, and E. Vivekanandan. 2010. "What Drives the Increased Phytoplankton Biomass in the Arabian Sea?" *Current Science* 99(1):101–6.

Prasanna Kumar, S., M. Nuncio, Jayu Narvekar, N. Ramaiah, S. Sardesai, M. Gauns, V. Fernandes, J. T. Paul, R. Jyothibabu, and K. A. Jayaraj. 2010. "Seasonal Cycle of Physical Forcing and Biological Response in the Bay of Bengal." *Indian Journal of Marine Sciences* 39(3):388– 405.

Rebekah, S., A. B. Inamdar, and Shirish S. Gedam. 2019. "LONG-TIME-SCALE INVESTIGATION OF PHYTOPLANKTON BIOMASS THROUGH RECONSTRUCTED CHLOROPHYLL-A DATA USING DINEOF METHOD Indian Institute of Technology Bombay , Mumbai , Maharashtra , India – 400076." *IGARSS 2019 - 2019 IEEE International Geoscience and Remote Sensing Symposium* 7995–98.

Sarangi, R. K., Prakash Chauhan, and Shailesh R. Nayak. 2005. "Inter-Annual Variability of Phytoplankton Blooms in the Northern Arabian Sea during Winter Monsoon Period (February-March) Using IRS-P4 OCM Data." *Indian Journal of Marine Sciences* 34(2):163–73.

Hilborn, Andrea, and Maycira Costa. 2018. "Applications of DINEOF to Satellite-Derived Chlorophyll-a from a Productive Coastal Region." *Remote Sensing* 10(9):11– 13. doi: 10.3390/rs10091449.

Taylor, Marc H., Martin Losch, Manfred Wenzel, and Jens Schröter. 2013. "On the Sensitivity of Field Reconstruction and Prediction Using Empirical Orthogonal Functions Derived from Gappy Data." *Journal of Climate* 26(22):9194–9205. doi: 10.1175/JCLI-D-13-00089.1.

Zhou, Wang, Bin Peng, and Jiancheng Shi. 2017. "Reconstructing Spatial–Temporal Continuous MODIS Land Surface Temperature Using the DINEOF Method." Journal of Applied Remote Sensing 11(04):1. doi: 10.1117/1.JRS.11.046016.

DYNAMICALLY LINKED EXTREME WEATHER EVENTS OVER THE NORTHWESTERN PACIFIC OCEAN IN JANUARY 2018

M. Pichugin[1], I. Gurvich[1]

[1]Department of Satellite Oceanography and Laser Sensing, V.I.Il'ichev Pacific Oceanological Institute, Far Eastern Branch, Russian Academy of Sciences, 43, Baltiyskaya Street, Vladivostok, 690041, Russia
(pichugin, gurvich)@poi.dvo.ru

KEY WORDS: Cold Air Outbreak, Extratropical Cyclones, Extreme Weather, Northwestern Pacific Ocean, Polar Low, Satellite Remote Sensing

ABSTRACT:

An accurate severe marine weather systems forecast and hindcast are very important for marine traffic and offshore management. The capability of multisensor satellite optical and microwave observations opens new opportunities to improve numerical weather prediction (NWP) models, which still have some deficits under extreme weather conditions. This study combines satellite active and passive microwave measurements and model data to examine the multiscale extreme weather events (EWEs) over the northwestern Pacific Ocean during late January 2018. The EWEs include anomalous cold conditions in Primorsky Krai (Russia) linked to prolonged (7 days) marine cold-air outbreak (CAO) over the Sea of Japan, the occurrence of the two extratropical cyclones explosively developing over the Kuroshio–Oyashio Extension region and intense polar low (PL) over the northern part of the sea. The abnormally long CAO was caused by atmospheric blocking due to the location of the tropospheric ridge over the Bering Sea. Cold advection along the western periphery of the upper-level low over the Northeast Asia and the Sea of Japan consistently contributed to both explosive cyclogenesis east of the Honshu and rapid evolution of PL with near hurricane winds over the coastal area of Primorsky Krai. On January 23, the sea level pressure in the centre of the most intense extratropical cyclone dropped sharply from 1004 to 958 hPa per day; satellite-based winds reached 40-42 m/s. Model data significantly underestimated the development of synoptic- and mesoscale pressure systems in the fields of sea level pressure and sea surface wind speed. Satellite multisensor analysis allowed us to consider the evolution of the PL in the fields of cloudiness, wind speed, and the moisture content in the atmosphere; reveal storm-force wind jets off the continental coast of the Sea of Japan during CAO event, which also represent a hazard to marine traffic.

I.INTRODUCTION

Intensive marine weather systems (MWS), accompanied by storm/hurricane force winds, extreme heat and moisture fluxes at the sea surface and heavy precipitation, partly characterize the state of the Earth's climate system. Since the beginning of the 21st century, changes in a number of the ocean-atmosphere system parameters have clearly manifested, affecting the intensity of the mid-latitude extreme weather in the northern hemisphere. Recent studies demonstrate a decrease in the Arctic ice cover, the variability of typical trajectories of extratropical winter cyclones, the increase in cases of extreme values of air temperature and precipitations.

In the winter months, along with the North Atlantic and the Arctic basin, the marginal seas of the northwestern Pacific Ocean are areas of frequent cold air outbreaks, characterized by rapid advection of the polar continental air mass to low latitudes and extreme weather. Climatically significant polar lows are also associated with such outbreaks (Rasmussen and Turner, 2003). Their rapid deepening often leads to an abrupt increase in the sea surface wind speed, in some cases up to 32 m/s and more (Fore et al., 2012).

This study examines the conditions of occurrence and development of the multiscale extreme weather events (EWEs) over the northwestern Pacific Ocean during January 22–27, 2018. We combine satellite active and passive microwave measurements and reanalysis data sets with taking a closer look at the EWEs.

II.DATA AND METHODS

A. Reanalysis data sets

The analysis of the characteristics of extreme weather events is based on the hourly fields of the zonal and meridional components of the wind speed and pressure at the sea surface, taken from the operational analyses of Climate Forecast System, Version 2, (CFSv2) of National Centers for Environmental Prediction and ERA5 data set - the fifth generation the European Centre for Medium-Range Weather Forecasts atmospheric reanalysis. Both data sets have a comparable spatial resolution of 27-31 km and assimilate satellite estimations of sea surface vector winds. We assume that this data will allow us to examine the mesoscale atmospheric circulations and orographic effects.

B. Satellite multisensor measurements

The location and size of baric systems, the cloud structure and its evolution over the sea surface were determined by satellite visible and infrared images obtained from spectroradiometers MODIS onboard Aqua and Terra satellites and VIIRS onboard Suomi NPP satellite. A detailed analysis of the PL characteristics was carried out using a series of infrared images measured at a 30-minute interval from the Korean geostationary satellite COMS.

The measurements of Advanced Microwave Sounding Radiometer AMSR2 onboard GCOM-W1 satellite were used to obtain and analyze the fields of total atmospheric water vapour

content, cloud liquid water content and sea surface wind speed. These hydrometeorological parameters were retrieved from AMSR2 Level 1B swath brightness temperature data using advanced retrieval algorithms (Zabolotskikh et al, 2015). For more accurate wind speed estimates, in addition to the AMSR2 data were supplemented the measurements of scatterometer ASCAT onboard MetOp-A/B satellites.

III.EXTREME WEATHER EVENTS

Extreme weather events developed under atmospheric blocking due to location the tropospheric ridge over the Bering Sea and cold advection along the western periphery of the upper-level low over the Northeast Asia and the Sea of Japan.

A. Cold Air Outbreak

Analysis of visible and infrared images and satellite-derived geophysical parameters allow us to identify prolonged (6 days) Cold Air Outbreak (CAO) over the Sea of Japan from January 22 to 27, 2018. Satellite images showed the occurrence and evolution of convective clouds organized in two- dimensional structures (fig. 1a) known as "roll clouds" or "cloud streets" indicating shallow boundary layer convection (Etling and Brown, 1993). An abnormally prolonged CAO was associated with a near-stationary strong high-pressure ridge over the Bering Sea and characterized by strong (10 - 12 m/s), in some areas storm (25 - 27 m/s) winds and low total water vapour content off the continental coast.

At the mature stage of the outbreak, the ASCAT- and AMSR2-derived sea surface wind speed exceeded 15 m/s over most of the sea (fig. 1b, c). The maximum winds were observed in one of the bands off the west coast of the sea, extending from the northwest to the southeast. According to weather stations, gusts of wind on the eastern coast of Primorsky Krai reached 28–32 m/s. These wind bands were formed under the influence of orographic gaps near Vladivostok (Kawamura and Wu 1998). During the CAO the total water vapour content varied considerably: from 1-2 kg/m^2 off the continental coast to 7-8 kg/m^2 along the northwestern coast of the Honshu. This is caused by the active evaporation and convective moisture transfer from the sea surface. However, cloud liquid water content did not exceed 0.1-0.12 kg/m^2 on average.

B. Polar Low

A prolonged Cold Air Outbreak and explosive cyclogenesis

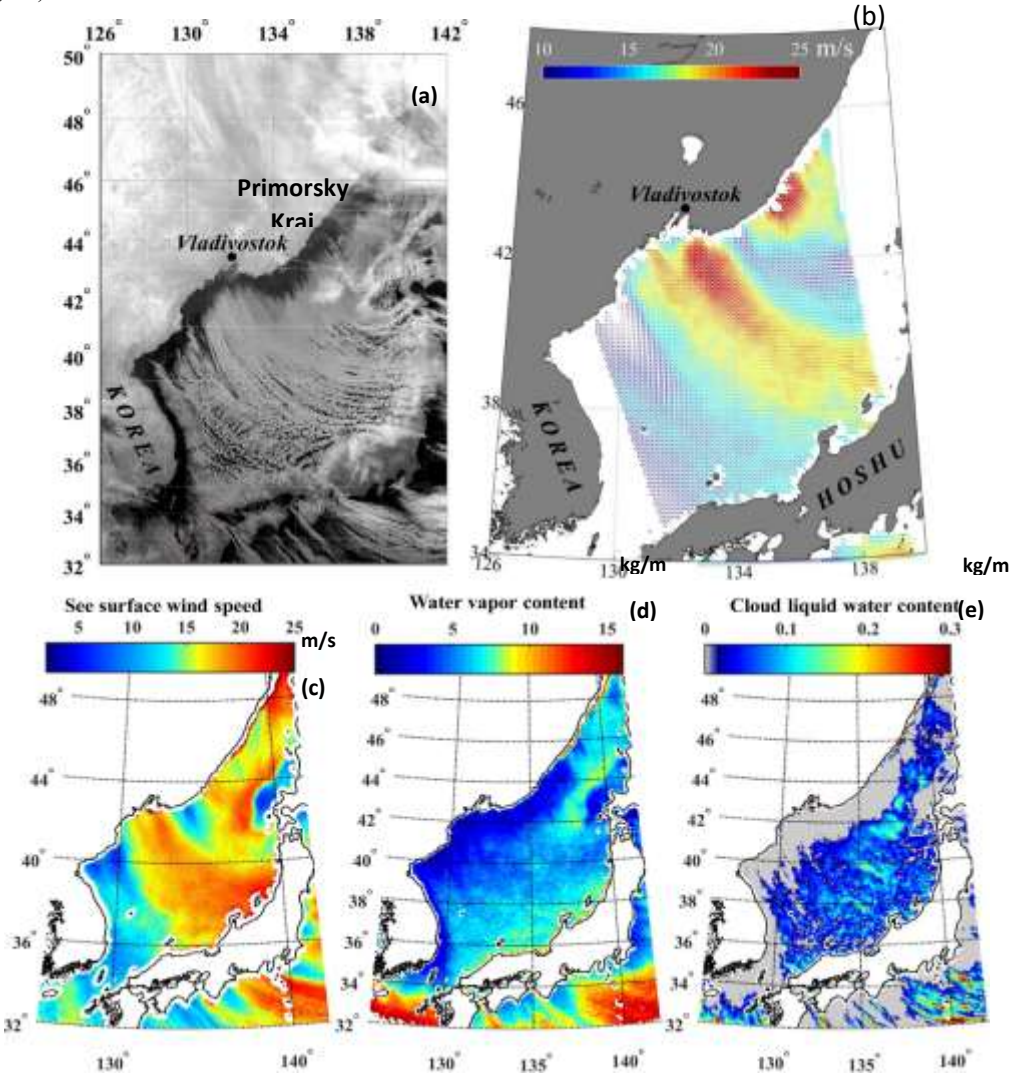

Figure 1. Cold Air Outbreak over the Sea of Japan January 24, 2018: (a) – VIIRS satellite infrared image of the convective cloud structures obtained from the Suomi NPP at 16:55; (b) – ocean surface wind vector measured by ASCAT from MetoOp-A/B at 12:30/13:05 UTC; (c) – sea surface wind speed, (d) – total atmospheric water vapor content and (e) – total cloud liquid water content retrieved from AMSR2 measurements at 17:00 UTC.

contributed to the development of intensive polar lows over the Sea of Japan.

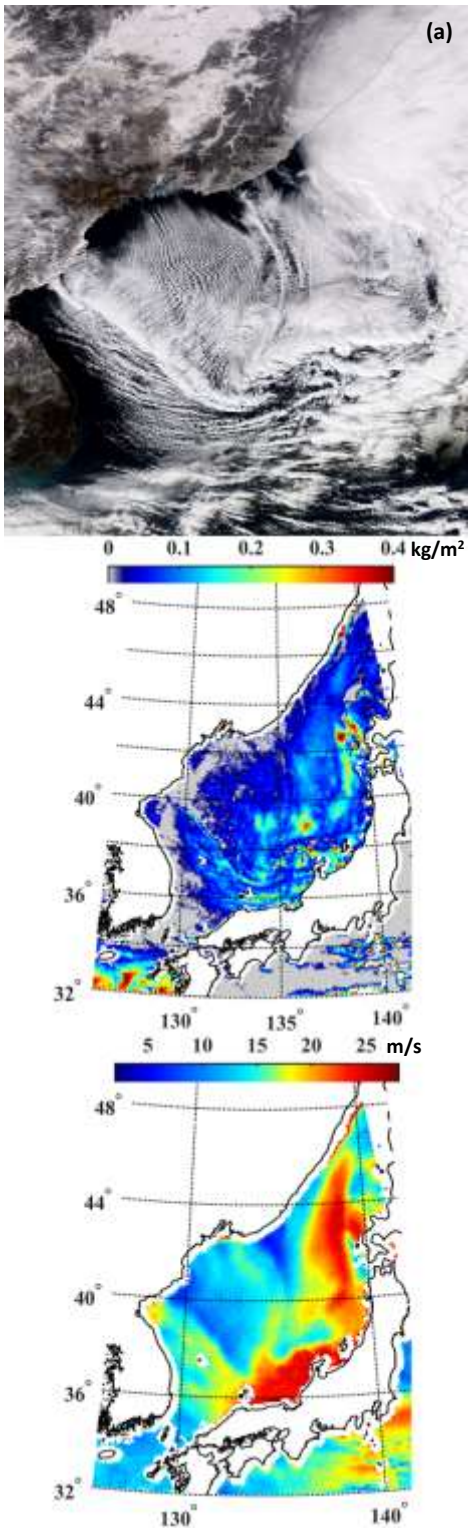

Figure 2. Mesoscale circulations over the Sea of Japan January 23, 2018: (a) – MODIS satellite visible image from Terra at 02:35; (b) – total cloud liquid water content and (c) – sea surface wind retrieved from AMSR2 measurements at 04:10 UTC. The numbers 1 and 2 indicate the positions of Polar Lows.

A meso-α-scale polar low (PL) occurred on January 22, 2018 over the central part of the sea in the rear of the extratropical cyclone. At the initial stage of development, it was not clearly expressed in the cloudy field. However, mesoscale circulation with a wind speed of 20 m/s was identified by ASCAT measurements at 01:36 UTC on January 23. The PL moved to the north-north-east and reached a peak in intensity at the turning point of the trajectory when its centre was located at the same latitude as the centre of the explosive extratropical cyclone (Fig. 3). In this case, ASCAT-based maximum wind speed in it was 25–28 m/s (Fig. 3a), while the AMSR2 showed values 30-32 m/s (Fig. 3b).

Moreover, on January 23, another polar low with a wind speed > 25 m/s developed off the northern coast of Korea (Fig. 2a, c). This mesocyclone was not detected in the pressure fields from operational analysis CFSv2 and reanalysis ERA5 and was identified in satellite images and the fields of ocean surface wind vector. Within a few hours, it PL moved southeast to the coast of Honshu, where it starts to decay.

C. Explosive extratropical cyclones

Intensive cold advection along the western periphery of upper-level low with a cold core over the coastal part of the Asian continent and the Sea of Japan contributed to the development of Explosive Cyclones (ECs) east of the Japanese islands. ECs – rapidly intensifying low-pressure systems with a drop in sea level pressure exceeding 24 hPa in 24 h relative to 60◦N (Gyakum et al., 1989). In this case, on January 22-23, during the day, the sea level pressure in the centre of the extratropical cyclone extremely dropped from 1004 to 958 hPa, and the wind speed according to the ASCAT measurements (MetOp-A, B satellites) reached 40-42 m/s. We assume that real wind speeds may be higher due to scatterometer limitations (Meissner et al., 2017).

Operational analysis CFSv2 and satellite measurements showed close sea surface wind speed throughout the entire period of cyclogenesis (fig. 3), but CFSv2 significantly underestimated the deepening of the low-pressure system. At the same time, the ERA5 showed low winds at speeds greater than 25 m/s (figure 3d).

A blocking ridge localized over the Bering Sea facilitated the cyclone path to the Sea of Okhotsk. Such synoptic processes, as a rule, cause severe weather in north-eastern Asia and, in particular, extreme cold conditions in the Primorsky Krai.

IV.CONCLUSIONS

This study examines multiscale extreme weather events (EWEs) over the northwestern Pacific Ocean associated with storm and hurricane wind conditions. The EWEs include: anomalous prolonged (6 days) marine cold-air outbreak (CAO) over the Sea of Japan, explosive cyclogenesis over the Kuroshio–Oyashio Extension region and intense polar lows (PLs) over the sea.

The combination of satellite active and passive microwave measurements and reanalysis data sets allowed us to consider the EWEs evolution in the fields of cloudiness, wind speed, and the moisture content in the atmosphere. We revealed PL with near hurricane winds over the coastal area of Primorsky Krai and storm-force wind jets off the continental coast of the Sea of Japan during CAO event, which represents a hazard to marine traffic.

It has been shown that ERA5 – the fifth generation the European Centre for Medium-Range Weather Forecasts atmospheric reanalysis – significantly underestimated the

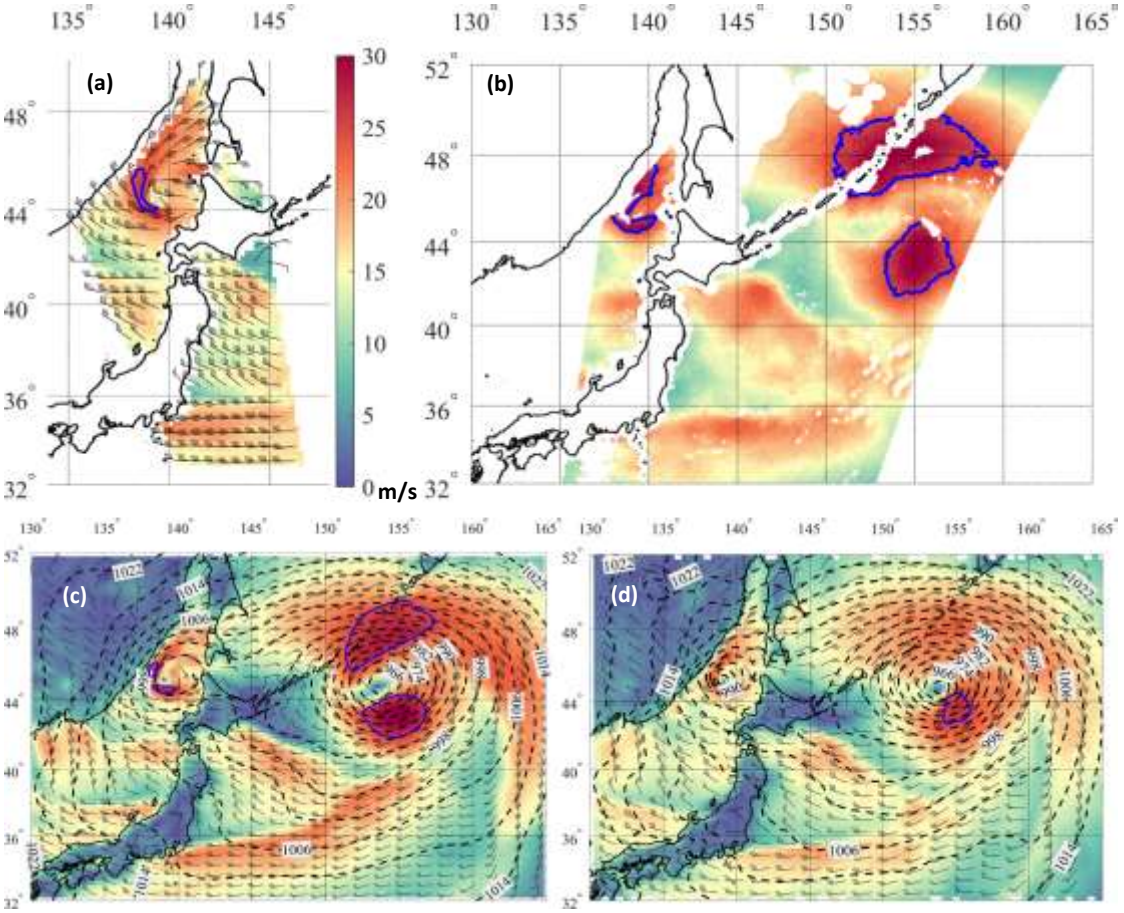

Figure 3. Satellite-derived and model near surface wind speed (m/s) and direction over the northwestern Pacific Ocean: (a) – measured by ASCAT from MetoOp-A/B at 11:45/12:40 UTC; (b) – retrieved from AMSR2 measurements at 16:05 UTC (c) and (d) – obtained from CFSv2 and ERA5 data sets at 16:00 UTC January 23, 2018. Blue lines indicate areas of storm and hurricane force winds. The dashed lines in fragments (c) and (d) – isobars of sea level pressure in hPa. The color scale – in m/s and the same for all fragments.

development of both synoptic- and mesoscale pressure systems in the field of sea surface wind speed. Moreover, the operational analyses of Climate Forecast System, Version 2, (CFSv2) of National Centers for Environmental Prediction significantly underestimated the deepening of the explosive cyclone over the Kuroshio–Oyashio Extension region.

We assume that atmospheric blocking due to the location of the tropospheric ridge over the Bering Sea and cold advection along the western periphery of the upper-level low over Northeast Asia and the Sea of Japan were decisive in the intensification of the weather systems.

ACKNOWLEDGEMENTS

This work was supported by the POI FEB RAS program No. AAAA-A17-117030110037-8.

REFERENCES

Etling D. and Brown R.A., 1993. Roll vortices in the planetary boundary layer: A review. *Boundary-Layer Meteorol.*, vol. 65, no. 3, pp. 215–248.

Føre I., Kristjánsson J.E., Kolstad E.W., Bracegirdle T.J., Saetra Ø., and Røsting B., 2012. A 'hurricane-like' polar low fuelled by sensible heat flux: high-resolution numerical simulations. Q. J. R. Meteorol. Soc., vol. 138, no. 666, pp. 1308–1324.

Gyakum J.R., Anderson J.R., Grumm R.H. and Gruner E.L., 1989. North Pacific cold-season surface cyclone activity: 1975–1983. Mon. Wea. Rev. vol. 117, pp. 1141–1155.

Meissner T., Ricciardulli L., and Wentz F.J., 2017. Capability of the SMAP mission to measure ocean surface winds in storms. *Bull. Amer. Meteor. Soc.*, vol. 98, pp. 1660–1677

Rasmussen E. and Turner J., 2003: Polar Lows: Mesoscale Weather Systems in the Polar Regions. *Cambridge University Press*, 612 pp.

Zabo lotskikh E.V., Mitnik L.M., Reul N., and Chapron B., 2015. New Possibilities for Geophysical Parameter Retrievals Opened by GCOM-W1 AMSR2. *IEEE J. Sel. Top. Appl. Earth Obs. Remote Sens.*, vol. 8, no. 9, pp. 4248–4261.

4D IOPS STRUCTURE OF THE SEA OF AZOV BASED ON SIMULATION AND DATA ASSIMILATION OF REGIONAL OCEAN COLOR PRODUCTS

T. Shul'ga [1], V. Suslin [1, 2]

[1] Marine Hydrophysical Institute of RAS, Kapitanskaya Str., 2, Sevastopol, 299011, Russia – shulgaty@mail.ru
[2]Sevastopol State University, Universitetskaya Str., 33, Sevastopol, 299053, Russia – slava.suslin@mhi-ras.ru

KEY WORDS: The Sea of Azov, Spectroradiometer MODIS, 3D Numerical Simulation, Data-assimilation, Bio-optical Indices, Non-living Organic Matter

ABSTRACT:
Nowadays, the scale of ecological problems is becoming threatening and causes extremely negative consequences to the ecosystems, especially for the shallow sea basins. The selected study area, the Sea of Azov, is a shallow sea linked by the narrow Kerch Strait to the Black Sea. Non-ferrous and steel plants located on its coast are dangerous for this area. The aim of this study is to estimate the total suspended matter in the seawater from January to July 2019. The main instrument of this study is related to the information of the satellite systems with high spatial resolution ensuring daily data occurrence for any monitoring area. Besides that, the numerical simulations tool was used in this work for filling the gaps due to satellite imagery unavailability and/or cloud covering. The ad hoc assimilation scheme allows using the bio-optical indices in the Sea of Azov for the Princeton Ocean Model. From spectroradiometer MODIS Ocean Color products, data for assimilation were reconstructed: total concentration of chlorophyll-a and phaeopigments, coefficients of light absorption by phytoplankton pigments, and non-living organic matter. Combined MODIS measurements and 3D simulation provide the maps of the bio-optical indices and the half-yearly cycle of the average values of bio-optical indices in the Sea of Azov.

I.INTRODUCTION

A. Motivation and background

A significant disadvantage of using satellite data to study suspended matter content in the Sea of Azov is the presence of gaps in available satellite data due to common problems associated with Ocean Color images (e.g. cloud cover). Combining the results of numerical simulation and remote sensing provides a more accurate reproduction of the state of seawater (Konik et al., 2019).
This work continues earlier studies (Shul'ga et al., 2018) and (Shul'ga et al., 2020) and contains new results supplemented by new bio-optical indices obtained using improved assimilation.

B. Study Area

The study area is the shallow Sea of Azov, bounded by the coordinates between 44.501° to 48°N and from 34° to 40.021°E linked to the Black Sea by the narrow Strait of Kerch (Figure 1). The study area is split into parts reflecting the distance from the mouth of the Don River. The borders of sub-regions correspond to the settlements: I – 45°25'N, 35°49'E (Shchelkino); II – 46°45′59″N, 36°47′55″E (Berdyansk); III 46°37.89′N, 37°48.21′E (Dolzhanskaya).

C. Datasets

We used standard products of the MODIS-Aqua and MODIS-Terra from Ocean Color (NASA, 2018a) and (NASA, 2018b) for investigating the total concentration of chlorophyll-a and phaeopigments, coefficients of light absorption by phytoplankton pigments and non-living organic matter in 2017–2019 in the Sea of Azov.
We used the 3D hydrodynamic Princeton Ocean Model over a domain of the Sea of Azov with 1 km horizontal resolution, vertically discretized into 11 terrain-following sigma levels.

Figure 1. The study area (the Sea of Azov) and its sub-regions

Validation of the model run was described in (Ivanov, 2014), highlighting a satisfactory agreement with the observed processes.
For 3D simulation, we used the hourly atmospheric forcing with 0.1° resolution in latitude and longitude from the SKIRON model forecasts (Kallos et al., 1997) for the same period (forecast.uoa.gr).
The MODIS measurements and SKIRON atmospheric data were interpolated on the model grid of the Sea of Azov (396×295) with the horizontal resolution of 1/59°×1/84° in latitude and longitude.

II.METHODS

A. Algorithm of the bio-optical indices determination

The essence of our approach was as follows: (1) the use of regional relationships between the measured values of light absorption and the combination obtained from the satellite products (the spectrum of remote-sensing reflectance $R_{RS}(\lambda)$

from the wavelength (λ) range of 600–700 nm, namely: center bands at 645, 667 and 678 nm); (2) correction taking into account scattering by suspended matter in the long-wavelength part of the spectrum and possible errors in an atmospheric correction, which was minimized by using the difference between the bands for close wavelengths.

The bio-optical index $a_{ph}(678)$ was obtained based on the found relationships between the absorption coefficient by phytoplankton at 678 nm and the combination $R_{RS}(667)$ and $R_{RS}(678)$. The next step was to obtain the index for the absorption of the colored component of the organic matter $a_{CDM}(438)$ based on the relationship between the remote-sensing reflectance $R_{RS}(\lambda)$ at 531 and 438 nm wavelength.

Other bio-optical characteristics – concentration the pheopigments (*TChl)* and the light backscattering coefficient by particles $b_{bp}(438)$ in the Sea of Azov were obtained according to MODIS measurements based on the known relationships (Suslin et al., 2016).

B. Methodology

The methodology includes three main stages:

(1) the processing of imaging spectroradiometer MODIS (oceancolor.gsfc.nasa.gov) and construction of the bio-optical indices maps, (2) the 3D simulation with Princeton Ocean Model using wind and atmospheric pressure from the SKIRON model, and (3) assimilation of the MODIS remote sensing data is time-synchronized with 3D simulation. Overall, the research plan contemplates three separate steps shown in Figure 2.

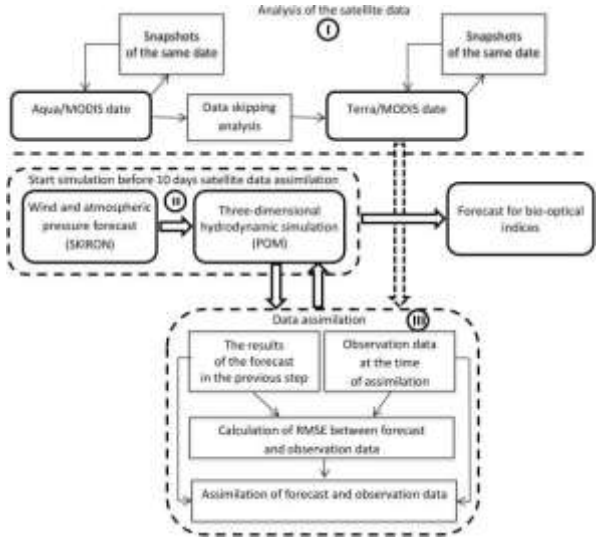

Figure 2. Scheme of the research plan

C. The assimilation system

The bio-optical indices maps are assimilated into the hydrodynamic model every time remote sensing data become available. The assimilation system is described in (Shul'ga, 2017). It is a sequential assimilation method based on the forecast-correction system. The short-term forecast vector from the previous step of assimilation is constructed based on the integration of the transport and diffusion equations in the 3D model. Its dimension equals the number of points in the model space, unlike the MODIS data observation vector with dimensions usually smaller. The assimilation scheme updates (i.e., "corrects") the forecasted states.

III. RESULTS AND DISCUSSION

A. The maps of the bio-optical indices

The proposed approach provides a detailed and long-term characterization of the variability of the fields of chlorophyll-a and phaeopigments, coefficients of light absorption by phytoplankton pigments and non-living organic matter in the Azov Sea. Such an approach made it possible to construct time-continuous maps of four bio-optical indices and, as a result, to get the 4D *IOPs* (the inherent optical properties) structure of the Sea of Azov.

As an example, Figure 3 shows the maps of the distribution of the optical index $a_{ph}(678)$ in January and May 2019 on the surface and at the bottom of the Sea of Azov.

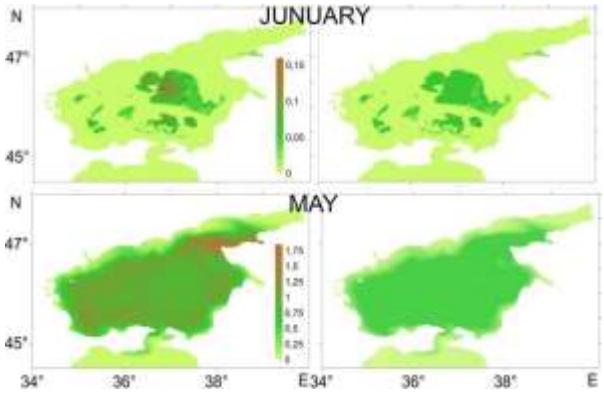

Figure 3. Maps of the bio-optical index $a_{ph}(678)$ in January and May 2019 in the surface (left) and at the bottom (right) of the Sea of Azov.

B. Half-yearly cycle of the average values of bio-optical indices

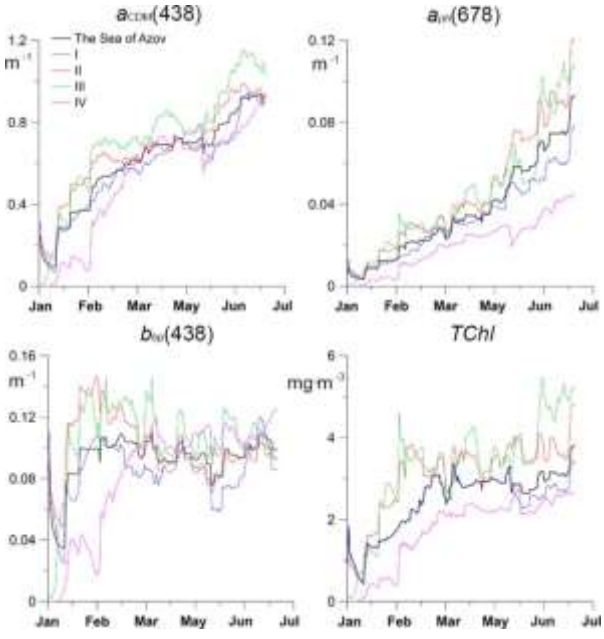

Figure 4. Average values of bio-optical indices: $a_{CDM}(438)$, $a_{ph}(678)$, $b_{bp}(438)$ and *Tchl* from January to July 2019.

As can be seen from Figure 4, at the beginning of spring and summer, there is a sharp increase in the bio-optical parameters. The trend of the average values of the indices is upward. This is consistent with long-term observations.

IV.CONCLUSIONS

Combined MODIS measurements and 3D simulation improve the prediction of the evolution of the suspended matter content in the Sea of Azov. We have developed a simulation framework that incorporates remote sensing MODIS data into a hydrodynamic model using sequential data assimilation.

V.FUTURE WORK

In the future, these results will be used to obtain photosynthetically active radiation in the water column and at the bottom of the sea.

ACKNOWLEDGEMENTS

The work was carried out within the framework of State Projects No. 0827-2019-0002 and No. 0827-2019-0004. The reported study was funded by RFBR according to the research projects No. 18-05-80025 and No. 18-45-920070.

REFERENCES

Ivanov, V. A., Cherkesov, L. V. and Shul'ga, T. Ya. 2014. Dynamic processes and their influence on the transformation of the passive admixture in the Sea of Azov. *Oceanology*. 54(4). pp. 426-434. https://doi.org/10.1134/S0001437014030023

Kallos, G., Nickovic, S., Papadopoulos, A. et al. 1997. The regional weather forecasting system SKIRON: An overview. In: *Proceedings of the Symposium on Regional Weather Prediction on Parallel Computer Environments*, Athens, Greece, pp. 109– 122

NASA Goddard Space Flight Center, 2018a. Ocean Ecology Laboratory, Ocean Biology Processing Group. Moderateresolution Imaging Spectroradiometer (MODIS) Aqua Ocean Color Data; Reprocessing. NASA OB.DAAC, Greenbelt, MD, USA. doi: data/10.5067/AQUA/MODIS/L2/OC/2018

NASA Goddard Space Flight Center, 2018b. Ocean Ecology Laboratory, Ocean Biology Processing Group. Moderateresolution Imaging Spectroradiometer (MODIS) Terra Ocean Color Data; Reprocessing. NASA OB.DAAC, Greenbelt, MD, USA. doi: data/10.5067/TERRA/MODIS/L2/OC/2018.

Konik, M., Kowalevski, M., Bradtke, K., and Darecki M., 2019. The operational method of filling information gaps in satellite imagery using numerical models. International Journal of Applied Earth Observation and Geoinformation. 75. pp. 66-82. https://doi.org/10.3390/rs11242982

Shul'ga, T.Ya., 2017. Evolution of the pollution in the Sea of Azov by satellite data and simulation results. *Vestnik Udmurtskogo Universiteta: Matematika, Mekhanika, Kompyuternye Nauki.* 27(3). pp. 450-459. https://doi.org/10.20537/vm170312

Shul'ga, T.Ya. and Suslin, V.V., 2018. Investigation of the evolution of the suspended solids in the Sea of Azov based on the assimilation of satellite data in a hydrodynamic model. *Fundamentalnaya i Prikladnaya Gidrofizika*. 11(3). pp. 73-80. https://doi.org/10.7868/S2073667318030097

Shul'ga, T.Ya., Suslin, V.V., Shukalo, D.M., and Ingerov, A.V., 2020. Research of the relations between the seasonal variability of salinity and bio-optical features in the Sea of Azov using the satellite data in the visible spectrum range. *Fundamentalnaya i Prikladnaya Gidrofizika*. 13(2). pp. 68-75. https://doi.org/10.7868/S2073667320020082

Suslin, V. V. and Churilova, T. Ya. 2016. A regional algorithm for separating light absorption by chlorophyll-a and coloured detrital matter in the Black Sea, using 480– 560 nm bands from ocean colour scanners. *Int. J. Remote Sensing*. 37(18), pp. 4380-400. https://doi.org/10.1080/01431161.2016.1211350

ASSESSMENT OF COASTAL MANAGEMENT FOR SINKING COASTAL AREA

Dewayany Sutrisno [1] Muhammad Helmi [2] and Mulyanto Darmawan [3]
[13] Badan informasi geospasial
Jalan Raya Jakarta – Bogor km 46 Cibinong 16911 – (dewayany, drmoel2011)@gmail.com
[2] Fakultas Perikanan dan Ilmu Kelautan, Universitas Diponegoro
Jl. Prof. H. Soedarto, S.H, Tembalang, Kec. Tembalang, Kota Semarang, Jawa Tengah 50275– muhammadhelmi69@gmail.com

KEY WORDS: Coastal Management, Coastal Degradation, Spatial Planning

ABSTRACT:

The degradation of coastal areas is affected by numerous factors, either by nature or human social-economic activities. Consequently, spatial planning, which considers the ecosystem, should be assessed. This article aims to review the best method for spatial planning based on ecosystem adaptation. This article evaluated the sinking coastal area in North Java coast-Indonesia using the change detection method, spatial analysis, and review from experts. The findings indicate the need for the coastal protection zone and silvo-fisheries activities as the coastal planning solutions. Other differences in spatial planning are better to consider the existing ecosystem as part of coastal zonation.

I.INTRODUCTION

The coastal area is influenced by numerous factors that interact with one another, either by nature or human drivers. Combining social activities in exploiting natural resources with the phenomenon of climate change in the oceans triggers changes in the coastal environment. In some cases, coastal degradation, coastal biodiversity loss, and the decrease of the coastal inhabitants' welfare have occurred. The risks create an urgent need for actions on the management of adaptation and mitigation that cannot be implemented by the mentally model only but needs to be spatially assessed. For example, look at the Northern Central Java coast, Indonesia. Some area of this coastal region is sinking, and the coastline is moving landward. This coastal area landscape consists of wetland, channels, and muddy beaches, which has been slowly drowning caused by land conversion, relative sea-level rise, high tide, and groundwater discharge. Therefore, this article aims to review the best method for spatial planning based on ecosystem adaptation. For this purpose, a study area on the northern coast of Central Java Province Indonesia is selected. This coastal flooding occurs daily in this area cause of the high tide that local people, namely rob.

II.METHOD

The coastal sinking review method is based on coastal changed detection, spatial analysis, and review of the findings based on the expert judgment approach. The multi-temporal Landsat data acquired in 1973 and 2020 was used to review the method and develop some spatial data. The band transformation was applied for coastal change detection analysis, and spatial analysis was used to assess the mitigation and adaptation plan. The expert judgment review was then used to evaluate the best spatial planning-based ecosystem adaptation in the study area.

III.RESULT AND DISCUSSION

This study's result indicates a significant impact on the coastal decrease, as can be seen in Figure 1.

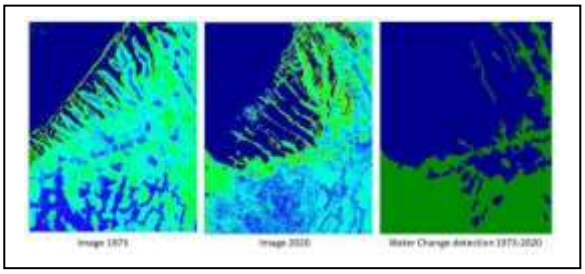

Figure 1. Coastal change 1972-2020

The coastal area has retreat more than 5000 m landward, which causes land-use changes and changes in the local people's livelihood.

Previously, this area was agricultural land but then has been changed into ponds. The existence of these ponds is threatened by tidal waves caused by climate and environmental change. Due to the study's aim that focuses on ecosystem adaptation, the spatial analysis of the area should consider the coastal green belt and marine culture as part of the ecosystem-based planning. A previous study of land suitability analysis suggested that the area is suitable for cultivation activities. Since most of the area has been developed as marine culture, silvo-fisheries method is the best option to mitigate the tidal wave's impact. Priyanto (2019) supports the idea that mixed mangrove aquaculture (MMA) is the best solution to maintain the coastal agricultural area's sustainability.

A review on mitigation and adaptation, which has been employed by the local government and local people by using the combination of hard and soft engineering as the coastal protection, indicates some success and failure in developing the coastal protection zone. A successful one shows that the land accretion was occurred (see figure 2), followed by the rapid growth of mangrove plants. Some failures occurred because of the lack of analysis of the characteristics of the area's oceanographic parameter (Sugiyanto, 2019), which should be assessed prior to the implementation of the protection engineering (Figure 3).

Figure 2. Accretion and coastal protection zone (Helmi, 2019; Priyanto, 2019)

Figure 3. The failure in coastal protection engineering (Sugianto, 2019).

The silvo-fisheries method's implementation indicates that ponds protected by mangroves can be more sustainable than those that are not (figure 4).

Figure 4, The example of the function of silvo-fishery (source: google map).

The regional spatial plan plans to develop this prone area as cultivation zones, including housing, business, and agriculture/fisheries land. Regardless of the regional development plans, the mangrove ecosystem's existence and the methods of protecting its cultivation efforts should still be considered. Zainuri and Ismanto (2019) State the importance of coastal ecosystems for coastal zonation plans that will support the biological, ecological, biophysical, and anthropocentric aspects of the coastal environment and its related livelihood (Zainuri and Ismanto, 2019). Of course, this review has some weaknesses. Therefore, further research involving multi- disciplinary needs to be carried out to bridge the coastal planning and the necessity to maintain the coastal environment sustainability

IV.CONCLUSION

Considering the current issues of coastal sinking, the evaluation based on the study's aim indicates the need for the coastal protection zone and silvo-fisheries activities as the coastal planning solutions. Other differences in spatial planning are better to consider the coastal ecosystem, such as mangrove as part of coastal planning to maintain the sustainability of the coastal environment

ACKNOWLEDGEMENTS

All authors are equally contributing as the main contributors. This article is part of the project of the Asia Pacific Network for Global Change Research (APN). Therefore, we would like to express our deepest gratitude to APN, who has funded this activity and also to all collaborators involved in this activity.

REFERENCES

Helmi, M. 2019. FGD dan Kick Off Meeting Integrated Coastal Landscape Management: An Adaptation to Related Climate Change Impact. Case Study: Sayung District, Demak, Central Java. Presented on The Kick Off Meetings of Integrated Coastal Landscape Management: An Adaptation to Related Climate Change Impact, Semarang-Indonesia

Zainuri, M. and A. Ismanto. Integrated Coastal Zone Management (Iczm) Di Pantura Propinsi Jawa Tengah Tahun 2019. Presented on The Kick Off Meetings of Integrated Coastal Landscape Management: An Adaptation to Related Climate Change Impact, Semarang-Indonesia

Priyanto, E.B. 2019. Rehablitasi Berbasis Ekosistem Pesisir Pembelajaran Dari Lapangan. Presented on The Kick Off Meetings of Integrated Coastal Landscape Management: An Adaptation to Related Climate Change Impact, Semarang-Indonesia.

Sugianto, D.N. 2019. Analisis Parameter Oseanografi Dan Mitigasi Kerusakan Pantai Di Wilayah Pesisir. Presented on The Kick Off Meetings of Integrated Coastal Landscape Management: An Adaptation to Related Climate Change Impact, Semarang-Indonesia

ESTIMATING SURFACE WIND SPEED IN TROPICAL CYCLONE FROM SATELLITE ALTIMETER MEASUREMENT AND MACHINE LEARNING TECHNIQUES

Syarawi M. H. Sharoni[1,2], Mohd Nadzri Md. Reba[1,3]

[1]Department of Geoinformation, Faculty of Built Environment and Surveying, Universiti Teknologi Malaysia, 81310 Skudai Johor, Malaysia.
syarawimuhammadhusni@graduate.utm.my, nadzri@utm.my
[2]School of Physics, Universiti Sains Malaysia, Penang, Malaysia.
[3]Geosciences and Digital Earth Centre (INSTeG), Research Institute for Sustainability and Environment (RISE), Universiti Teknologi Malaysia, Johor, Malaysia.

KEYWORDS: Altimeter; Machine Learning; Sea Surface Wind Speed; and Tropical Cyclone

ABSTRACT:

Sea surface wind speed can be estimated from altimeter satellite with high along-track resolution. In calm and normal conditions, the established geophysical model function from Ku-band backscatter for Jason-2 and Jason-3 (Jasons, henceforth) has shown good accuracy. However, in extreme conditions such as tropical cyclones, the ocean-atmosphere interactions have become very complex thus; single parameter estimation can become problematic. The accuracy is reduced at wind speed greater than 18 m/s and further contamination from rain towards Ku-band backscatter has exacerbated the estimated wind speed. Therefore, this study intended to incorporate several others Jason's parameters [C-band backscatter, significant wave height (SWH) at Ku- and C-band, brightness temperature at 18.7- and 34.0-GHz, and liquid water content (LWC)] to estimated sea surface wind speed inside the tropical cyclone. To incorporate multiple parameters, the application of machine learning techniques, including Artificial Neural Network (ANN), Support Vector Machine (SVM) regression, and Gaussian Process Regression (GPR), has been used and compared to the existing GMF. Statistical analysis has demonstrated significant accuracy improvement in several tropical cyclone crossing. This study reaffirms the unique ability of altimeter satellites in estimating more accurate wind speed by incorporating simultaneous physical parameters observed within a complex environment.

I.INTRODUCTION

General Instructions

Satellite altimeter has demonstrated its ability in deriving sea surface wind speed globally with the accuracy of 1.5 m/s (Ribal and Young, 2019). Most of the altimeter wind speed algorithm is derived from Ku-band backscattered over the specular sea surface reflection. However, the developed algorithm is limited to neutral atmospheric stability condition at low to moderate wind speed range (0-15 m/s) (Abdalla, 2012). The complex ocean-atmosphere interactions that existed inside the tropical cyclone environment have impaired the accuracy of the estimated wind speed. The inevitable rainbands that exist inside the giant tropical cyclone structure with measured wind speed can easily rise to more than 30 m/s has limited the applicability of the existing algorithm. Although the high wind speed tuning has been proposed by the Young (1993) and later followed by Quilfen et al. (2011), the Ku-band backscatter signal is still suffered in a rainy tropical cyclone environment. Studies demonstrated that rain contamination towards Ku-band signal is 40 times more than towards C-band (Xu and Stoffelen, 2019).

.

The ability of altimeter derived physical parameters inside the tropical cyclone environment has been demonstrated by some studies (Scharroo et al., 2005; Carrere et al., 2009). The altimeter can provide a high along-track resolution of significant wave height (SWH) which can also be used as an input to the wind speed estimation. The study indicated that the wave age can have a direct impact on how altimetric signal altered when reflected from the sea surface (Zhao and Toba, 2003), with reported accuracy improvement when incorporate SWH into their estimation model (Gourrion et al., 2002; Lillibridge et al., 2014). With all the recent altimeter satellite is always accompanied by a radiometer onboard the same platform, this has opened the new perspective of incorporating radiometric observations into wind speed estimation. The inclusion of environmental parameters in a complex tropical cyclone environment is anticipated to improve the accuracy of the estimated wind speed. The liquid water content derived from radiometric brightness temperatures is suggested to emulate the rainy condition that modified the principal altimetric signal inside the tropical cyclone. It has been proved in several studies where the accuracy of the estimated wind speed from scatterometer can be increased by incorporating simultaneous brightness temperature (Stiles et al., 2014; Xu et al., 2018).

However, incorporating all the mention parameters into conventional algorithms is a complicated task. For that reason, we explore the advantages of the machine learning technique in making multi-parameter relations to estimate wind speed in a complex tropical cyclone environment. The performances of the estimated wind speed from newly developed models are then compared with the existing operational algorithm.

II.DATA AND METHODLOGY

Jasons Altimeter Data

Altimeter satellite was designed purposely to observe sea surface globally. The principal signal measurement from the normalized radar cross-section (NRCS) backscatter reflected upon sea surface roughness proven can be used for sea surface wind speed (Ribal & Young, 2019). The Joint Altimetry Satellite Oceanography Network (Jason) is a series

of satellite microwave altimeter jointly organized by the National Aeronautics and Space Administration (NASA), the Centre National d'Etudes Spatiales (CNES, France), the European Organisation for the Exploitation of Meteorological Satellites (EUMETSAT) and the National Oceanic and Atmospheric Administration (NOAA) can provide wind speed with high accuracy in normal condition. Fully validated and research quality 1-Hz Geophysical Data Record (GDR) product of Jason-2 and Jason-3 (addressed as Jasons) from the reprocesses Archiving, Validation, and Interpretation of Satellite Oceanographic Data (AVISO) database were extracted and used in this study. Dual-frequency backscatter and significant wave height derived from Poseidon altimetric sensor with simultaneous brightness temperature at 18.7 GHz and 34.0 GHz and its derived Liquid Water Content parameters measured by onboard Advanced Microwave Radiometer were used as inputs to estimates the wind speed in tropical cyclone environment. Several studies have investigated the usefulness of incorporating these parameters to enhance the better quality altimetric signal in a complex environment (Ali et al., 2015; Jiang et al., 2020).

MetOps Scatterometer Data

The Advanced Scatterometer (ASCAT) on-board the Meteorological Operational (MetOp) satellites managed by EUMETSAT and European Space Agency (ESA) provides sea surface wind speed derived from C-band (5.228 GHz) radar backscatter. This study used ASCAT Level 2 Ocean Surface Wind Vectors optimized for Coastal Ocean product with a resolution of 12.5 x 12.5 km from the MetOp-A and MetOp-B (hereafter defined as MetOps) downloaded from the Physical Oceanography Distributed Active Archive Center (PODAAC). Extensive sea surface wind speed validation from CMOD5.n model against buoy and European Centre for Medium- Range Weather Forecast (ECMWF) and other satellites measurements were conducted by several studies (Verspeek et al., 2009; Soisuvarn et al., 2012). Weaker rain contamination on the C-band signal demonstrated a major advantage over Ku-band when used in rainy conditions inevitably existed inside tropical cyclones (Tournadre & Quilfen, 2003; Xu & Stoffelen, 2019). In addition, ASCAT wind speed has been used as the supporting data to Himawari 8/9 for tropical cyclone analysis at the Japan Meteorological Agency (Bessho et al., 2016). For this reason, this study accepts the estimated wind speed to the collocated Jasons parameters for wind speed modelling discussed in the later section.

Data Filtering and Match-Up

Satellite crossing of Jasons and MetOps have filtered within the 349 tropical cyclones outermost wind radius that occurred between 2015 and 2018 globally. Collocated match-up points between both satellites were obtained with the criteria of maximum 0.25° spatial distance and temporal gaps of less than 30 minutes. A total of 19,803 collocated points were extracted. To ensure only high-quality data was used, only match-up samples that hold a good quality of backscatter, significant wave height and brightness temperatures were accepted. The final 16,922 Jasons-MetOps match-up points were further investigated.

Machine Learning Techniques

All the match-up samples have been divided into training (80%) and testing (20%) datasets. Seven input parameters are assigned, including backscatter and significant wave height at Ku- and C-band frequency, brightness temperature at 18.7 and 34.0 GHz, and liquid water content. Collocated MetOps wind speed is assigned as the targeted output. Few machine learning techniques have been proposed to be used in this study, including Artificial Neural Network (ANN), Support Vector Machine (SVM), and Gaussian Process Regression (GPR). Statistical analysis of bias, root mean square error (RMSE), and Pearson's correlation (R) between the model estimated to MetOps wind speed is calculated.

III.EARLY RESULT & DISCUSSIONS

The performances of the estimated wind speed from all the machine learning techniques applied are summarized in the table below. The result indicated that RMSE of all developed machine learning models has reduced from more than 2 m/s for the operation wind speed product to around 1 m/s. Improved R between Jasons estimated wind speed to the MetOps also suggest that the developed models are almost similar to the observed wind speed from the scatterometer.

REFERENCES

Abdalla, S. (2012). Ku-band radar altimeter surface wind speed algorithm. Marine Geodesy, 35(sup1), 276-298.

Ali, M. M., Bhowmick, S. A., Sharma, R., Chaudhury, A., Pezzullo, J. C., Bourassa, M. A., ... & Niharika,
K. (2015). An artificial neural network model function (AMF) for saral-altika winds. IEEE Journal of Selected Topics in Applied Earth Observations and Remote Sensing, 8(11), 5317-5323.

Bessho, K., Date, K., Hayashi, M., Ikeda, A., Imai, T., Inoue, H., ... & Okuyama, A. (2016). An introduction to Himawari-8/9—Japan's new-generation geostationary meteorological satellites. Journal of the Meteorological Society of Japan. Ser. II, 94(2), 151-183.

Carrère, L., Mertz, F., Dorandeu, J., Quilfen, Y., & Patoux, J. (2009). Observing and studying extreme low pressure events with altimetry. Sensors, 9(3), 1306-1329.

Gourrion, J., Vandemark, D., Bailey, S., Chapron, B., Gommenginger, G. P., Challenor, P. G., & Srokosz,
M. A. (2002). A two-parameter wind speed algorithm for Ku-band altimeters. Journal of Atmospheric and Oceanic technology, 19(12), 2030-2048.

Jiang, H., Zheng, H., & Mu, L. (2020). Improving Altimeter Wind Speed Retrievals Using Ocean Wave Parameters. IEEE Journal of Selected Topics in Applied Earth Observations and Remote Sensing, 13, 1917-1924.

Lillibridge, J., Scharroo, R., Abdalla, S., & Vandemark, D. (2014). One-and two-dimensional wind speed models for Ka-band altimetry. Journal of Atmospheric and Oceanic Technology, 31(3), 630-638.

Quilfen, Y., Vandemark, D., Chapron, B., Feng, H., & Sienkiewicz, J. (2011). Estimating gale to hurricane force

winds using the satellite altimeter. Journal of Atmospheric and Oceanic Technology, 28(4), 453-458.

Ribal, A., & Young, I. R. (2019). 33 years of globally calibrated wave height and wind speed data based on altimeter observations. Scientific data, 6(1), 1-15.

Scharroo, R., Smith, W. H., & Lillibridge, J. L. (2005). Satellite altimetry and the intensification of Hurricane Katrina. Eos, Transactions American Geophysical Union, 86(40), 366-366.

Soisuvarn, S., Jelenak, Z., Chang, P. S., Alsweiss, S. O., & Zhu, Q. (2012). CMOD5. H—A high wind geophysical model function for C-band vertically polarized satellite scatterometer measurements. IEEE Transactions on Geoscience and Remote Sensing, 51(6), 3744-3760.

Stiles, B. W., Danielson, R. E., Poulsen, W. L., Brennan, M. J., Hristova-Veleva, S., Shen, T. P., & Fore,
A. G. (2014). Optimized tropical cyclone winds from QuikSCAT: A neural network approach. IEEE Transactions on Geoscience and Remote Sensing, 52(11), 7418-7434.

Tournadre, J., & Quilfen, Y. (2003). Impact of rain cell on scatterometer data: 1. Theory and modeling. Journal of Geophysical Research: Oceans, 108(C7).

Verspeek, J., Stoffelen, A., Portabella, M., Bonekamp, H., Anderson, C., & Saldaña, J. F. (2009). Validation and calibration of ASCAT using CMOD5. n. IEEE Transactions on Geoscience and Remote Sensing, 48(1), 386-395.

Xu, X., & Stoffelen, A. (2019). Improved Rain Screening for Ku-Band Wind Scatterometry. IEEE Transactions on Geoscience and Remote Sensing, 58(4), 2494-2503.

Xu, X., Dong, X., Zhu, D., & Lang, S. (2018). High Winds From Combined Active and Passive Measurements of HY-2A Satellite. IEEE Journal of Selected Topics in Applied Earth Observations and Remote Sensing, 11(11), 4339-4348.

Young, I. R. (1993). An estimate of the Geosat altimeter wind speed algorithm at high wind speeds. Journal of Geophysical Research: Oceans, 98(C11), 20275-20285.

Zhao, D., & Toba, Y. (2003). A spectral approach for determining altimeter wind speed model functions. Journal of Oceanography, 59(2), 235-244.

ESTIMATION OF CHLOROPHYLL-A CONCENTRATION USING BAND RATIO AND MACHINE LEARNING TECHNIQUE IN JOHOR WATERS

Fatin Nabihah Syahira Ridzuan [1], Mohd Nadzri Md Reba [1,2], Monaliza Mohd Din [3], Mazlan Hashim [1,2], Po Teen Lim [3,4], Zaharah Ibrahim [3], Mohd Firdaus Abdul-Wahab [3]

[1] Faculty of Built Environment & Surveying, Universiti Teknologi Malaysia, 81310, Johor Bahru, Johor, Malaysia - fatinabihahsyahira@gmail.com; nadzri@utm.my; mazlanhashim@utm.my.
[2] Geoscience and Digital Earth Centre (INSTeG), Research Institute for Sustainability and Environment (RISE), Universiti Teknologi Malaysia, 81310, Johor Bahru, Johor, Malaysia
[3] Faculty of Biosciences & Medical Engineering (FBME), Universiti Teknologi Malaysia, 81310, Johor Bahru, Johor, Malaysia - monaliza_mdin@yahoo.com; zaharah@utm.my; firdausw@utm.my
[4] Institute of Ocean and Earth Sciences, University of Malaya, 16310 Bachok, Kelantan, Malaysia - ptlim@um.edu.my

KEY WORDS: Chlorophyll-A, Remote Sensing, Band Ratio, Neural Network

ABSTRACT:

Remote sensing has great potential to provide the spatial and temporal coverage needed for effective monitoring of algal blooms by means of Chlorophyll-a (Chl-a) measurement. MODerate Resolution Imaging Spectroradiometer (MODIS) has been used widely in the mapping of the Chl-a worldwide. However, it is not suitable for the coastal area due to its low spatial resolution and the complexity of water led to overestimation. Landsat OLI and Sentinel 2 MSI has relatively fine spatial sampling, providing the capability to map optically active components (OACs) of coastal water. The combination of OLI and MSI will allow for more frequent observations at these moderate spatial resolutions. This study aims to develop the model for Chl-a estimation of OLI and MSI imageries over the West Johor Straits waters using machine learning techniques and to assess the accuracy of Chl-a estimates using on-site measurements. The Artificial Neural Network (ANN) techniques were applied to the selected OAC pixels. An improved accuracy of all techniques is evident when comparing with the traditional band-ratio ocean color algorithm. The band ratio showed relatively low performance (> 4 mg m^{-3}), but the ANN provided slightly higher accuracy (< 4 mg m^{-3}) in both MSI and OLI products. This study demonstrated the Chl-a model based on various OAC is almost universal and reliable regardless of the unknown relationship between OAC and spatio-temporal variability on satellite data initially determined by the machine learning method. The results provide the necessary information for developing an effective strategy in monitoring the coastal algal blooms.

I.INTRODUCTION

Phytoplankton is an essential aquatic photosynthesis organism and plays an important role as the main source of the food web that contributes to the world's primary production (Miguel et al., 2019). A large accumulative number of phytoplankton and macroalgal reported throughout the coastal areas of all continents (Sellner et al., 2003) dramatically impact the marine ecosystem, which resulted in significant economic losses and affects human health (Fletcher, 1996; Morand and Merceron, 2005). Conventionally, the in-situ measurement has been practiced measuring algae blooms. However, this process is generally considered tedious work and time-consuming. The water samples are collected once or twice a month and maybe increased, depends on the high and low-risk areas identified and the situations such as red tides and Paralytic Shellfish Poisoning (PSP) reported in the area. For the last 30 years, remote sensing has provided spatially and temporally comprehensive data of the photosynthesis pigment Chlorophyll-a, hereafter known as Chl-a, which is measured in mg m^{-3}, which strongly manifested to the phytoplankton.

The new sensors were invested in providing operational ocean colour monitoring daily with improved specification and instrument capabilities, such as OCTS (1996-1997), SeaWIFS (1997-2010) and MERIS (2002-2012) (O'Rilley and Werdel, 2019). NASA's next ocean colour sensor following the SeaWIFS, which is called MODIS has started its operations in 2002 and provided continuous observation for global coverage data and capable of monitoring across the visible spectrum and narrowly defined band that lowering the associated noise (Robinson, 2004). O'Reilly et al. (1998) developed the first version of the "band ratio" algorithm for the Sea-viewing Wide Field-of-view Sensor (SeaWiFS) data by exploiting a large optical dataset of remote-sensing reflectance, Rrs(λ), i.e., just above the sea surface, and in situ seawater chl-a measurements.

This empirical blue-green band ratio algorithm, named Ocean-Chlorophyll-2 (OC2), quantifies the chl-a concentration as a function of how much blue and green light is reflected from the sea surface (Dierssen, 2010). The standard OCx algorithm has been subject to additional updates and has been implemented as a three-band OC3 algorithm form (O'Reilly et al., 2000) on the Moderate Resolution Imaging Spectro-radiometer (MODIS) onboard the Aqua satellite. Although the empirical OCx algorithms have been developed to retrieve chl-a concentration in the open ocean for global scale studies, they exhibit poor accuracy at the basin/regional level (Gregg and Casey, 2004; Santoleri et al., 2008).

Among the existing satellites, MODIS and Landsat sensors are commonly used in retrieving Chl-a. In Peninsular Malaysia, MODIS sensors have been utilized in detecting and measuring chlorophyll concentration. However, these sensors are not suitable for monitoring Chl-a in the coastal area due to low spatial resolution. Lah et al. (2014) reported the MODIS OC3M standard algorithm had shown an overestimation of Chl-a in the Case-2 water of Malacca Straits. MODIS empirical Chl-a algorithm (OC3M) shows fairly acceptable Chl-a estimates with the absolute percentage difference (APD) <= 35% for clear

water or open sea (mostly by Case-1 water) but higher (APD >90%) near the coastal (probably by Case-2 water). The overestimation of Chl-a was potential to be occurred in Case 2 water due to the distribution of Chl-a, which is inhomogeneous within 1 km.

In West Johor Straits, 1km to 1 km MODIS resolution already covered different water types. Landsat with the 30-meter medium resolution has embarked a remarkable coastal mapping capability over the study area. However, its revisiting time of 16 days has slightly restricted the capability in providing a periodic scene of coastal water conditions. The launched of twin satellites of Sentinel-2 Multi-Spectral Instruments (MSI) in 2015 and 2017 may allow for more frequent observation at these moderate spatial resolutions. MSI is believed to provide fine spatial and temporal resolution (10-m resolutions and 5 to 10 days revisit time). The matching narrow blue (443,482 and 490 nm) and green bands (around 550-560 nm) to avoid the atmospheric absorption band at 567 to 637 nm. By the recent OLI and MSI data released, the empirical Chl-a estimation, particularly for Johor waters where the water depth is shallow and impact of various geomorphology from adjacent shores from Malaysia and Singapore, can be improved and performed at the highest spatial resolution. On top of that, there is still no study available using OLI and MSI in Johor water.

Therefore, it has motivated this study to develop the ocean colour model for Chl-a mapping in Johor waters on both OLI and MSI data through empirical modelling and using a machine learning method. Machine learning allows complicated water types to be correlated to the IOP and the measured Chl-a in-situ. The results will be used to assess the Chl-a variability within the Johor waters.

II.MATERIALS AND METHODS

A. Study Site

West Johor Straits were chosen as they were included in previous algae blooms event in Johor Bahru (Lim et al., 2012; Fisheries Research Institute Penang, 2017). This area is located nearest to the international boundary between Malaysia and Singapore and is considered as complex water with freshwater inflows from Sg. Pendas and Sg. Pulai, aquaculture farms, mangroves and influenced by tidal from the Straits of Johor and nearest oceanic current, as shown in Figure 1. The developments of the new residential and industrial area changed the landscape of the area. The development of Forest City attracts new tourism activity and a few industrial activities actively running at Port of Tanjung Pelepas and Tanjung Bin. Moreover, a few aquaculture farms were located in Kukup, Sg. Pulai and nearest Second Link Bridge. Mangrove habitat also can be found at Pulau Merambong and Tanjung Piai. The first bloom event of Prorocentrum Minimum was recorded in 2002 in Johor Bahru. In 2014 and 2015, another episode of algae blooms, Karlodinium Australe is recorded at Tanjung Kupang, Johor Bahru.

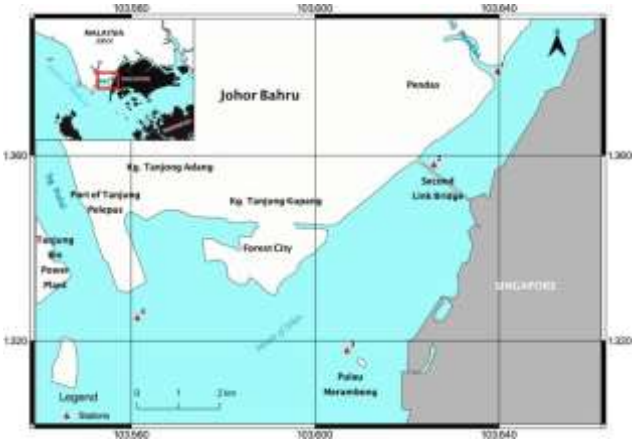

Figure 1. Location map of four sampling stations at West Johor Straits, which in situ Chl-a is collected.

B. In situ measurement

Phytoplankton samples were collected fortnightly during high tide from January 2017 to December 2018. Triplicates of 1-L water samples were collected at subsurface water using a Van Dorn water sampler for dissolved inorganic and chlorophyll a (Chl-a) analysis. For Chl-a analysis, 1-L seawater samples were filtered onto glass-fibre filters (Whatman®, UK). The filters were blotted dry, folded in aluminium foil, and kept frozen prior to Chl a extraction. Chl a was extracted by 90% acetone; and measured by using the multi-wavelengths spectrophotometer as described in Parsons et al., (1984).

C. Satellite Data

Landsat with the 30-meter medium resolution has embarked a remarkable coastal mapping capability, with 11 spectral bands channel in the visible/near-infrared (VNIR), short wave infrared spectral range (SWIR), panchromatic, cirrus and thermal infrared zone. However, its revisiting time of 16 days has slightly restricted the capability to monitor coastal water conditions. The twin satellites of Sentinel-2 MultiSpectral Instruments (MSI), S2A and S2B, respectively, were selected due to it spatial resolution of 10-m and a 10-day revisit period for every single Sentinel-2 and 5-days revisit period for the combined constellation over the study area. Level-1C data with 13 spectral channels in the visible, VNIR and SWIR were obtained from https://scihub.copernicus.eu/ for comprehensive Chl-a analysis. The level-1 data provide the Top of Atmospheric (TOA) Reflectance in fixed cartographic geometry and contain applied radiometric and geometric correction.

Chl-a retrieved from the satellite were match-up with in situ Chl-a based on the nearest date of measurements. The availability of match-up data in West Johor Straits is limited due to cloud cover, hence weaken the sensibility of the algorithm toward the case-2 water. The available cloud-free Level-1C data were used for Chl-a estimation from January 2017 to December 2018. The data were taken from a 3x3 window (90x90m for OLI; 30 x 30m for MSI) centered at sampling stations. Since the observation date is not generally coincident, the mean of the window was used as the matchup value. MSI and OLI overpass time and the closest acquisition date to that of the field survey were selected and processed (up to a few days apart).

D. Band ratio algorithms

Early in CZCS mission, Chl-a algorithm switched between two band ratios to estimate chlorophyll, which led to discontinuity in pigment estimation at switching value (O'Rilley et al.,1998). To overcome this problem, the maximum band ratio (MBR) algorithm has been conceived by O'Rilley et al. (1998) by relating the in situ Chl-a to reflectance band ratios, using a single fourth-order polynomial equation. The equation state as follows:

$$\log_{10}(\text{Chl-a}) = a_0 + a_1X + a_2X^2 + a_3X^3 + a_4X^4 \quad (1)$$

where a_n = polynomial fit coefficient

X = log of band ratio between two band

In this study, a sequence of blue-green band ratios was used to quantify Chl-a estimation (Rrs 443, Rrs 490 and Rrs 560 nm).

E. Artificial Neural Network (ANN)

By using the remote sensing reflectance from MSI and OLI, the estimation of Chl-a was constructed using ANN methods. ANN model has been widely applied as a modelling tool for water quality modelling and complex environmental processes (Park et al., 2018; Kim et al., 2015; Park et al., 2017). The ANN model is constructed via three layers (input, hidden and output layers) that are consist of nodes and connected by weight and bias. Too many layers and nodes may result in overfitting the ANN models (Farifteh at al., 2007).

The *Rrs* value in 443**,** 490, 560, 705, 740, 783 and 865 nm bands were used as input in the input layer and the in situ Chl-a data was used as the output in the output layer. ANN was trained sequentially and evaluated in terms of the square of the Pearson's correlation coefficient, R^2 and the root mean square error, RMSE.

III.RESULT AND DISCUSSION

A. Retrieval using Band Ratio

The performance of the band ratio algorithm was analysed for OLI and MSI, which involved a sequence of blue and green band ratio**.** The coefficients were listed in Table 1. Meanwhile, Table 2 presented the performance of band ratio in estimating Chl-a. concentration. Band ratio algorithm have shown low performance in coastal Chl-a study, with $R^2 = 0.214$ and $R^2 = 0.165$. For all ranges, the band ratio algorithm tended to underestimate and overestimate Chl-a concentrations. A relatively high and low magnitude of green band, 560 nm band dominates can cause the underestimation and overestimation of Chl-a concentration at coastal water.

Table 1. Coefficient of band ratio algorithm, involving Rrs 443 and Rrs 490, for OLI and MSI.

Sensor	Coefficient				
	a0	a1	a2	a3	a4
OLI	10.15	-9.686	-0.912	1.637	1.284
MSI	33.44	6.296	-5.009	-0.2296	1.245

Table 2. Performance of band ratio algorithm for OLI and MSI.

Sensor	Fitting		Validation	
	R^2	RMSE	R^2	RMSE
OLI	0.214	0.207	0.749	8.912
MSI	0.165	0.216	0.892	4.560

B. Retrieval using machine learning techniques

The performance of ANN models is shown in Table 3. For OLI, the best performance is at the combination of visible band, at 443, 490, 560 nm and 705 nm, the training step showed the highest R^2 value with 0.98 and the lowest RMSE value, 0.912. During the validation step, the RMSE was also lowest compared to the other *Rrs* combinations. The sensitivity of each Rrs at different wavelengths is also analysed in this study, as presented in Table 4. At 655 nm, the ratio is 0.61, which indicates that the network will work better without *Rrs* from 655nm.

Meanwhile, for MSI, the best performance is at the combination of visible band, at 443, 490, 560 nm and 705 nm, the training step showed the highest R2 value with 0.71 and the lowest RMSE value, 2.615. However, during the validation step, the highest R2 value is a combination of *Rrs* without 443 nm with 0.81 (R^2 value) and RMSE 1.749, Table 5. From sensitivity analysis (Table 6), the network will improve without Rrs at 655, 705, 740 and 865 nm.

Table 3. Performance of *Rrs* combination from OLI

λ (nm)	Training		Validation	
	R^2	RMSE	R^2	RMSE
443	0.83	1.873	0.76	3.008
490	0.74	3.279	0.69	3.822
560	0.58	3.479	0.41	5.450
655	0.98	0.912	0.69	2.864
705	0.85	2.250	0.16	4.839

Table 4. Sensitivity analysis of each *Rrs* at different wavelength for OLI

λ (nm)	R^2	Ratio
443	0.65	1.49
490	0.71	1.34
560	0.68	1.84
655	0.60	0.61
705	0.61	1.81

Table 5. Performance of *Rrs* combination from MSI

λ (nm)	Training		Validation	
	R2	RMSE	R2	RMSE
443	0.55	3.182	0.81	1.749
490	0.58	3.068	0.69	3.265
560	0.61	2.959	0.42	4.245
655	0.71	2.615	0.66	3.786
705	0.52	3.329	0.74	3.340
740	0.55	3.286	0.50	3.545
783	0.53	3.238	0.53	3.311
865	0.46	3.289	0.55	4.425

Table 6. Sensitivity analysis of each *Rrs* at a different wavelength for OLI and MSI

λ (nm)	R^2	Ratio
443	0.76	0.92
490	0.75	0.81
560	0.67	0.93
655	0.56	1.02
705	0.53	1.02
740	0.53	1.33
783	0.52	0.92
865	0.53	1.10

IV.CONCLUSION

The measurement and distribution of Chl-a matter, commonly related to phytoplankton and algae and the development of the improved method in retrieving Chl-a using satellite instruments has been anticipated by the community of scientists, researchers and aquatic managers for decades. In this paper, the performance of OC algorithms and optimal ANN model has been developed for Chl-a modelling. OC algorithms have shown poor performance using OLI and MSI satellite data in West Johor Straits water with R^2=0.214 and R^2=0.165, respectively. The development of ANN model in retrieving Chl-a show better estimation for Chl-a and is reliable regardless of the unknown relationship between OAC and spatio-temporal variability on satellite data, hence prove that machine learning techniques can potentially be used for the coastal region in monitoring Chl-a.

ACKNOWLEDGEMENTS

This study was supported by TRGS grant (vote no: R.J130000.7827.4L849), Ministry of Higher Education (MOHE) Malaysia. We are thankful to the Universiti Teknologi Malaysia for providing the facilities for this research.

REFERENCES

Ab Lah, N.Z., Reba, M.N.M. and Siswanto, E., 2014. An improved MODIS standard chlorophyll-a algorithm for Malacca Straits water. In IOP Conference Series: Earth and Environmental Science (Vol. 18, No. 1, p. 012113). IOP Publishing.

Farifteh, J., Van der Meer, F., Atzberger, C. and Carranza, E.J.M., 2007. Quantitative analysis of salt-affected soil reflectance spectra: A comparison of two adaptive methods (PLSR and ANN). Remote Sensing of Environment, 110(1), pp.59-78.

Fletcher, R.L., 1996. The occurrence of "green tides"—a review. In Marine benthic vegetation (pp. 7-43). Springer, Berlin, Heidelberg.

Gregg, W.W. and Casey, N.W., 2004. Global and regional evaluation of the SeaWiFS chlorophyll data set. Remote Sensing of Environment, 93(4), pp.463-479.

Kim, M., Baek, S., Ligaray, M., Pyo, J., Park, M. and Cho, K.H., 2015. Comparative studies of different imputation methods for recovering streamflow observation. Water, 7(12), pp.6847-6860.

Teen, L.P., Gires, U. and Pin, L.C., 2012. Harmful algal blooms in Malaysian waters. Sains Malaysiana, 41(12), pp.1509-1515.

Morand, P. and Merceron, M., 2005. Macroalgal population and sustainability. Journal of coastal research, 21(5 (215)), pp.1009- 1020.

O'Reilly, J.E., Maritorena, S., Mitchell, B.G., Siegel, D.A., Carder, K.L., Garver, S.A., Kahru, M. and McClain, C., 1998. Ocean color chlorophyll algorithms for SeaWiFS. Journal of Geophysical Research: Oceans, 103(C11), pp.24937-24953.

Park, Y., Pyo, J., Kwon, Y.S., Cha, Y., Lee, H., Kang, T. and Cho, K.H., 2017. Evaluating physico-chemical influences on cyanobacterial blooms using hyperspectral images in inland water, Korea. Water research, 126, pp.319-328.

Park, Y., Kim, M., Pachepsky, Y., Choi, S.H., Cho, J.G., Jeon, J. and Cho, K.H., 2018. Development of a nowcasting system using machine learning approaches to predict fecal contamination levels at recreational beaches in Korea. Journal of environmental quality, 47(5), pp.1094-1102.

Parsons, T.R., Maita, Y. and Lalli, C.M., 1984. Amanual of chemical and biological methods for seawater analysis. Pergamon Press.

Pour, A.B. and Hashim, M., 2016. Identification of High Potential Bays for HABs occurrence in Peninsular Malysia using Palsar Remote Sensing Data. The International Archives of Photogrammetry, Remote Sensing and Spatial Information Sciences, 42, p.97.

Santoleri, R., Volpe, G., Marullo, S. and Nardelli, B.B., 2008. Open waters optical remote sensing of the Mediterranean Sea. In Remote sensing of the European seas (pp. 103-116). Springer, Dordrecht.

Sellner, K.G., Doucette, G.J. and Kirkpatrick, G.J., 2003. Harmful algal blooms: causes, impacts and detection. Journal of Industrial Microbiology and Biotechnology, 30(7), pp.383-406.

THE CAPABILITIES OF AN ACOUSTIC WAVE GAUGE "TRIDENT" IN THE ARCTIC CONDITION

Yu. A. Titchenko [1], V. Yu. Karaev [1], R. V. Belyaev[2], M. S. Ryabkova[1], S. M. Kovalev[3], I. A. Kusheverskiy[3], E. M. Meshkov[1 1]

Department of Geophysical Researches, Institute of Applied Physics of the Russian Academy of Sciences, 46 Ul'yanov Street, Nizhny Novgorod, 603950, Russia – (yuriy, volody, mrjabkova)@ipfran.ru
[2] Department of Radiophysical Methods in Medicine, Institute of Applied Physics of the Russian Academy of Sciences, 46 Ul'yanov Street, Nizhny Novgorod, 603950, Russia – belyaev@ipfran.ru
[3] Ice Physics Laboratory of the Arctic and Antarctic Research Institute, 38 Bering str., St.Petersburg, 199397, Russia – (skovalev, iakusheversky)@aari.ru

KEYWORDS: Acoustic measurements, Arctic seas, Ice cover, Water level, Ice thickness

ABSTRACT:

This work is devoted to the description of a long-term experiment with an underwater sonar "Trident" at the polar research station "Ice Base Baranova Cape" of the Arctic and Antarctic Research Institute, conducted from January to April 2020. The device was placed to the bottom while special air cylinders supported the orientation of the sonar antenna vertically upward. The purpose of the experiment was to test the long-term operability of the device and to assess the capabilities of the acoustic wave gauge to carry out continuous remote measurements of the thickness of the ice cover and the water level. An important advantage of using hydroacoustic methods and the location of the device near the bottom is the ability to carry out measurements in any weather conditions and anywhere in the World Ocean, regardless of the presence and state of the ice cover. In the absence of ice cover, the instrument can provide information on surface waves.

I.INTRODUCTION

At present, orbital radars have become the main source of information on the parameters of the near-surface layer of the World Ocean. This is due to the possibility of obtaining up-to-date information on the water surface throughout the World Ocean, regardless of atmospheric conditions or illumination. However, this information can be used only after performing subsatellite measurements and subsequent validation of algorithms for the thematic processing of radar data. Therefore, the development of new measuring equipment for conducting subsatellite sea waves is an urgent task and should be carried out in parallel with the development of radar equipment.

A breakthrough in solving problems of subsatellite measurements and ground calibration will be the use of underwater hydroacoustics methods. This will make it possible to carry out measurements anywhere in the World Ocean without using stationary platforms and without disturbing the measured surface. In addition, underwater acoustics can work in any conditions, for example, in severe storms, and during precipitation, in the Arctic Ocean, as well as in freezing inland waters. Measurement of the main parameters of surface waves and characteristics of the ice cover using underwater sonar systems will for the first time allow validation of all thematic information that will be extracted from satellite data of future Russian and foreign spacecraft.

In addition, underwater hydroacoustics in inland waters will for the first time be able to provide constant monitoring of the processes of formation and destruction of ice cover, as well as information about changes in the water level in the reservoirs.

To measure the ice thickness according to sonar data, it is proposed to use a method based on measuring the time delay of an acoustic pulse between the lower and upper boundaries of the ice cover. Knowing the average speed of sound in the ice cover profile, one can estimate its thickness. A similar approach to

observing the lower and upper boundaries of the ice cover using a broadband ultrasonic signal in a laboratory experiment is considered in the following work (Bassett et al. 2020).

The thickness of the ice cover can be measured by space and aircraft laser (Abdalati et al. 2010) and radar (Kaleschke et al. 2015) altimeters. The thickness of the ice cover, in the presence of polynyas, is calculated from the difference in distances between the upper boundary of the ice cover and the surface of clear water.

Methods of hydroacoustic determination of ice thickness from underwater are known and actively used (R. Hudson, 1990), in which the time of arrival of the reflected pulse from the lower edge of the ice is used for analysis in combination with a hydrostatic pressure sensor.

Using this well-known method in conjunction with the method proposed in this paper for measuring the thickness of the ice cover will provide new information, for example, about the speed of sound propagation in ice and, ultimately, about the temperature gradient of the ice cover (the temperature at the top edge of the ice).

In the absence of ice cover, the acoustic wave gauge can provide information on surface waves. Our group has developed approaches for determining significant wave height and slope variance from the shape of the reflected pulse (Titchenko et al. 2019; Karaev et al. 2014). Moreover, the same surface parameters are determined, which are determined using space radars using the same wavelength.

II.EXPERIMENT DESCRIPTION

The "Trident" was installed at the bottom of the Shokalsky Strait in Amba Bay at a depth of 33 meters on January 20, 2020. At the time of installation near the bottom, salinity is 32.10- 32.17 ppm, water temperature is -1.75 ° C. The installation location on the map of the Northern Land Archipelago is shown in Figure 1.

Figure 1. Northern Land Archipelago and place of "Trident" installation

Photographs of the acoustic wave gouge "Trident" at the time of installation are shown in Figure 2 a) and b).

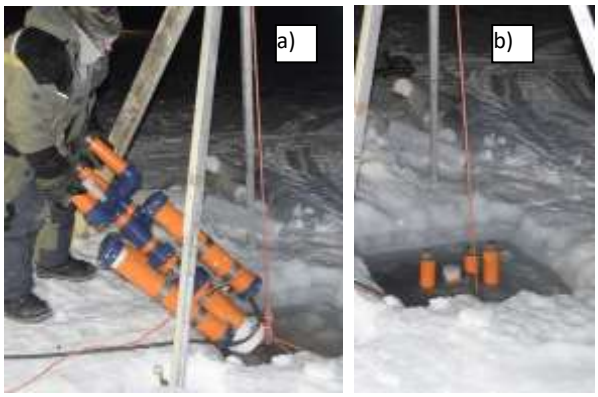

Figure 2. Photographs during the installation

The acoustic wave gauge "Trident" was manufactured at the IAP RAS, Nizhny Novgorod. The sonar antenna unit contains one transceiver antenna of the sonar pulse channel with a symmetrical directional pattern, the width of which at the half-power level is 15 degrees. The transceiving antenna is oriented vertically upward to the sea surface. The operating frequency of the generator is 200 kHz (the length of the radiated wave in water is 8 mm). The duration of the emitted pulse can be 1, 2, 4 and 8 periods of the generator, i.e. varies from 5 to 40 μs. The pulse repetition rate can be 5Hz, 10Hz, 40Hz, and 100Hz. There is also a 2-step adjustment of the power of the emitted pulse and an 8-step adjustment of the sensitivity of the receiving path.

In addition to the impulse channel, the sonar is equipped with a Doppler channel that allows us to measure the Doppler spectrum of the reflected signal. The Doppler channel is equipped with one continuously transmitting and one continuously receiving antenna with 15-degree radiation patterns, the same as for the pulse part. The emitted frequency is 200 kHz, the reception also occurs near this frequency.

The Doppler spectrum is formed by the movement of reflective objects. This channel is designed to measure the drift speed of the ice cover, but its operation will not be discussed here.

As auxiliary equipment, the acoustic wave gauge "Trident" is equipped with a two-axis inclinometer that measures the deviation of the pulse channel antenna from the vertical, as well as a hydrostatic pressure sensor with a measurement limit of 10 Bar.

The device is connected to a computer on the shore by a 600-meter cable that is laid on the ice surface with the help of special supports. The advantage of the cable connection in comparison with the autonomous operation mode, which is traditional for Arctic sonars, is the ability to measure the parameters of the ice cover and water level in real-time and access this information via the Internet.

The objectives of the study carried out with the Trident sonar at the polar station were, firstly, to test the possibility of detecting the lower and upper boundaries of the ice cover in sea conditions by an underwater sonar with an emitted acoustic wavelength of 8 mm, and, secondly, to test the long-term operability of the device in arctic conditions.

III.MEASUREMENT RESULTS

For example, consider the record of the impulse channel of the acoustic wave gauge "Trident" accumulated for 12 seconds (coherent accumulation of 60 pulses) in Figure 3.

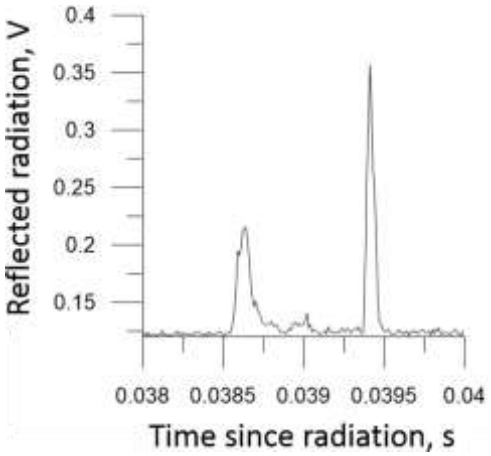

Figure 3. Reflected pulse accumulated for 12 seconds (coherent accumulation of 60 pulses)

Figure 3 shows an example of a reflected pulse obtained with the optimal settings of the acoustic wave gauge for a given pulse repetition rate (5 Hz), at the maximum emitted power and at the maximum possible gain for the reception.

The first maximum in Figure 3 corresponds to 29 meters, which is quite consistent with the distance from the emitter to the lower water-ice boundary. The second maximum is like the reflection from the upper ice-air boundary since from

theoretical considerations (ratios of acoustic impedances), the reflection from the upper boundary should be energetically greater than from the lower one. However, this conclusion requires confirmation in comparison with contact measurements, which will be carried out in future works.

Next, consider the recordings of the impulse channel made for 20 hours on March 3 and 6 in Figure 4.

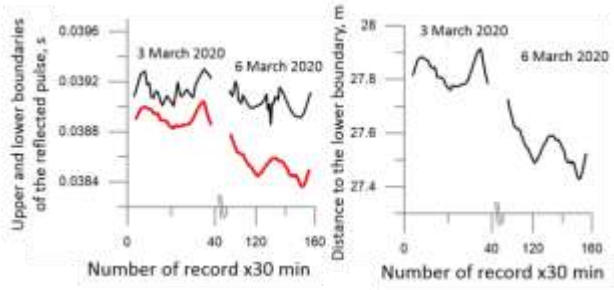

Figure 4. Upper and lower boundary dynamics on March 3 and 6

The figure on the left shows the time delay to the first reflection (red) and the second reflection (black) for 20 hours on March 3 and for 20 hours on March 6, where each point is averaging over 100 seconds for each next point is obtained after 30 minutes. It should be noted that, in addition to the thickness of the ice cover, the temperature of the upper edge of the ice cover has a large effect on the pulse delay between the lower and upper boundaries, which changes the gradient of the speed of sound in the ice. The right graph shows the conversion of the lower boundary delay to the range in meters. As a result, the graph illustrates the daily fluctuations in the lower edge of the ice cover for March 3 and 6, caused by the daily fluctuations in the water level.

IV.CONCLUSIONS

As a result of the work performed, a unique data set of measurements of the acoustic wave gauge "Trident" in arctic conditions was obtained. The possibility of observing the lower and upper boundaries of the ice cover using an underwater sonar with an emitted wavelength of 8 mm was confirmed. The device has been demonstrated to work in arctic conditions at a depth of 30 m from January to April. In the future, it is required to compare the measurement data with independent measurements of the ice thickness, as well as fluctuations in the ice cover and water level performed in the same period at the research station "Ice Base Baranova Cape".

ACKNOWLEDGEMENTS

This research was funded by the State target No. 0035–2019–0006.

REFERENCES

Abdalati W., Zwally H. J., Bindschadler R., Csatho B., Farrell S. L., Fricker H. A., Harding D., Kwok R., Lefsky M., Markus T., Marshak A., Neumann T., Palm S., Schutz B., Smith B., Spinhirne J., Webb C., 2010. The ICESat-2 Laser Altimetry Mission. *Proceedings of the IEEE*. 98(5), pp. 735-751.

Bassett C., Lavery A. C., Lyons A. P., Wilkinson J. P., Maksym T., 2020. Direct inference of first-year sea ice thickness using broadband acoustic backscattering. *The Journal of the Acoustical Society of America*. 147(2), pp. 824-838.

Hudson R., 1990. Annual measurement of sea-ice thickness using an upward-looking sonar. *Nature.* 344(6262), pp. 135-137.

Kaleschke L., Tian-Kunze X., Maaß N., Ricker R., Hendricks S., Drusch M., 2015. Improved retrieval of sea ice thickness from SMOS and CryoSat-2. *2015 IEEE International Geoscience and Remote Sensing Symposium (IGARSS).* pp. 5232-5235.

Karaev V. Y., Meshkov M. E., Titchenko Y. L., 2014. Underwater Acoustic Altimeter. *Radiophysics and Quantum Electronics*. 57(7), pp. 488-497.

Titchenko Y., Karaev V., Ryabkova M., Kuznetsova A., Meshkov E., 2019. Peculiarities of the Acoustic Pulse Formation Reflected by the Water Surface: a Numerical Experiments and the Results of Long-term Measurements Using the "Kalmar" Sonar. *OCEANS 2019*. pp. 1-7.

OIL SPILLS IN THE PERSIAN GULF AND THEIR DISTRIBUTION BASED ON SATELLITE MONITORING WITH SAR

A.Yu. Ivanov[1], N.V. Evtushenko[1], V.M. Evtushenko[1], N.V. Terleeva[1]

[1]Shirshov Institute of Oceanology Russian Academy of Sciences, Nakhimovsky 36, Moscow, 117997, Russia
ivanoff@ocean.ru

KEY WORDS: Persian Gulf, Oil spills, SAR images, Satellite monitoring, GIS approach, Oil spill distribution

ABSTRACT:

The Persian Gulf (PG) is characterized by a huge number of offshore oil and gas platforms, large oil terminals and busy shipping lines for oil transportation. In this connection, the development of remote sensing methods for assessing the oil pollution of the PG is extremely needed. For the first time, synthetic aperture radar (SAR) images of the European Sentinel-1A and Sentinel-1B satellites were used in 2017-2018 to routinely monitor the entire PG for oil spills. To effectively analyze the SAR images and detected dark patches, a geoinformation approach, specifically, a web-based GeoMixer application is used. This involves the creation of a dedicated geoportal with a large volume of oceanographic, physical-geographical and industrial information about the water basin, including the offshore oil and gas infrastructure. Using this approach, as well as data of ship identification systems (AIS), oil spills were detected and identified. It is shown that the main sources of oil pollution (spills 0.5 to 700 km^2) are oil production and oil transportation.

I. INTRODUCTION

The Persian Gulf (PG), a semi-enclosed basin covering 240,000 km^2 with a maximum depth is about 100 m, is an important water basin (Massuod, 1998). The PG is divided between several oil-rich countries that include Iran, Iraq, Kuwait, Saudi Arabia, Qatar, Bahrain, United Arab Emirates (UAE) and Oman. These countries have active regional economies, sea communications and industry contributing to the pollution of the basin (Patin, 1999). Major ship routes going through the PG waters connect the major economic centers of the PG States with Indian Ocean, and farther with Asia, Europe and America. Among other things, the PG is considered as a marine basin with unique ecosystems and its environment has a tendency to be damaged by the rapid growth of industry, mainly due to oil production and transportation (Pashaei et al., 2015).

This paper presents and analyzes the results of the satellite monitoring of the PG with SAR, undertaken for the detection and identification major oil spills and sources of recent PG's oil pollution.

II. DATA, MATERIALS AND MONITORING METHOD

The ESA SAR image database was used (2017-2018, i.e. during 24 months) in order to find suitable imagery covering the PG. From the analysis of the available Sentinel-1A and Sentinel-1B images acquired in Interferometric Wide mode (IW) mode (with VV polarization, swath width 250 km and pixel spacing 10 x 10 m), about 1700 were selected from the ESA' Copernicus Open Access Hub. Most of them are suitable for the detection of oil slicks and spills. Examples of SAR image sub-scenes with typical and accidental oil spills in the PG are shown in Figures 1, 2.

In order to increase the reliability of the detection and identification of oil slicks and assess the ecological status of the upper layer of the sea, the low and medium resolution optical images from the Terra, Aqua, Suomi NPP, Sentinel-2 and Landsat-8 satellites were also used.

III. SAR MONITORING AND IDENTIFICATION OF OIL SLICKS

Since SAR practically does not measure some of the physical parameters of the oil patches floating on the sea surface, the detection and identification of potential oil slicks in SAR images is a complex process (Brekke and Solberg, 2005; Ivanov, 2011). However, SAR is able to give some information about the oil patches on the sea surface via the form, size, texture and contrast estimated from SAR image. Fully automated analysis of SAR images for the identification and classification of dark patches as oil spills is currently, for a number of objective reasons, poor selling, although interactive ones with the expertise of trained experts can be applied.

Typically, the detection of oil slicks on SAR images consists of several steps: (1) interactive or semiautomatic detection of dark patches or candidates for oil pollution in an image; (2) the extraction of more information about these spots with the help of the computer processing of SAR images and analysis of additional data; (3) the exclusion of look-alikes from consideration, and (4) the subsequent classification of detected oil spills in a number of categories of oil pollution (Brekke and Solberg, 2005).

In order to help the experts analyze the causes and sources of oil pollution, a geoinformation (GIS) approach has been proposed by Ivanov and Zatyagalova (2008). This means assembling all the additional necessary information in a single GIS envelope, mainly focusing on the information about the marine basin and its environment, wind, oil and gas infrastructure, and navigation, to enable the identification of the dark patches on the SAR images with a high probability and create a synergetic analysis of the monitoring results (Ivanov and Zatyagalova, 2008). A GIS approach as web technology and analytical tools have been implemented by the SCANEX Group in the form of internet-based applications, i.e., GeoMixer (http://geomixer.ru).

IV. MAIN RESULTS OF THE MONITORING

The collection and analysis of satellite SAR images covering the PG were conducted in 2017 and 2018. All of the detected and

identified oil slicks were vectorized and placed in the geoportal, where it was possible interactively generating integrated distribution maps and monitoring statistics. The main results for 2018 are summarized in Figure 3 and all results are in Table 1 and are discussed below. In total, more than 1,553 Sentinel-1A SAR images were collected, processed and analyzed. In 2017, on 782 SAR images 4905 oil spills were detected with a total area of 13,835 km^2, whereas in 2018, on 771 SAR images 4812 spills were detected with a total area of 3805 km^2 (Table 1).

Figure 1. Typical oil spills detected on the Sentinel-1A/1B SAR images: a) large spill around the oil production site (Abouzar oilfield, Iranian sector) on 26.03.2017;

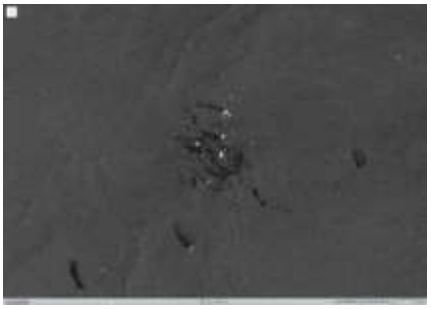

b) numerous oil spills at the oil production site (Salman oilfield, Iranian sector) on 26.03.2017;

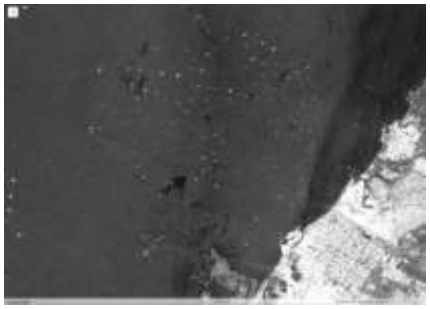

c) numerous ship-made oil spills on the raid of Dubai (UAE) on 10.05.2017;

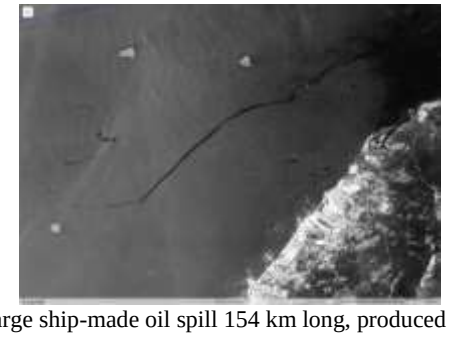

d) large ship-made oil spill 154 km long, produced in the daytime opposite the coast of the UAE, on 10.10.2017.

Figure 3 shows an example of a summary map with firmly identified oil spills detected in the PG on the Sentinel-1A/1B SAR images in 2018. It clearly shows the features and pattern of the one year distribution of oil spills in the gulf. In particular, the analysis of the SAR image collection, this distribution map and annual ship traffic (AIS data is not presented here) revealed the following things:

(1) Oil pollution in the form of oil spills was represented mainly by man-made oil spills, consisting of a variety of oily substances from crude oil and oil products.

(2) The main pollution of the PG occurs at the major oil fields and main shipping routes; from the routine operations such as discharge of dirty ballast waters and tank washing, maybe due to the lack of shore reception facilities.

(3) Most of the large oil slicks were detected on SAR images of the open PG outside of the territorial waters;

(4) The sizes of the detected oil spills varied from 0.1 to 780 km^2; the most frequent patches were from 0.5 to 5 km^2, and they were mostly ship-made spills;

(5) There was a seasonal dynamic for the number of detected slicks: the most frequent oil spills were detected in the summer months, mainly due to lower winds than in other seasons;

(6) The number and total area of the detected slicks depend on the wind conditions, sea state, the intensity of ship traffic, routine oil operations and accidents, as well as a number of other less known factors.

The most polluted marine areas were interactively defined in the geoportal, when all oil spills found on the SAR images were grouped around objects associated with the oil extraction and transportation, such as rigs, terminals, ship lanes, etc. (Figures 1-3). Most interestingly, the risk zones are located outside the territorial waters of the PG, but in their economic zones that possibly removes direct responsibility for oil pollution from a number of PG States. Also, an increased concentration of oil spills is observed in the territorial waters of Iran (well-known Bushehr region), Iraq (on approaches to the oil terminals around Basra), Kuwait and from place to place in the waters of Saudi Arabia. Nevertheless, monitoring also confirmed that the coastal zone (the territorial waters) of the UAE (Dubai, Sharjah and Umm al-Quwain) is prone to severe oil pollution, mainly due to illegal ship discharges.

Among the oilfields around which the oil spills are pronouncedly grouped, there are Iranian Nowrouz, Aboozar, Foroozan, Soroosh Salman and Sirri oilfields; Saudi Arabian Abu Saraf, Foorazan, Zuluf, Manifa, Marjan and Saffaniyah oilfields, Quatari Al Shabee and UAE's Umm Shaif, Zakum, Umm Dalkh and Fatesh, as well as coastal and offshore oil loading terminals (see Table 2).

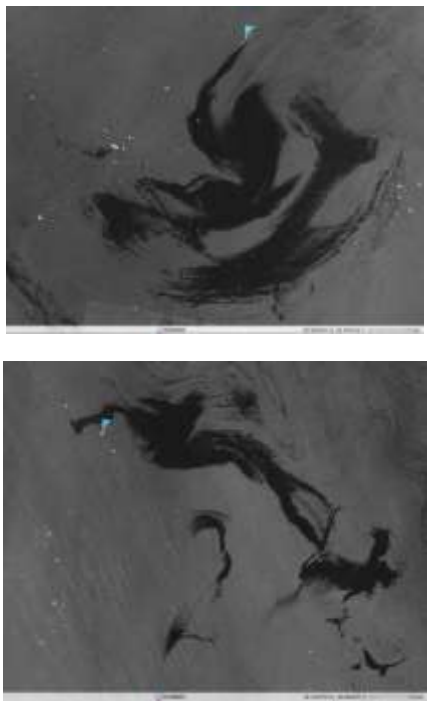

Figure 2. Accidental oil spills in the Persian Gulf on Sentinel-1 SAR images in 2017: up – at the Sirri E oil field (on 11.03.2017 with total area 783 km^2); bottom – at the Aboozar oil field (on 6.06.2017 with total area 259 km^2); flags indicate the sources of the oil spills. © ESA

Table 1. Main monitoring statistics

Year	**2017**	**2018**
Number of acquired and analyzed SAR images	782	771
The total number of detected oil spills	4905	4812
The total area of the detected oil spills (km^2)	13835	3805
The maximal area of an oil spill (km^2)	783	53

The large difference in the total area of pollution in 2017 (13,835 km^2) and 2018 (3805 km^2) can be explained by accidental oil spills that occurred in 2017 (see Figure 2).

V.CONCLUSION

More than 1,550 SAR images from the SAR-equipped Sentinel-1 satellites acquired in 2017-2018 were collected, processed and analyzed, in order to detect the sources of oil pollution and understand the spatial distributions of oil spills in the Persian Gulf. This study included a geospatial aspect, allowing for the identification and exploration of real oil pollution of this marine basin. On the basis of this two-year monitoring, for the first time, maps of the actual distribution of oil spills at sea were created. The processed and analyzed SAR data and summary maps allowed us to conduct spatial-temporal and statistical analysis of the oil spill distribution.

Based on monitoring with SAR, the Persian Gulf, in comparison with other inland basins, maintains a high level of pollution by oil and oil products, i.e., higher than, e.g., in the Baltic Sea and the Black Sea. It is once again confirmed that the main source of oil pollution is oil production. Moreover, due to the current trends in oil and gas development in the Persian Gulf and the traffic intensification via the Hormuz Strait, monitoring of the Persian Gulf with new science satellite-based products, such as oil spill distribution maps, has to become permanent, effective and efficient.

Table 2. Most polluted oil fields, terminals and other offshore places in the Persian Gulf were discovered during SAR monitoring

Source / Country	Oil fields	Oil terminals	Ship lanes	Anchored areas / Other
Iran	Nowruz (?), Aboozar, Sorooch, Foroozan Farzad, South Parz, Salman, Sirri		Main shipping lane running along the long axis of the Gulf; local ship lanes	
Iraq		Al Bakr, Khawr Amaya		
Kuwait	Hout		Local ship lanes	
Saudi Arabia	Sarafaniya, Zulut, Marjan, Berri		Anchored areas	
Bahrain				
Qatar	Al Shabee		Local ship lanes	Anchored area of Abu Dabi
UAE	Umm Shaif, Zakum, Umm Dalkh, Fateh+Pashid, Ummal Qalwan		Local ship lanes	Oil well and seeps off Isl. Sir Abu Nu'ayr
Oman	Bukha West			

ACKNOWLEDGEMENTS

For this study, the Sentinel-1 SAR images from the European Space Agency, which owns their exclusive rights, were provided by SCANEX (www.scanex.ru). This research was carried out in the frameworks of the state assignment of the Russian Federal Agency of Science Organizations (FASO Russia), theme No. 0149-2019-0003, and partially supported by the Russian Foundation for Basic Research (grant #18-55-20010).

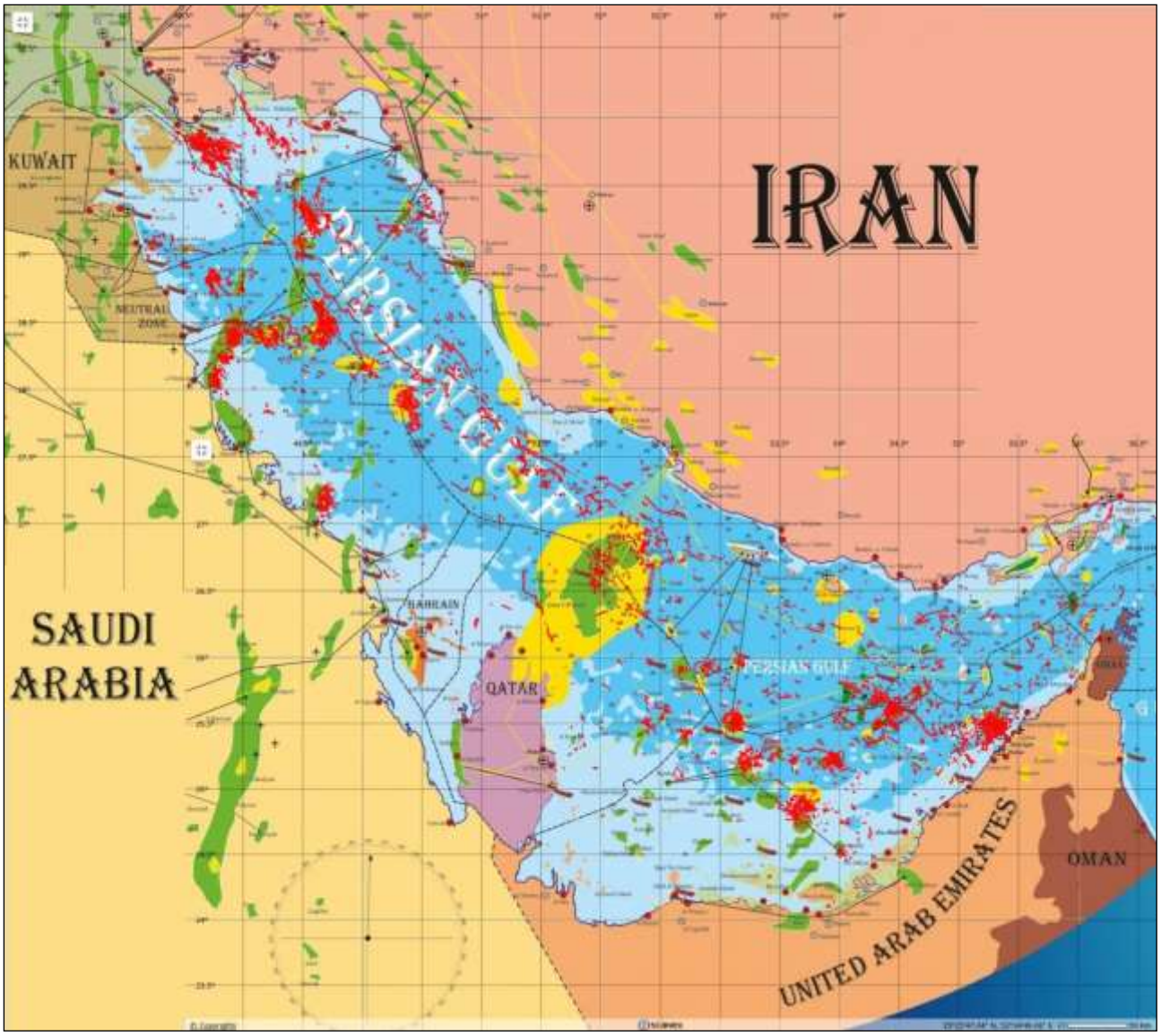

Figure 3. The oil spill distribution map for 2018 (in red) collocated with the Oil & Gas general map (Oil & Gas General Information Map, 2018) clearly shows most polluted oil production sites

REFERENCES

Brekke, C., Solberg, A.H.S., 2005. Oil spill detection by satellite remote sensing in the world oceans. *Remote Sensing of Environment*, 95, pp. 1–13.

Ivanov, A.Yu., 2011. Remote sensing of oil films in the context of global changes. In: *Remote Sensing of the Changing Oceans*, Springer-Verlag, Berlin/Heidelberg, pp. 169–194.

Ivanov, A.Yu., Zatyagalova, V.V., 2008. A GIS approach to mapping of oil spills in a marine environment. *International Journal of Remote Sensing*, 29, pp. 6297–6313.

Massoud, M.S., 1998. The status of oil pollution in the Arabian Gulf by the end of 1993. *Environment International*, 24(1-2), pp. 11-22.

Oil & Gas General Information Map. Scale 1:1050000. Iranian Offshore Oil Company. 2018, http://www.iooc.co.ir/Uploads/image/20181027144726590.jpg.

Patin, S., 1999. *Environmental Impact of the Offshore Oil and Gas Industry*. EcoMonitor Publishing, New York.

Pashaei, R., Gholizadeh, M., Jodeiri Iran, K., Hanifi, A., 2015. The effects of oil spills on ecosystem at the Persian Gulf. *International Journal of Life Sciences*, 5(3), pp. 82-89.

ARTIFICIAL NEURAL NETWORK FOR PRECISE SATELLITE ALTIMETRY SEA LEVEL: TESTING USING SIMULATED DATA

Muhammad Haikal Fayyadh Munadi [1], Nurul Hazrina Idris [1,2]

[1] Tropical Resource Mapping Research Group, Department of Geoinformation, Faculty of Geoinformation and Real Estate, Universiti Teknologi Malaysia81310, Johor Bahru, Malaysia – (mhfayyadh2@graduate.utm.my, nurulhazrina@utm.my)
[2] Geoscience and Digital Earth Centre, Research Institute for Sustainability and Environment, Universiti Teknologi Malaysia, 81310, Johor Bahru, Malaysia

KEYWORDS: Coastal Altimetry, Deep learning, Neural Network, Coastal Sea Level, Waveform Retracking

ABSTRACT:

This paper reports the finding of a deep learning technique based on an artificial neural network to improve the precision of altimetric sea levels over coastal oceans. It is well-known that waveform retracking protocol is necessary to optimise the estimated geo physical parameters. In practice, most of the waveform retracking algorithms are specialised for a particular waveform shape (e.g. multi-peak, ocean-like and quasi-specular). In attempting to generate accurate sea levels from multiple retracking algorithms, one should be concerned about the issue of the existence of relative offset between retrackers that generate 'a leap' in the profiles of the sea level, thus resulting in an inaccurate estimate of the sea level. In this study, the neural network technique is explored to minimise the offset values between retrackers. The performance of neural network technique is accessed based on 10,000 simulated data, which are generated using Monte Carlo simulation. The simulated data are produced by considering different physical characteristics of altimetric waveforms and sea states (e.g., wave height). The multi-layer feed-forward neural network with varying parameters (i.e., number of hidden layers, transfer functions in hidden and output layers, and training algorithm) is explored. There are two sets of the experiment being conducted. Set 1 considers only one input parameter (sea surface height (SSH)) and Set 2 considers two input parameters (SSH and significant wave height (SWH)). The findings indicate that the best parameters for offset reduction are neural network Set 2 with 10 hidden layers, in which the lowest root mean square error (0.7 cm) and standard variance deviation (0.2 cm) are shown.

I.INTRODUCTION

When using satellite altimetry data over coastal ocean, it is a standard practice to implement a data post-processing technique called ‘waveform retracking’. It is a protocol to optimize the estimation of ocean parameters such as sea level, significant wave height and wind speed (Gommenginger et al., 2011).

Over the coastal ocean, altimetric waveforms are highly complicated due to interactions among both lands and oceans. In addition, complicated coastal sea states also contribute to the complexity of waveform shapes. Due to the fact that most retracking algorithms are specialized for a certain shape of waveforms, combining different retracking algorithms (Berry et al., 1998; Idris et al., 2017b; Idris et al., 2017b; Idris and Den g, 2012; Deng and Featherstone, 2006) are crucial when attempting to produce accurate sea levels over coastal oceans. Berry et al., (1998) and Idris et al., (2017b) proposes an expert system to choose the optimal retracker for various waveform shapes, leading to a systematic strategy for decision making. Idris et al. (2017b) combines several retracking algorithms including Ocean Model (Deng and Featherstone, 2006), Modified Threshold (Lee et al., 2010) and Sub-waveform (Idris and Deng, 2012) to retracked altimetric waveforms. The decision to choose the optimal retracker is based on fuzzy inference system (Idris et al., 2017b; Idris and Deng, 2013; Idris, 2014; Idris and Deng, 2012b). Idris et al (2017b), Idris and Deng (2013), and Idris (2014) that also embed the neural network technique to handle the issue of offset when combining different retracking algorithm.

The study by Idris (2014) and Idris and Masrol (2018) reported that the offset among retrackers exists. For instance, offset among the Ocean Model and Modified Threshold retracker is about 2 0 - 30 cm, and 26-36 cm among the Ocean Model and Sub-waveform retracker (Gommenginger et al., 2011). Therefore, when combining the retracked sea levels from various retrackers, one cannot simply switch from one retracker to another. In doing so, the retracked sea level profiles become imprecise because of the ‘jump’ in the sea level profiles. A study by Idris (2014) reported that the value of offset varies due to the variation of significant wave height (SWH).

This paper further investigates the potential of deep learning techniques using neural network approach for reducing the value of offset among various retrackers, aiming at producing accurate sea surface height (SSH) data. Neural network has a great potential for reducing the offset value because of its capability of finding the relationship among retracked sea levels. Multi-Layer Feed-Forward (MLF) neural network is adopted in this study (Demuth and Beale, 2006; Howard et al., 2006). The parameters of sea level and SWH are simulated using the Monte Carlo simulation. Through the neural network, the relationship between the varying sea level and SWH is explored, and a seamless transition of sea levels is produced. Note that a previous study by Idris and Deng (2012a) indicates that there is a linear relationship between SLA and SWH.

II. DATA AND METHODOLOGY

This section describes the data and methodology of the study.

A. Simulated Data

Monte Carlo simulation technique is used to create 10,000 waveform data. The simulated waveforms consider various ocean sea states (Table 1), including varying SWH (0-4 m), and tracking gate (bin 30-31). The value of thermal noise, amplitude and slope of trailing edge are fixed as constant.

Table 1. The parameters for simulating altimetric waveforms

Parameters	Value (unit)
Thermal noise	0.5
Amplitude	100
Epoch	30 - 31 bin
Significant wave height	0 - 4 m
Slope of trailing edge	0.02
Tracker range	40460.5618 m
Orbital height	40533.0266 m
Total atmospheric and geophysical corrections	-1.6403

The simulated waveforms are retracked using two retracking algorithms: 1) Ocean Model (Deng and Featherstone, 2006), and 2) Modified Threshold 30% (Lee et al., 2010). Th e output retracked range from both retrackers are then used to compute retracked SSH, namely 1) SSH Ocean and 2) SSH Threshold 30. When computing the value of SSH, the parameters of orbital height, tracker range and corrections are made constant. The retracked sea levels using Ocean Model is used as a reference when analysing the accuracy assessment.

B. Development of Neural Network

MLF neural network trained by back-propagation learning algorithm and supervised by learning method (Howard et al. 2006) is applied. The neural network consists of the input layer, hidden layer and output layer. Neural network is performed in two modes of operations, which are training and prediction. In the training mode, the network is trained by modifying its weight parameters for the best-desired function approximation. This is done by feeding the network with the input and targeted output. In the prediction mode, the network is fed by the input, and the trained network (during the training mode) is implemented to predict the output.

In this study, the simulated data (10,000) are divided into two: 1) 40% of data are used in training mode; and 2) 60% of data are fed in the prediction model. During the training mode, the input layers are SSH Threshold 30 (and SWH, for Set 2), and the output layer is SSH Ocean. The neural network is trained. During the prediction mode, the input layers are SSH Threshold 30 (and SWH, for Set 2). Using the trained network, the output layer is predicted. The predicted output is the de-offset SSH.

C. Testing with Neural Network

The testing with neural network is conducted by fixing the transfer function in hidden (i.e., Logsig) and output (i.e., Purelin) layers and training algorithm (i.e., Levenberg-Marquardt). The number of hidden layers is varied between 1 to 10, and the number of inputs is varied between 1 (i.e., Set 1) and 2 (i.e., Set 2). Table 2 summarises the various algorithms considered in this study.

The performance of the neural networks is examined by computing the root mean square error (RMSE) and standard deviation of the difference. The SSH Ocean is used as a reference because it is the standard retracker that is widely used over open oceans. For comparison, the analysis of neural network is compared with the Mean Method (MM). This statistical technique is a common method by several researchers (Berry et al., 1998; Idris et al., 2017b; Idris et al., 2017; Idris and Den g, 2012; Deng and Featherstone, 2006). It is conducted by computing the mean of difference among retrackers that are computed based on data over the open ocean. The mean difference is then used to remove the offset value in the retracked SSH over both coastal and open oceans.

Table 2. Two sets of testing with varying number of inputs, transfer function in hidden and output layers, and training algorithm. For each set, the number of hidden layers varied from 1-10

Set	Transfer function in hidden Layer	Transfer function in output Layer	Training algorithm	Input(s)
1	Logsig	Purelin	Levenberg-Marquardt (trainlm)	1 Input (SSH with
2	Logsig	Purelin	Levenberg-Marquardt (trainlm)	2 Input (SSH with

III. RESULTS AND ANALYSIS

Tables 3 and 4 (and Figure 1) show the performance of neural networks. The experiment using one input layer (without SWH, Table 3) indicates that the RMSE and STD of neural network is 10-11 cm and 8-9 cm, respectively. When compared with the MM, the values of RMSE and STD are much higher; 19.96 cm and 17.42, respectively, suggesting that the MM is inaccurate.

However, significant improvements are seen in terms of the RMSE and STD when the SWH parameter is considered in the neural network for offset reduction (Table 4). By maintaining the similar algorithms of neural network (as in Set 1) but adding the extra input parameter of SWH, hereafter called "Set 2", the RMSE and STD are significantly improved to 0.7 cm and 0.2 cm, respectively. Figure 2 illustrates the finding from Set 2.

The relationship between offset and SWH is almost linear (Figure 3). This indicates that the value of offset increases with the increase of SWH value. The finding in Figure 3 proves that the offset value is not a constant and cannot be simply removed using the MM. Therefore, considering SWH when handling the offset among retrackers is crucial.

Table 3. Set number 1 with one input. Comparison with Mean Method is also shown. The best hidden layer is shown in bold, showing the most appropriate neural network algorithm

No of Hidden layer	Set 1 with 1 Input			
	RMSE using NN (cm)	STD using NN (cm)	RMSE using MM (cm)	STD using MM (cm)
1	10.8	9.0	19.96	17.42
2	**10.4**	**8.5**		
3	**10.4**	**8.5**		
4	10.4	8.6		
5	**10.4**	**8.5**		
6	**10.4**	**8.5**		
7	10.5	8.6		
8	10.5	8.6		
9	**10.4**	**8.5**		
10	10.5	8.6		

Table 4. Set number 2 with two inputs. Comparison with Mean Method is also shown. The best hidden layer is shown in bold, showing the most appropriate neural network algorithm

No of Hidden layer	Set 2 with 2 Inputs			
	RMSE using NN (cm)	STD using NN (cm)	RMSE using MM (cm)	STD using MM (cm)
1	2.3	1.6	19.96	17.42
2	1.3	0.9		
3	1.2	0.7		
4	1.3	0.9		
5	0.9	0.5		
6	0.9	0.4		
7	0.8	0.4		
8	0.9	0.5		
9	0.7	0.3		
10	**0.7**	**0.2**		

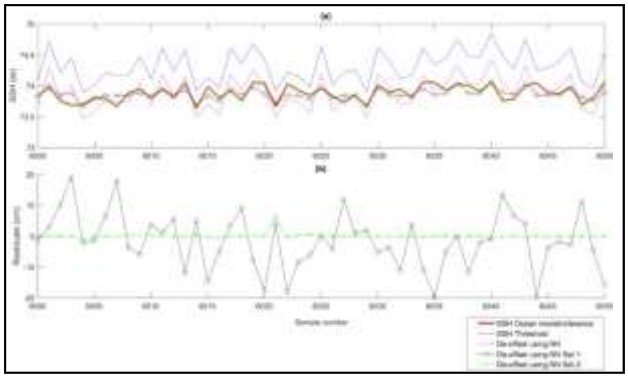

Figure 1. (a) Set 1 (1 input) hidden layer 9 and Set 2 (2 inputs) hidden layer 10 are compared with SSH ocean model to obtain residuals. (b) Residuals value in cm for Set 1 and Set 2

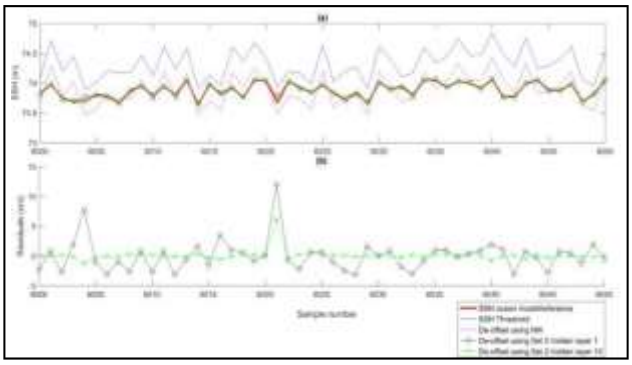

Figure 2. (a) Set 2 hidden layer 1 (worst RMSE) and Set 2 hidden layer 10 (best RMSE) are compared with SSH ocean model to obtain residuals. (b) Residuals value in cm for Set 2 hidden layer 1 and Set 2 hidden layer 10

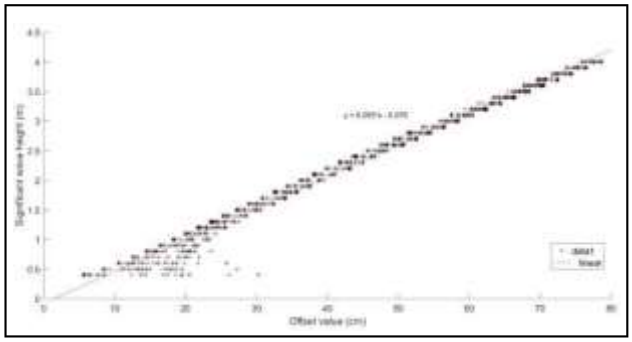

Figure 3. Relationship of offset value (cm) and SWH (m)

IV. DISCUSSION AND CONCLUSION

The finding from this study is similar to those from Id r is et al. (2017b) and Idris and Deng (2012a), where the variation of offset among retrackers is a variable, not a constant. The value of offset varies with varying SWH, suggesting the common MM to minimise the offset is impractical.

This study found that Set 2 (hidden layer 10) is the best algorithms to minimise the offset among the retrackers of Ocean Model and Modified Threshold 30%. This result is nearly similar to that of finding from Idris and Masrol (2018), where they also found the best transfer functions are the Logsig (in hidden layer) and Tansig (output layer). However, the best number of hidden layers is 6, instead of 10 (from this study). Idris and Masrol (2018) reported that the RMSE and STD are 0.7 cm and 4.8 cm, respectively. Meanwhile this study found the RMSE and STD of 0.7 cm and 0.2 cm, respectively. This indicates improvement in terms of STD using the developed technique in this study. Note that the study by (Idris and Masrol, 2018) did not consider any physical variations in the simulated data, and the simulated SSH is not based on any retracking algorithms. They were created arbitrarily, thus less accurate.

Research is currently ongoing to test the neural network algorithms with the real altimetric data and validate the results with independent in-situ data.

ACKNOWLEDGEMENTS

The research is supported by GUP-ICONIC RA Universiti Teknologi Malaysia (Vot 09G73), Ministry of Education Malaysia.

REFERENCES

Berry, P., Sanders, R., Leenmans, C., Bron, E., 1998. Generating orthometric heights from the ERS-1 altimeter geodetic mission dataset: results from an expert systems approach, Geodesy on the Move. Springer, pp. 113-118.

Demuth, H., Beale, M., 2006. Neural Network Toolbox for Us e with MATLAB, Users guide ver. 6.0. 1. The MathWorks, Inc., Natick.

Deng, X., Featherstone, W., 2006. A coastal retracking system for satellite radar altimeter waveforms: Application to ERS-2 around Australia. Journal of Geophysical Research: Oceans 111.

Gommenginger, C., Thibaut, P., Fenoglio-Marc, L., Quartly, G., Deng, X., Gómez-Enri, J., Challenor, P., Gao, Y., 2011. Retracking altimeter waveforms near the coasts, Coastal altimetry. Springer, pp. 61-101.

Howard, D., Mark, B., Martin, H., 2006. Neural network toolbox for use with MATLAB. The Mathowrks User's Gu id e. Version.

Idris, N., Deng, X., 2012a. The retracking technique on multi- peak and quasi-specular waveforms for Jason-1 and Jason-2 missions near the coast. Marine Geodesy 35, 217 -237.

Idris, N.H., 2014. Development of new retracking metho d s fo r mapping sea levels over the shelf

areas from satellite altimetry data. University of Newcastle.

Idris, N.H., Deng, X., 2012b. Coastal waveform retracking for sea surface height estimates: a fuzzy expert system approach. Proc. 20 Years of Progress in Radar Altimetry.

Idris, N.H., Deng, X., 2013. An iterative coastal altimetry retracking strategy based on fuzzy expert system for improv ing sea surface height estimates, 2013 IEEE International Geoscience and Remote Sensing Symposium-IGARSS. IEEE, pp. 2954-2957.

Idris, N.H., Deng, X., Idris, N.H., 2017a. Comparison of retracked coastal altimetry sea levels against high frequency radar on the continental shelf of the Great Barrier Reef, Australia. Journal of Applied Remote Sensing 11, 032403.

Idris, N.H., Deng, X., Md Din, A.H., Idris, N.H., 2017b. CAWRES: A waveform retracking fuzzy expert system for optimizing coastal sea levels from Jason-1 and Jason-2 satellite altimetry data. Remote Sensing 9, 603.

Idris, N.H., Masrol, N.S., 2018. Seamless transition of altimetric retracked sea levels using neural network technique: case stu d y using simulated data, IOP Conference Series: Earth and Environmental Science. IOP Publishing, p. 012097.

Lee, H., Shum, C., Emery, W., Calmant, S., Deng, X., Kuo, C. - Y., Roesler, C., Yi, Y., 2010. Validation of Jason-2 altimeter data by waveform retracking over California coastal ocean. Marine Geodesy 33, 304-316.